A theoretical investigation of oxygen transport and the growth of avascular solid tumor in the micro-environment

趙, 凝

https://doi.org/10.15017/1470522

A theoretical investigation of oxygen transport and the growth of avascular solid tumor in the micro-environment

（微小循環における酸素輸送と無血管期の腫瘍の成長に関する理論研究）

Ning Zhao

2014

DECLARATION

This dissertation was conducted under the supervision of Prof. Iramina Keiji and Prof. Xian Chen. The work submitted in this dissertation is the result of original research carried out by myself, except where acknowledged. It has not been submitted for any other degree or award.

Ning Zhao

July 22, 2014

ABSTRACT

The present dissertation begins with an investigation of a very significant and fundamental topic involved in the microcirculation, namely, the study of the distribution of oxygen concentration at the most detailed level. For this, we numerically calculated the entire process of oxygen transport, by developing a 3D porous media model with coupled solid deformation–fluid seepage–convection and diffusion. The principal novelty of the model is that it takes into account the volumetric deformation of both capillaries and tissue resulting from capillary fluctuation. The model couples the deformations with seepage, and then the coupled deformation and seepage impacts on the convection-diffusion of oxygen. Specifically, we quantitatively examined how solid deformation, fluid seepage, and convection-diffusion combine to affect the transport of oxygen. We obtained the following important findings:

1. Solid deformation is more significant in the middle of a capillary, where the maximum value of volumetric deformation reaches about 0.5%;

2. Though solid deformation has a small impact on seepage, it can exert a positive influence on the tissue fluid so that it flows more uniformly; it can also cause the oxygen to be transported more uniformly, which eventually impacts on the distribution oxygen concentration by 0.1%$\sim$0.5%;

3. The change in pore pressure distribution within the tissue near the arteriole end and near the venule end of a capillary is several times larger than within the tissue surrounding the middle of the capillary;

4. Convection-diffusion given by coupled deformation and seepage has a 16% maximum, and a 3% average, increase in oxygen concentration, compared to pure diffusion. Its more significant role is to allow oxygen to be transported more evenly, especially away from the capillary;

5. Convection-diffusion has a greater effect in the middle of a capillary than near the ends of a capillary. Also, larger values of the permeability coefficient, or smaller values of the diffusion coefficient, produce a more obvious effect on oxygen transport.

Thus, the numerical results from this more comprehensive theoretical model indicate that the convection-diffusion of oxygen transport should be taken into consideration

in relevant studies; the importance of the role lies in the fact that it allows oxygen to be transported more uniformly. This property should be given more attention and studied in more detail. Then, building on this mathematical coupled model for oxygen transport, we developed a coupled mathematical model of avascular tumor growth based on porous media mechanics. This comprises of the migration of tumor cells (TCs), the degradation of extracellular matrix (ECM), the transport of matrix-degrading enzymes (MDEs), the seepage of tissue fluid, and the supplement and consumption of oxygen. The simulation of a solid tumor grows in the micro-environment composed of the pre-existing capillaries and the surrounding tissues. The specific property of changing porosity with the growth of TCs in a tumor micro-environment is taken into account. We proposed functional coefficients for fluid seepage and oxygen diffusion, and incorporated the convection-diffusion of oxygen and the convection of MDEs. From this modified model the main findings included: first, a solid tumor originating in the inlet region undergoes necrosis in the outlet region because of a low supply of oxygen, while a solid tumor originating in the outlet region undergoes necrosis at the primary site because of overconsumption of oxygen; second, tumors further from capillaries grow faster than tumors close to adjacent capillaries; third, the pre-existing capillaries greatly impact on the transport of those chemical factors involved in tumor growth, further impacting on tumor migration and necrosis.

In addition, many previous studies have predicted the importance of MDEs for the diagnosis of certain cancers, for increased MDEs are experimentally examined in early stages of solid tumors, i.e. avascular tumors. However, no quantitative standard exists for MDEs as diagnostic bio-markers. To quantify MDE transport during the avascular stage of solid tumors, a mathematical model based on diffusion-advection models is proposed, coupling MDE convection and diffusion, the amoeboid-like migration of TCs, fluid seepage, ECM degradation, and oxygen convection and diffusion. The data are presented in the fourth chapter. A specific capillary-tissue micro-environment for avascular tumors with changing porosity for the porous medium is incorporated. The numerical results indicated that TCs enter the blood long before cell necrosis; however, MDEs diffuse much further than the TC migration, and enter the blood circulation much earlier than TCs; when a solid tumor originates at the inlet end, MDEs enter the blood 12 cell cycles earlier than TCs; when a tumor originates at the outlet end, MDEs enter the blood 15 cell cycles earlier than TCs. These results theoretically demonstrate the diagnostic significance of MDEs for early cancers, quantitatively provide a basis to determine the tumor stage when MDEs can be detected in blood, and estimate solid

tumor size by measuring MDE concentrations in blood.

Keywords: Porous medium; Microcirculation; Oxygen transport; Convection–diffusion; Solid deformation; Fluid seepage; Tumor micro-environment; Avascular tumor growth; Early cancer detection; Cancer diagnostic bio-markers; Matrix degrading enzymes; Mathematical coupled model

ACKNOWLEDGEMENT

I wish to express sincere appreciation to all the people and associations who contributed to this thesis in one way or another.

First of all, my deepest gratitude goes first and foremost to my supervisor, Prof. Iramina, for his instructive advice and useful suggestions on my dissertation. And high tribute shall be paid to Prof. Chen, who unselfishly provides his two years patience in teaching me how to write a scientific paper better and to make the research more significant. I am also deeply indebted to my father, a profound professor on fluid mechanics in China. He provided many useful and interesting ideas with me not only in the biology field but also in the whole science field, more important is that he likes sharing his experiences in researches as well in life, including how to expand your knowledge of the mind and brain, and how to organize your ideas into a well structural scientific paper. I also want to express my acknowledgement to Prof. Lauwereyns Johan and Prof. Kudo, for their instructive and patient advice to give me many help to improve the quantity and readability of my thesis.

I also would like to express my heartfelt gratitude to the Graduate School of System Life Sciences for their extended long-term supports, and especially to China Scholarship Council which provides plenty of financial support to me during the four years, so that I can pay enough attention to my research and finally receive a doctor degree.

I also owe a special debt of gratitude to Dr. Katayama and all of the colleagues who have left or presently stay in the Iramina'Laboratory of Kyushu University for making the environment rewarding and my research life full of excitement. Special thanks also should go to my families and my friends who have put considerable time and effort into their moments on the draft.

TABLE OF CONTENTS

List of abbreviations

ECM	Extracellular matrix
FEM	Finite Element Method
Hb	Hemoglobin
Mb	Myoglobin
MDEs	Matrix-Degradation Enzymes
MM	Macromolecules
MMPs	Metalloproteinases
RBCs	Red Blood Cells
TCs	Tumor Cells

Chapter 1.

Introduction

1.1 Oxygen transport in microcirculation

1.1.1 Structure of the microcirculation

A primary function of the circulation – to transport nutrients to the tissues and remove the waste products – occurs in the capillaries. The capillaries have only a single layer of highly permeable endothelial cells, permitting rapid interchange of nutrients and cellular waste products between the tissues and circulating blood. About 10 billion capillaries, which have a total surface area of 500 to 700 square meters provide this function for the body.

Blood enters the capillaries through an arteriole and leaves through a venule. Blood from the arterioles passes into a series of met-arterioles, which have structure midway between those of arterioles and capillaries. Arterioles are highly muscular and play a major role in controlling blood flow to the tissues. The met-arterioles do not have a continuous smooth muscle coat, but smooth muscle fibers encircle the vessel at intermittent points called pre-capillary sphincters. Contraction of the muscle in these sphincters can open and close the entrance to the capillary. This arrangement of the microcirculation is not found in all parts of the body, but similar arrangements serve the same purpose. Both the me-arteriole and arterioles are in close contract with the tissues they serve, and local conditions, such as changes in the concentration of nutrients or waste products of metabolism, can have direct effects on these vessels in controlling the local blood flow.

The branching pattern observed in the capillary system varies considerably not only from tissue to tissue, but also within any one bed. In many beds the capillary network is tortuous, with multiple cross-connections, however, in skeletal muscle the arrangement is far more uniform. Fig.1.1 shows the organization of the capillary system in the rat cremaster muscle. The small arteries and veins run parallel to each other, the arterioles branch off at right angles and the capillary networks are arranged so that the capillaries run parallel to the muscle fibres. This figure illustrates two layers of capillaries running parallel to the layers of muscle fibres which lie approximately at right angles to each other. Moreover, the organization of the capillaries in the rat cremaster muscle

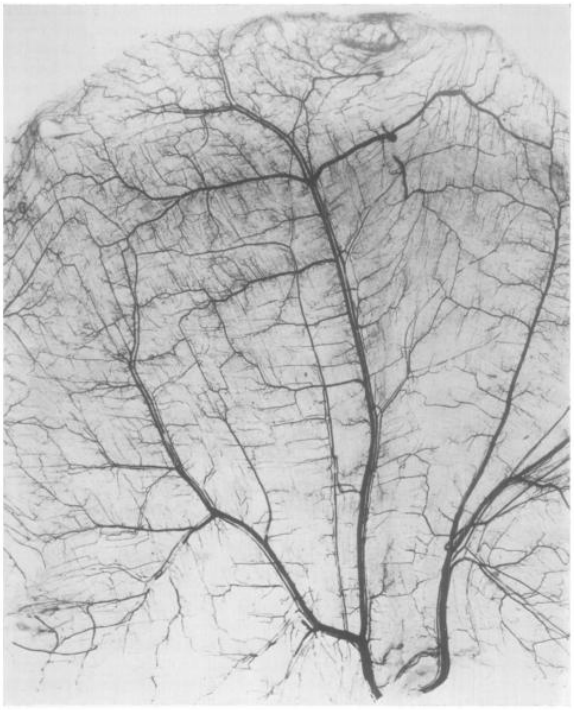

Figure 1.1: Micrography of rat cremaster after intravenous injection of carbon to visualize the vascular pattern. The main arteriole and veins can be seen running parallel to one another. Muscle fibres are arranged in two layers approximately at right angles to one another, with capillaries running parallel to the fibres (Smaje et al 1970).

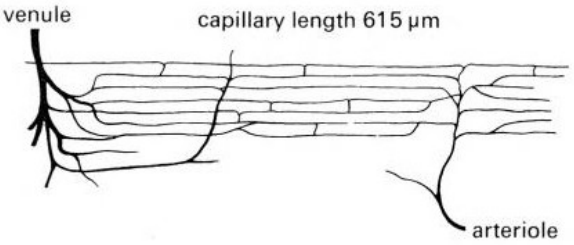

Figure 1.2: Idealized diagram of the capillary network in the rat cremaster muscle. Capillary diameter at arteriole end: 5.5µm; capillary diameter at venular end: 6.1µm; distance between capillaries: 34µm; distance between cross-connections between capillaries: 210µm; capillary density: 1300mm^{-2}; capillary surface area: 244cm^2 per cm^3 muscle; average rat red cell diameter: 7.5µm.(Smaje et al 1970)

is schematically illustrated in Fig.1.2. It will be specially noted that the capillaries are greater in diameter at the venule end than at the arteriole end, but always less that the nominal red cell diameter. It is now widely accepted that capillaries are smaller in diameter than the red cells which have to pass through them and also that the arterial end of the capillary is the narrowest part of circulation, the capillary increasing in diameter along its length. The thin capillary wall consists of a single layer of endothelial cells. Capillaries are also very porous, with several million slits, or pores, between the cells that make up their walls to each square centimeter of capillary surface. Because of the high permeability of the capillaries for most solutes and the high surface area, as blood flows through the capillaries large amounts of dissolved substances diffuse in both directions through these pores. In this way, almost all dissolved substances in the plasma, except the plasma proteins, continually mix with the interstitial fluid.

Blood flows intermittently through capillaries, a phenomenon called "vasomotion". In many tissue, blood flow through capillaries is not continuous, instead, turns on and off every few seconds. The cause of this intermittence is concentration of the metarterioles and pre-capillary sphincters, which are influenced mainly by oxygen and waste products of tissue metabolism. When oxygen concentrations of the tissue are reduced, the periods of blood flow occur more often and last longer, thereby allowing the blood to carry increased quantities of oxygen and other nutrients to the tissues.

1.1.2 Exchange of oxygen between capillary and tissues

In the human circulatory system, arteries and veins are responsible for the transport of blood to and from the heart. An artery carries oxygen-rich blood until it encounters a capillary bed. Oxygen in a capillary is transported into the surrounding tissue where it is absorbed. The deoxygenated blood goes back to the heart through the vein (Middleman 1972). If the supply of oxygen to tissue is insufficient then function will be impaired and damage can appear; for example, brain fainting may occur. Hence, many diseases are believed to be caused by abnormalities in microcirculation (Skalak 1971).

Many pores are distributed in capillary walls. These pores allow fluid to diffuse through them, while selectively impeding the passage of ions and macromolecules, thereby making the capillary walls function as semi-permeable walls. Mass exchange between a capillary and its surrounding tissues varies along the capillary. In the arteriolar end, blood fluid is partly squeezed out of the capillary due to high intravascular blood pressure. In contrast, in the venular end, interstitial fluid in tissue is partly absorbed into the capillary (Michel 1984; Landis and Pappenheimer 1963). Excessive or

very little fluid in the tissue will lead to edema or dehydration, respectively.

Oxygen is transported principally in combination with hemoglobin to the peripheral tissue capillaries, where it is released for use by the cells. About 97% of the oxygen is carried to the tissues in chemical combination with hemoglobin (Hb). The remaining 3% is carried to the tissues in the dissolved state in the water of plasma and cells. Hemoglobin combines with large quantities of oxygen when the oxygen partial pressure, P_{o_2}, is high and then releases the oxygen when the P_{o_2} level is low. When blood passes through the lungs, where the blood P_{o_2} rises to 95 mm Hg, Hb picks up large quantities of oxygen. As it passes through the tissue capillaries, where the P_{o_2} falls to about 40 mm Hg, large quantities of oxygen are released from the Hb. The free oxygen then diffuses to the tissue cells. The oxygen-hemoglobin dissociation curve shows the percent saturation of hemoglobin plotted as a function of P_{o_2}. The oxygen-hemoglobin dissociation curve shown in Fig.1.3 indicates a progressive rise in the percentage of hemoglobin that is bound with oxygen as the blood P_{o_2} increases, which is called percent saturation of the hemoglobin. Note the following features in the curve:

- When the P_{o_2} is 95 mm Hg (arterial blood), the hemoglobin is about 97% saturated with oxygen; an average of nearly four molecules of oxygen are bound to each molecule of Hb.

- When the P_{o_2} is 40 mm Hg (mixed venous blood), the Hb is 75% saturated with oxygen; an average of three molecules of oxygen are bound to each molecule of Hb.

- When the P_{o_2} is 25 mm Hg (mixed venous blood during moderate exercise), the Hb is 50% saturated with oxygen; an average of two molecules of oxygen are bound to each molecule of Hb.

The sigmoid shape of the oxygen-hemoglobin dissociation curve results from stronger binding of oxygen to Hb as more molecules of oxygen become bound. Each molecule of Hb can bind four molecules of oxygen. After one molecule of oxygen has bound, the affinity of Hb for the second molecule is increased, and so forth. Note that the affinity for oxygen is high in the lungs where the P_{o_2} value is about 95 mm Hg and low in the peripheral tissues where the P_{o_2} value is about 40 mm Hg, shown in Fig.1.3.

Hb functions to maintain a constant P_{o_2} in the tissues. Although Hb is necessary for the transport of oxygen to tissues, it performs another major function essential to life as a tissue oxygen buffer system. Under the basal conditions, the tissues requires about

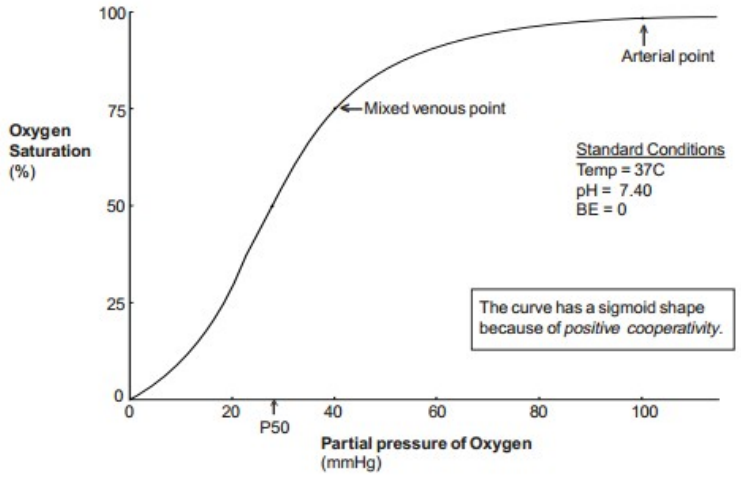

Figure 1.3: Oxygen-hemoglobin dissociation curve

5 mL of oxygen from each 100 mL of blood. For the 5 mL of oxygen to be released, the P_{o_2} must fall to about 40 mm Hg. The tissue P_{o_2} level normally does not rise to 40 mm Hg because the oxygen needed by the tissue at that level is not released from the Hb; therefore, the Hb sets the tissue P_{o_2} level at an upper limit of about 40 mm Hg. The oxygen-hemoglobin dissociation curve is shifted to the right in metabolically active tissues in which temperature and hydrogen ion concentration are increased. The oxygen-hemoglobin dissociation curve shown is for normal, average blood. A shift in the curve to the right occurs when the affinity for oxygen is low, facilitating the unloading of oxygen.

Thus, the exchange of oxygen in microcirculation is an important factor in normal metabolism, and a number of diseases involving the microcirculation, such as the growth of solid tumors, are caused by abnormalities in oxygen transport.(Skalak 1971)

1.1.3 The theoretical studies of oxygen transport in microcirculation

To support the energy requirements of human tissues, oxygen is transported from lungs to the individual cells via the blood circulation. Blood flows away from the heart to arteries, which follow into arterioles, and then narrow further into capillaries. oxygen pass through the capillary wall into the tissue, after the tissue has been perfused, capillaries branch and widen to become venules and the widen more and connect to become veins, which return deoxygenated blood to the heart. Actually, oxygen is primarily carried in the form of oxyhemoglobin, that is, bound to the Hb molecules inside red blood cells (RBCs). The transportation of oxygen from RBCs to plasma, is accomplished in the microcirculation. The microcirculation, which comprises the arterioles, the venules

and the capillaries, its condition are very different from those in large arteries and it is appropriate to consider the flow properties within them separately. Therefore, understanding the properties of oxygen transport at the micro level is a fundamental topic for gaining insight into such diseases. To study the transport of oxygen from capillaries to surrounding tissues requires to be carried on at the level of micron, this is technically challenging for experimental measures, therefore many theoretical model have been developed and applied. But there remain some difficulties for comprehensively modelling oxygen transport at this level: first, though volumetric deformation resulting from capillary fluctuations might significantly affect the transport of oxygen, it would be challenging to model the active capillary fluctuations with different patterns in amplitude, frequency and lasting time. Second, it would be complicated to model the entire process of Hb releasing oxygen to supply the part of oxygen diffused to tissues. Moreover, three different media of capillary lumen, capillary wall and tissues are involved in oxygen transport. These problems imply that understanding the oxygen transport properties at micro level would be a difficult topic.

Various theoretical, experimental, and numerical studies have been performed. The first attempt to describe the phenomenon of oxygen supply to living tissues through microcirculation of blood in mathematical terms is the classical Krogh's model (Krogh 1919a). The model dealts with an idealized geometric arrangement, consisting of one capillary of a circular cross section concentric with a circular cross section of muscle tissue. This pioneering theoretical model is built on a number of idealized assumption, including: constant oxygen consumption rate, uniform oxygen diffusivity, and homogeneous capillary distribution (Krogh 1919b). The derivation of the model in tissue sub-domain can also be found,(Middleman 1972) in terms of the diffusion equation. Since then, some investigators have paid much attention to the role of oxygen transport to tissue and many alternative oxygen transport models have been developed (Goldman 2008; Popel 1989; Pittman 2011c) with a lot of additional physiological features. These are neglected in the Krogh-Erlang model, including variable oxygen consumption rate, intravascular oxygen transport resistance, myoglobin (Mb) facilitated diffusion, axial oxygen diffusion in the tissue, time dependent oxygen transport, pre- and post-capillary transport and flow redistribution. These important modifications were made while maintaining the Krogh geometry as discussed below.

Tissue oxygen consumption is often assumed to be uniform, but oxygen dependent consumption in mathematical models is proposed to simulate the oxygen delivery under hypertension (Greene et al 1992) and under the condition of high oxygen demand

(McGuire and Secomb 2001). A global existence of a unique smooth solution of the nonlinear diffusion of oxygen in a living tissue, in presence of consumption due to metabolism, was discussed.(Mikelic and Primicerio 2006) The existence of intravascular pressure gradients implies a finite intravascular resistance to blood-tissue oxygen transport (Federspiel and Popel 1986). The Mb molecule found in heart and striated muscle could bind and release oxygen in the same way as Hb, and its movement could enhance oxygen diffusion. Mb diffusion appears to be isotropic in heart and skeletal muscle cells (Papadopoulos et al 2001) with $D_{MB} \approx 8 \times 10^{-7} \mathrm{cm}^2/\mathrm{s}$ in heart at $40\,^{\circ}\mathrm{C}$ (Lin et al 2007). Axial oxygen diffusion in the tissue has also been found to be important for modeling microcirculation transport, because each slice of the tissue cylinder is not independent but can exchange oxygen with neighbors. Axial diffusion inside following capillaries is less important due to the relatively greater effect of axial convection (Grinberg et al 2005). Titcombe et al investigated an asymptotic solution for a diffusion problem in 2D which describes oxygen transport from multi-capillaries to skeletal muscle tissue.(Titcombe and Ward 2000) Analysis of oxygen concentration in 2D array of capillaries, in terms of a system of ordinary differential equations for the oxygen concentration coupled with a system of algebraic equations for the fluxes, was investigated.(Salathe 2003) Several studies use time-dependent Krogh-type models since the convective oxygen supply to individual capillaries can vary considerably over time and there are many problems of interest in which time dependent oxygen transport is relevant (Schumacker and Samsel 1989; Piiper and Scheid 1991; Lagerlund and Low 1991;Lagerlund and Low 1993; Sharma and Jain 2004). Since arterioles and venules are also involved in blood-tissue diffusive oxygen transport, it is important to understand how they carry oxygen and release oxygen to the surrounding tissue before including them in models of tissue oxygen delivery (Hellums et al 1996; Popel and Gross 1979; Moschandreou et al 2011). Hoofd investigated the effects of flow redistribution on muscle oxygenation(Hoofd and Degens 2009). Based on Krogh model, a critical ratio between supply and consumption of oxygen in tissue region in order to fulfill cells oxygen requirements was obtained.(Yulianti and Gunawan 2012)

In the above modifications to the standard Krogh model, investigators did not take account of oxygen diffusion between capillaries, which is believed to be important in many physiological situations. As a first step towards studying oxygen transport by realistic capillaries network, parallel arrays of capillaries have been considered (Klitzman et al 1983). A steady-state model of oxygen transport was presented (Hsu and Secomb 1989) and was extended a previous parallel capillary model to the case of 3D oxygen

transport from capillary network.(Groebe 1990) In addition, oxygen transport models have been extended to include complex capillaries network geometry with capillary tortuosity and anastomoses (Goldman et al 2004; Goldman and Popel 2000; Secomb et al 2004). As for oxygen transport, another essential study on oxygen storage in the form of oxyhemoglobin was investigated by many experiments (Sehgal et al 1984; Rosen et al 1990; Biro et al 1991; Palaparthy et al 2001) and simulated by numerical models. The majority of blood substitute products are being developed based on Hb which is a natural oxygen carrier of RBCs. Page has described a mathematical model for oxygen transport by RBC/extracellular Hb solution mixtures, flowing in arteriolar-size tubes with diameters in the range of 20-100μm (Page et al 1998). Their model predicts that RBC/Hb solution mixtures transport oxygen more efficiently than RBC suspensions in plasma. A model was developed for oxygen transport by RBCs and hemoglobin solution in the capillary-size vessels to investigate the influence of Hb-based oxygen carriers on the delivery of oxygen to tissue (Vadapalli et al 2002). Theoretical studies suggest that significant longitudinal gradients in blood oxygen tension and Hb saturation exist in pre-capillary vessels (Sharan et al 1998).

In spite of the fact that numerous studies have been conducted on the solute transport in a porous medium and the theoretical framework for solute transport in porous materials is established (Bird et al 2002; Edwards and Brenner 1993), many fundamental questions related to solute transport in a porous medium have not been answered satisfactorily. Lei et al (1998) proposed a three-porous-media model to describe extravascular mass transport and trans-vascular mass exchange. Two model-based studies to investigate the blood and interstitial flows through a solid tumor with a single tube or an interior vascular network were carried out. The work presented a framework to describe the blood and fluid flow through the interstitium, and it was subsequently developed for various applications (Pozrikidis 2010; Pozrikidis and Farrow 2003; Pozrikidis 2010). A multi-scale model was presented to describe fluid flow through blood vessels and interstitium in solid tumors (Chapman et al 2008). The resulting equations derived by systematic asymptotic analysis show that both the vascular network and the tumor interstitium behave as a porous medium with fluid transport between them. The porous medium modelling generally applies in the study of drug delivery. In Wang's work (Wang and Olbricht 2010), brain tissues are assumed to be a homogeneous porous medium and the interstitial transports of macro-molecules are governed by the mass conservation equation for computational study on retro-convection enhanced drug delivery. Mixture theory model of fluid and solute transport has commonly been utilized

to describe transport in a porous medium for non-biological material (Hartridge and Roughton 1923). Schuff et al (2013a) presented a comprehensive model that includes transport in the vessel lumen, the vessel wall, and the interstitial space and considers the effect of the solute concentration on fluid flow. This model was used in a companion paper to examine fluid and solute transport for simplified case of an axisymmetric geometry with no solid deformation. In addition to understanding how the differences in the vasculature of normal and malignant tissues affect transport and applicability of existing mathematical models, they further determined an appropriate set of governing equations as it is necessary to specify appropriate model parameters based on physiological data (2013b). In order to understand the effect of fiber type and size on the heterogeneity of oxygen distribution, Liu et al (2012) used models coupled by convective oxygen transport in the blood vessels and oxygen diffusion and consumption in tissue. Convection-diffusion was only considered in the region of intravascular space in the models. A theory for solute transport in a porous medium was developed by using the mechano-electrochemical mixture theory. The convective and diffusive fluxes of solute in such a material also had been clearly defined (Yao and Gu 2007).

Finite element method (FEM) is especially powerful for analysis flows in complex geometries and is hence particularly suitable for handling problems with realistic geometries. Nassehi et al (2005) performed finite element modeling of flow through pleated cartridge filters, which can be simulated as combined Stokes/Darcy flow. He's study (2012) employs the FEM to simultaneously investigate the blood and fluid flow in a permeable curved capillary and the surrounding tissue. The computational domain is composed of a fluid capillary sub-domain coupled with a porous tissue sub-domain. The flows in the sub-domains are described by the Stokes and Darcy equations, which are solved in a coupled manner by applying a nodal replacement scheme at the capillary wall. However, few papers have reported the application of FEM in such studies because of the difficulties of this method.

Developments during the last 40 years, including studies of oxygen gradients in arterioles, capillaries, venules, capillary wall and surrounding tissues are reviewed (Pittman 2011a). The understanding of oxygen transport from the perspective of the microcirculation has progressed from a consideration of oxygen gradients in capillaries and tissue to the realization that oxygen has the ability to transport from any capillary to another location under the conditions in which there exists a large enough oxygen tension gradient and that the seepage for oxygen along the intervening pathway is sufficient (Pittman 2013; Popel et al 2003). The effect of convection-diffusion and deformation of tissue

have not been paid enough attention. It was generally viewed that convection of oxygen within tissue could be neglected because many studies considered that tissue fluid flows very slowly within tissues. However, the deficiency remains exist in studying for seepage of tissue fluid: seepage might be significantly affected by the deformation of microcirculatory structure which could be caused by capillary fluctuation. The deformations at micro level are very difficult to be measured by the experiments biologically, thus, the deformation was considered and studied in some relevant mathematical models(Yao and Gu 2007;Byrne and Preziosi 2003). Therefore we take account of oxygen transport in deformable porous media, where the volumetric deformation is modelled basing on the pressure variations of capillary fluctuation from experiments.(Zweifach 1974) It is therefore necessary to establish a comprehensive mathematical model of oxygen transport in the microcirculation.

1.2 Growth of avascular solid tumor

Understanding oxygen transport in microcirculation is also an essential topic for studying the progress of a solid tumor.

1.2.1 Oncogene

All cancers begins with a single cell becoming transformed, owing to the genetic material (DNA) of a cell start producing mutation that affect normal cell growth and division by being damaged. This transformed cell differs from a normal one in several ways, one of the most notable being its escape from the bodys homeostatic mechanisms, leading to unregulated, quickened proliferation. An individual tumor cell has the potential, over successive divisions, to develop into a cluster (or nodule) of tumor cells (TCs).

There are several stages in the growth of a tumor before it becomes so large that it causes the patient to die or reduces permanently their quality of life. There is a lot of controversy over how exactly cancer is initiated, but it is a generally accepted view that it required several gene mutations to turn a normal cell into a cancer cell (Lengauer et al 1998;Charles and Rubin 1998). These genes belong to one of three classes: gatekeepers, caretakers and landscapers. Gatekeepers directly regulate growth and differentiation pathways of the cell and comprise oncogene and tumor-suppressor genes. Caretakers, by contrast, promote tumorigenesis indirectly (Rajagopalan et al 2003;Sieber et al 2003). Landscaper defects do not directly affect cellular growth, but generate an abnormal stromal environment that contributes to the neoplastic transformation of cells (Bissell and Radisky 2001).

Oncogene can contribute to tumorigenesis if one allele is mutated or inappropriately expressed (Charles and Rubin 1998). Over the past decades, many oncogenes have been discovered that are involved in various stage of human cancers – tumor initiation, progression, angiogenesis and metastasis. Tissues of multicellular organisms are subdivided into compartments, which contain populations of cells that proliferate to fulfill organ-specific tasks. Compartments are subject to homeostatic mechanisms that ensure that the cell number remains approximately constant over time. Whenever a cell divides, another cell has to die to keep the total population size the same. Cancer results if the equilibrium between cell birth and cell death is shifted towards uncontrolled proliferation. Not all cells of a compartment, however, might be at risk of becoming neoplastic. Differentiated cells, for example,might not have the capacity to divide of-

ten enough to accumulate the necessary number of mutations in cancer-susceptibility genes.(Michor et al 2003) The effective population size of a compartment describes those cells that are at risk of becoming cancer cells.

Considering a compartment of replicating cells. During each cell division, there is a small probability that a mistake will be made during DNA replication; in that case, a mutated daughter cell is produced. The mutation might confer a fitness advantage to the cell by ameliorating an existing function or inducing a new function. Then the cell proliferates more quickly or dies more slowly than its neighbors, and the mutation is advantageous in terms of somatic selection. Alternatively, the mutation might impair an important cellular function and confer a fitness disadvantage to the cell. Then the cell proliferates more slowly or dies more quickly than its neighbours. The net reproductive rate is decrease, and the mutation might not change the reproductive rate of the cell. Then the cell proliferates at the same rate as its neighbours and the mutation is neutral in terms of somatic selection. Large compartment accelerate the accumulation of advantageous mutations, but slow down the accumulation of deleterious mutations. Conversely, small compartments slow down the accumulation of advantageous mutations. Therefore, the compartment size is important in determining the types of mutations that are likely to occur.(Michor et al 2004)

1.2.2 Avascular phase for a solid tumor

At the very early stages, the vasculature is generally absent, and the TCs take all their nutrients from the surrounding tissue. This process is defined as the avascular stage for a solid tumor, where the TCs, healthy cells (HCs), variable molecules in the surrounding tissues, together with tissue fluid compose the particular micro-environment for early solid tumor growth and invasion. The interactions between cells and between cells and the molecules play a key role in this process.

As described in Sect.1.2.1, the factors that trigger these mutations are largely unknown, but are thought to include both environmental and hereditary effects. One of the outcomes of this series of mutations is an increase in the proliferation rate and a decrease in the death rate of the cells, giving rise to a clump of tumor cells growing faster than the host cells. However, even a fast growing clump of tumor cells cannot grow beyond a certain size, since there is a balance between cells inside the clump consuming nutrients and nutrient diffusion into the clump.(Michor et al 2004) Therefore, the general view is that one of the most important steps in malignant tumor growth is angiogenesis, which is the process by which tumors develop their own blood supply.

For this reason novel drugs are being developed specifically to target tumor blood vessels. Once the tumors have acquired their own blood supply, the tumor cells can escape the primary tumor via the circulatory system (metastasis) and set up secondary tumors elsewhere in the body. After angiogenesis and metastasis, the patient is left with multiple tumors in different parts of the body that are very difficult to detect and even more difficult to treat. Nevertheless, as of now, around 100 types of cancer are known to exist and about one-third of these can be cured for detected in an early stage. It implies the need to understand the vital mechanism that are always at play during the early stage of tumor growth.

Because there are three distinct stages (avascular, vascular, and metastatic) to cancer development, researchers often concentrate their efforts on answering specific questions on each of these stages. This present study aims to describe the current state of mathematical modeling of avascular tumor growth, i.e., tumors without blood vessels. There are some questions concerning avascular tumors which may be interesting in their own right, including the recent controversial hypodissertation that all humans have small dormant avascular tumors in their bodies.(Udagawa et al 2002) There are also parallels between avascular tumor growth and the growth of a tumor tissue in the micro-region supported by a single blood vessel inside a vascular tumor, as illustrated in Fig.1.4, where the different regions of both avascular and vascular tumors (to be explained shortly) are shown. Thus, avascular tumor modeling can be of use when making predictions and designing experiments on vascular and metastatic tumors, which are much more time consuming and difficult as they have to be performed in vivo.(Roose et al 2007)

1.2.3 Micro-environment for avascular tumor growth

As described in Sect.1.1.1, normal micro-environment comprises three essential sub-regions: capillary, capillary wall and surrounding tissues. For the growth of a solid tumor at the avascular phase, four important factors including TCs, ECM, MDEs and oxygen which are involved in avascular tumor growth are also significantly taken account into the specific micro-environment of avascular tumor growth, together with capillary, capillary wall and tissues. The physiological function of the four key factors are detailed shown in this section.

The interactions between cancer cells and their micro-environment create a context that promotes tumor growth and protects it from immune attack. The functional association of cancer cells with their surrounding tissues forms a new “organ” that changes

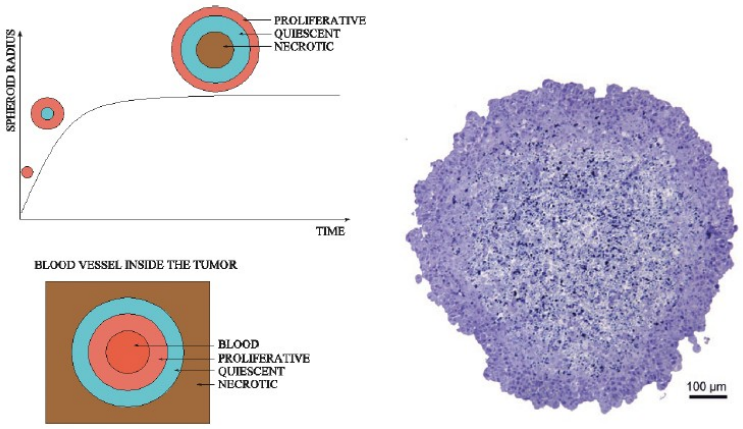

Figure 1.4: Left: Schematic illustration showing tumor spheroid growth. Right: 1 micron of spheroid section showing the proliferative rim and the necrotic core. (Roose et al 2007;Yu et al 2004)

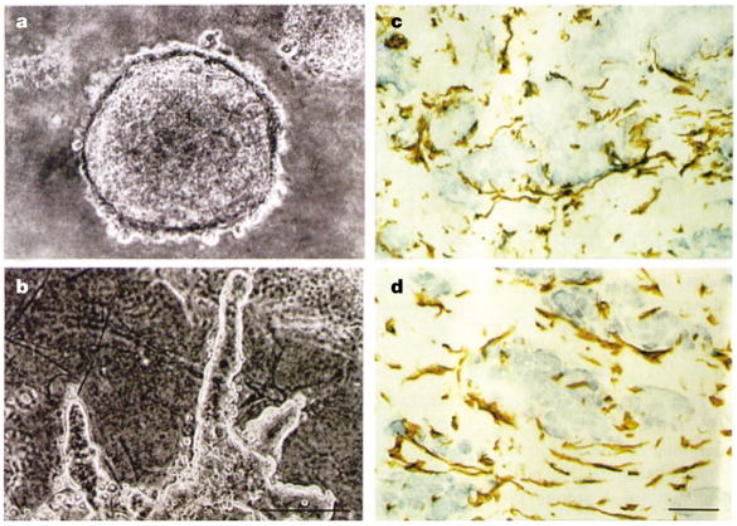

Figure 1.5: The tumour micro-environment assay. a. Primary breast carcinoma cells form spherical colonies when cultured in three-dimensional collagen type I. b. Co-cultivation with stromal cells, however, causes the tumour cells to spread and become invasive. The degree of tumour growth increases with the density of the stromal cells. Staining of the co-culture assay c. and of tumour d. with anti-vimentin antibody reveals the structural similarities of stromal cells in the presence or absence of cancer cells.(Jessen et al 1995)

as malignancy progresses. Investigation of this process might provide new insights into the mechanisms of tumor growth and could also lead to new therapeutic targets. An example of a diagram of tumor micro-environment is illustrated in Fig.1.5.

Degradation of ECM

As a major component of the cellular micro-environment, the extracellular matrix (ECM) takes part in most basic cell behaviors, from cell proliferation, adhesion and migration, to cell differentiation and cell necrotise (Hynes 2009). As the mass of TCs increases, the ECM undergoes extensive rearrangements with increased deposition of collagen fibers, making the resulting tissue thicker and more difficult to trespass(Jain and Stylianopoulos 2010). Also, since the TCs divide much faster than normal cells, the growing tumor mass exerts mechanical stresses on the surrounding healthy tissue, leading to the localized constriction and, at times, collapse of blood and lymphatic vessels. At this point, the TCs are already numbering millions and the malignant tissue has reached a characteristic size of hundreds of microns.

The ECM is a complex mixture of macromolecules (MM) in the tissues, some of which, like the collagen, play a structure role and others, such as laminin, fibronectin and vitronectin, are important for cell adhesion, spreading and motility. We note that all of these MM are bound within tissue and are non-diffusible. For the tumor cells, their ability as a molecular bridge between an external ligand and the cytoskeleton within the cell affects the tumor cells migration.(Burridge and Chrzanowska-Wodnicka 1996) Thus, the TCs differ from HCs in other properties such as cell-surface proteins(Nicolson 1984). Before a tumor becomes invasive, the roughness of its surface is caused by variation in how groupsof peripheral cells degrade the ECM they are in contact with. In fact, the degradation of the surrounding tissue or ECM achieved by TCs is that the most crucial part of avascular tumor invasion process, owing to ECM may have to be reduced in order to allow the TCs to spread, its degradation may, in addition, have vital biological effects on TCs (Liotta et al 1983;Stevenson et al 1993;Lawrence and Steeg 1996). To degrade basement membranes enzymatically may augment the aggressive behavior of some TCs , while the ECM can also sequester growth factors and itself be degraded to release fragments which can have growth-promoting activity (Anderson 2005).

Under normal conditions, ORGANS are made up of TISSUES that exchange information with other cell types via cellcell contact, cytokines and the ECM. The ECM, which is produced by collaboration between STROMAL fibroblasts and EPITHELIAL

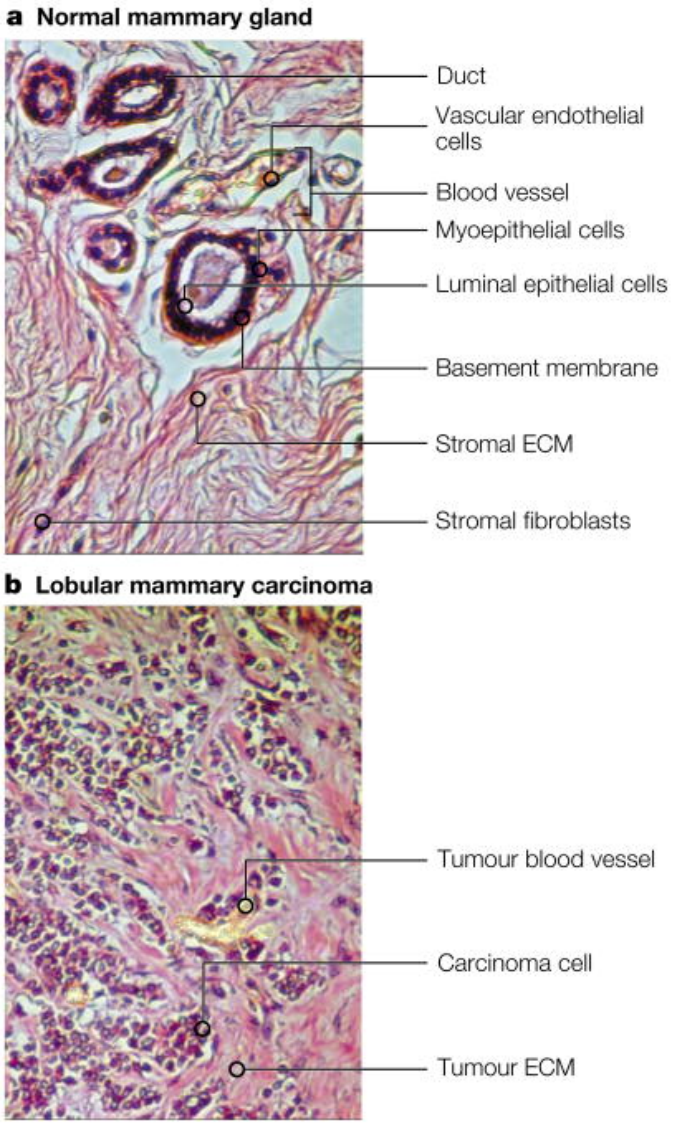

Figure 1.6: Normal versus malignant breast tumors. The normal mammary gland shows a highly structured and segregated architecture. Ducts are formed by a double layer of cells: luminal epithelial cells surrounded by a layer of myoepithelial cells, enclosed by the basement membrane. Stromal fibroblasts secrete a collagenous ECM, and blood vessels are centrally located and well defined. b. Lobular breast carcinoma is less organized. Tumour angiogenesis produces poorly defined blood vessels, and carcinoma cells intermingle with all the stromal elements.(Bissell and Radisky 2001)

cells, provides structural scaffolding for cells, as well as contextual information. The endothelial vasculature provides nutrients and oxygen, and cells of the immune system combat pathogens and remove apoptotic cells. Epithelial cells associate into intact, polarized sheets. These tissues communicate through a complex network of interactions: physically, through direct contact or through the intervening ECM, and biochemically, through both soluble and insoluble signalling molecules. In combination, these interactions provide the information that is necessary to maintain cellular differentiation and to create complex tissue structures.(Bissell and Radisky 2001)

Occasionally, the intercellular signals that define the normal context become disrupted. Alterations in epithelial tissues can lead to movement of epithelial sheets and proliferation for example, after activation of mesenchymal fibroblasts due to wounding. Normally, these conditions are temporary and reversible, but when inflammation is sustained, an escalating feedback loop ensues. Under persistent inflammatory conditions, continual up-regulation of enzymes such as matrix metalloproteinases (MMPs) by stromal fibroblasts can disrupt the ECM, and invading immune cells can overproduce factors that promote abnormal proliferation.

As this process progresses, the normal organization of the organ is replaced by a functional disorder (Fig.1.6). If there are pre-existing epithelial cells within this changing context that possess tumorigenic potential, they can start to proliferate. Alternatively, the abnormal interactions might lead to genomic instability within the epithelial cells and the acquisition of tumorigenic potential. The proliferating cancer cells can then interact with their micro-environment and enhance the abnormal interactions. At this point, the tumour has become its own organ, with a distinct context that now defines all its cellular responses. Here, we will examine how the mechanisms that contribute to the normal context also act to suppress developing tumours, how disruption of this context initiates and supports the process of tumorigenicity, and how some cells with a tumorigenic genotype can become phenotypically normal if the context is appropriately manipulated.

MDEs degrade ECM

Liotta et al found a characterised neutral protease purified from metastatic TCs has the ability to degrade the Type IV collagen (a normal constituent of ECM), but not to degrade other collagen or fibronectin (Liotta et al 1980). Type IV collagen known to be a major structural protein of basement membranes, along with laminin, plays an important role in cell adhesion, migration, differentiation, and growth (Aumailley and

Timpl 1986). It has been proposed that proteases secreted by TCs facilitate metastasis by degrading ECM in many studies. These proteases are known as matrix degrading enzyme (MDEs), mainly composed of the type MMPs and Urokinase Plasminogen Actovators (uPAs). In 1990s, a number of MDEs such as plasminogen activator system and the large family of MMPs have been described (Briozzo et al 1988;Matrisian 1992;Mignatti and Rifkin 1993;Thorgeirsson et al 1994;Gohji et al 2001), and both of these have been repeatedly implicated in tumor invasion. In addition to opening the migratory pathway, Cancer-induced degradation leads to the reorganization of the protein network that forms the ECM. In detail, MDEs can alter cell adhesion properties regulated through several classes of cell-surface receptors. These receptors, including cadherins, CD-44, integrins and receptors for fibronectin, laminin and vitronectin, negatively regulate cell motility and growth through cell-cell and cell-matrix interactions (Stevenson et al 1993). Therefore, degradation of receptors and ECM components could lead to the TCs detached from the primary tumor. Also, in many cases, its degradation products promote cell migration and proliferation. For instance, certain ECM protein-complexes like vitronectin, fibronectin, laminin, type-I collagen, type-IV collagen,and thrombospondin stimulate tumour cells into migration(Bogenrieder and Herlyn 2003). Both haptotaxis and chemotaxis are induced by different types of degradation of these proteins (Perumpanani et al 1998).

MMPs are the major components of MDEs, they can degrade ECM and are involved in promoting the inflammatory response, normal tissue remodelling, wound healing and angiogenesis46. These enzymes, however, also have an important function in malignancy (Vu and Werb 2002). The sustained presence of these proteinases in the tumour environment, produced both by the activated cells and by the cancer cells, leads to destruction of normal ECM. Degradation of ECM stimulates both proliferative and apoptotic mechanisms, which can lead to the selection of apoptosis-resistant carcinoma cells and enhanced invasive potential (Mitsiades et al 2001). In the tumour context, direct association of MMPs with specific ECM receptors provides spatial control of MMP activity and directional signals to the invading tumour cells (Yu and Stamenkovic 2000).

Migration of tumor cells

But how do migrating cancer cells move through tissues and become organized into invasive tumours, as determined by histopathology? In vitro and in vivo observations have shown that tumour cells infiltrate neighbouring tissue matrices in diverse patterns.

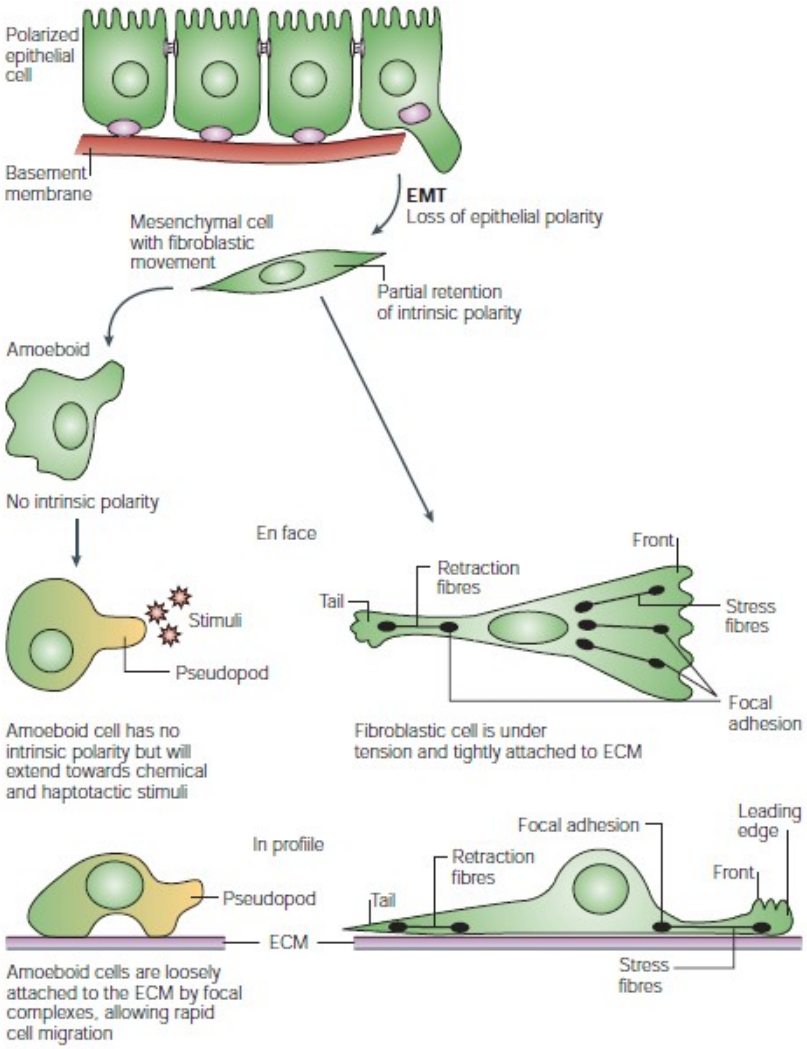

Figure 1.7: Definitions of types of cell movement. During the epithelialmesenchymal transition (EMT), tumour cells undergo a loss of intrinsic polarity and lose cellcell junctions that are required for the integrity of the epithelium. These events require extensive reorganization of the cytoskeleton and initiation of actin-based cell motility. Cells that partially retain their polarity still have a tail that contains retraction fibres and a front that contains stress fibres and can form focal adhesions. They can still attach to the ECM. Conversely, cells that lose all polarity are characterized as “amoeboid”.(detailed in Condeelis and Segall 2003)

They can disseminate as individual cells, referred to as "individual cell migration", or expand in solid cell strands, sheets, files or clusters, called "collective migration". In many tumours, both single cells and collectives are simultaneously present. Whereas leukaemias, lymphomas and most solid stromal tumours, such as sarcomas, disseminate via single cells, epithelial tumours commonly use collective migration mechanisms. In principle, the lower the differentiation stage, the more likely the tumour is to disperse via individual cells(Friedl and Wolf 2003). Such differences in cellular patterning putatively reflect variations in the molecular repertoire used by a cancer cell to migrate. In mammary tumours, invasion and intravasation occur primarily during the carcinoma stage (Lina et al 2001). During this stage, extensive loss of ECM networks has already occurred and cell shape and movement are not constrained by dense networks of ECM (Fig.1.7). ECM fibres that are composed of collagen and possibly other ECM proteins are identifiable and migration of cancer cells is most evident on these long ECM fibres (Zipfel et al 2003), shown in Fig.1.8. Cell migration of this type is characterized as "amoeboid", meaning that the cells undergo marked shape changes while crawling and are not fibroblastic during migration (Allen and Allen 1978;Condeelis et al 1992). Fibroblastic migration is characterized by cells that are elongated and under tension, causing them to be rigid in shape except near their leading edges, where lamellipods are observed to extend (Fig.1.7). In vitro, dense networks of ECM can induce amoeboid motility (Friedl and Wolf 2003). However, our in vivo imaging raises the possibility that such severe ECM constraints are not always necessary. If carcinoma cells are able to undergo amoeboid movement in vivo in the absence of constraints of an ECM network that is postulated to cause the transition from fibroblastic to amoeboid motility other factors must be at work in the tumour to induce this transition (Fig.1.7).

In vitro and in vivo studies in cell lines led to the original observations that individual tumour cells are motile. Individual motile tumour cells usually originate from the interstitial stroma or bone marrow. Alternatively, cells that originated from a multicellular compartment, such as epithelium, lose their cell contacts, detach and migrate as individual cells through the adjacent connective tissue. Based on cell type, integrin engagement, cytoskeletal structure and protease production, single-cell migration can occur in different morphological variants. These variants include mesenchymal and amoeboid types, as well as cell chains (Fig.1.9).

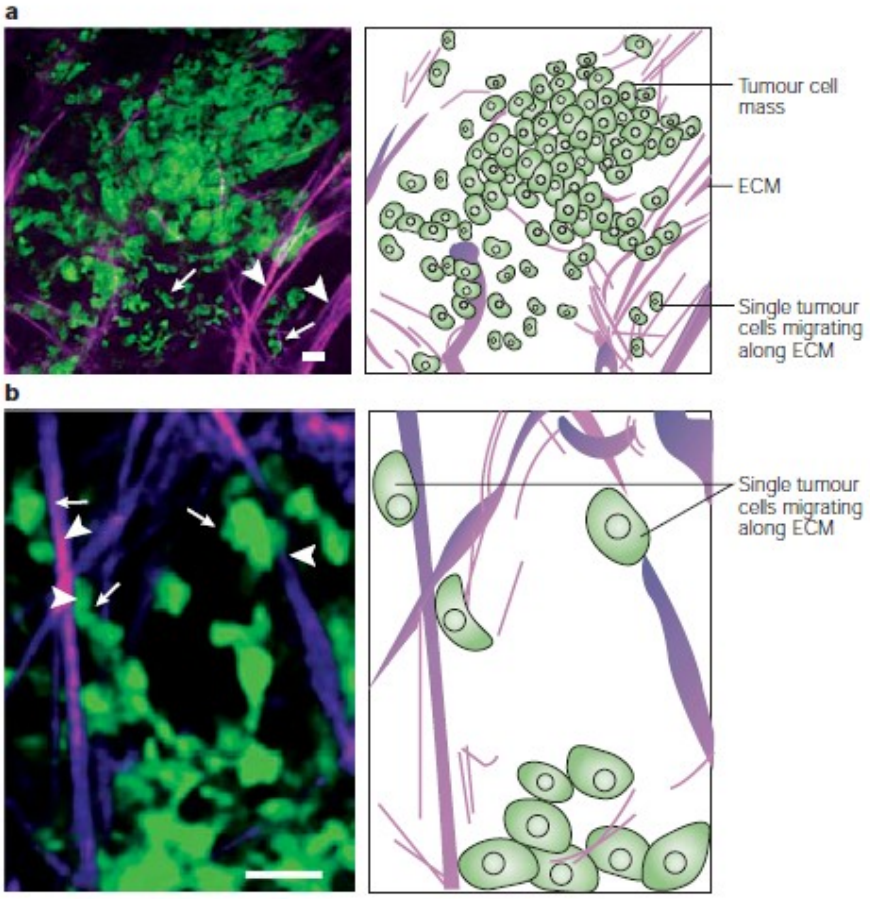

Figure 1.8: Carcinoma cells in primary mammary tumours move along ECM fibres. Multi-photon microscopy shows that carcinoma cells (green) move on ECM fibres (purple) and do not seem to be constrained by the ECM networks. a. A low-magnification image that shows, in the lower third of the image, single carcinoma cells (arrows) invading away from the central tumour mass and accompanying ECM fibres (arrowheads). b. A higher-magnification image visualized by second-harmonic generation that shows carcinoma cells (arrows) in a tumour contacting collagen-containing fibres. Arrowheads point to cellmatrix interactions. Scale bar = 25µm. From (Wang et al 2002)

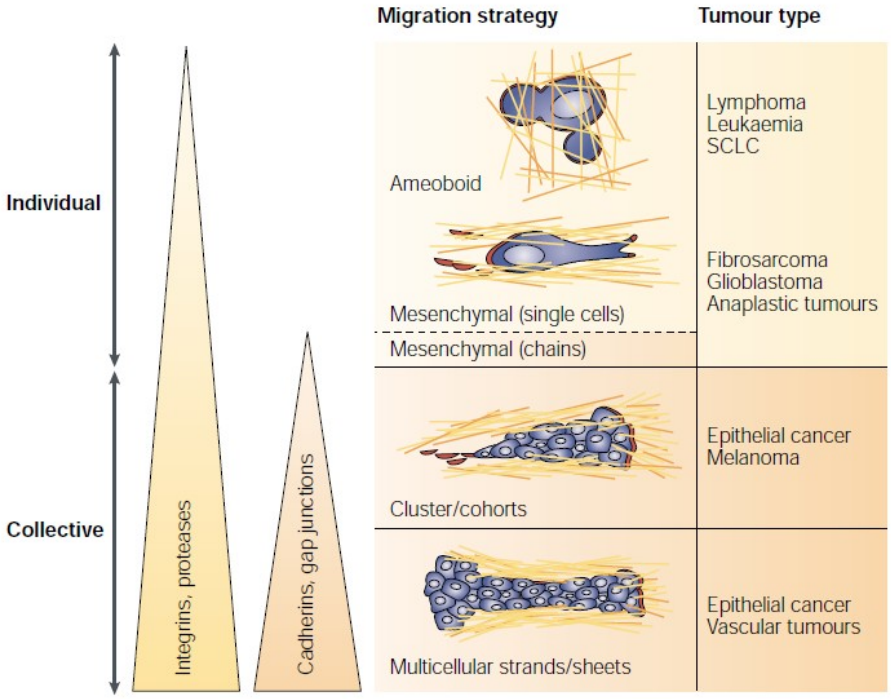

Figure 1.9: Diversity of tumour invasion mechanisms. Individual or collective tumour-cell migration strategies are determined by different molecular programmes (triangles). From individual (top) to collective (bottom) movements, increased control of cellECM interaction is provided by integrins and matrix-degrading proteases. Cellcell adhesion through cadherins and other adhesion receptors, as well as cellcell communication, via gap junctions, are specific characteristics of collective cell behaviour. Haematopoietic neoplasia (leukaemia and lymphoma) and small-cell lung carcinoma (SCLC) cells have been shown to undergo amoeboid behaviour. By contrast, mesenchymal-type migration occurs in sarcomas and glioblastomas. Detached and disseminating cell collectives (clusters or cohorts) are observed in epithelial cancers that retain high or intermediate levels of differentiation, such as breast and colon carcinoma, prostate cancer, as well as melanoma. Multicellular strands and sheets that do not detach are invasive, yet rarely metastatic. These occur in some epithelial cancers, including basal-cell carcinomas and benign vascular tumours. From (Friedl and Wolf 2003).

Oxygen transport in tumor micro-environment

Quantifying the dynamic oxygen distribution at a micro level is another necessity that would contribute to the understanding of tumor growth. Developments during the last 40 years including studies of oxygen gradients in arterioles, capillaries, venules, the capillary wall and surrounding tissues have been reviewed (Pittman 2011b, 2013). With regard to the motility of TCs, Friedl and wolf had described in detail the diverse patterns of migration and invasion that occur Friedl and Wolf 2003, and had experimentally demonstrated that TCs are particularly adept at amoeboid movement, which can lead to a high rate of metastasis (Allen and Allen 1978; Condeelis et al 1992).

Tissue fluid with varying permeability

In the tumor micro-environment, TCs will fill the pores with the growth of TCs. Therefore, the porosity of this specific tumor micro-environment varies with the concentration of TCs, and the permeability coefficient of tissue fluid and the diffusion coefficient of oxygen also would vary with the increase of TCs. Considering the tumor micro-environment with the varying porosity that is very important for studying the growth of avascular growth.

1.2.4 The theoretical studies of avascular tumor growth

Specific models of TC invasion have been discrete, where cells are considered as individual identities, or continuous, using reaction-diffusion equations, or a hybrid of both models, and have been used to explain diverse aspects of tumor growth dynamics (Frieboes et al 2010;Mahmood et al 2011). Most continuous models of avascular tumors describe the malignant mass as a homogeneous and viscous fluid, and employ reaction-diffusion-advection equations to predict the distribution and transportation of nutrients and cells (Roose et al 2007) Generally, the formulation of mathematical models for the growth kinetics of avascular tumors has been based on the availability of experimental data. These models, which have received much attention, investigate the one-dimensional growth of a single population of tumor cells with constant density, but they are insufficient for the systematic understanding of the complex mechanism of avascular tumor growth, such as the interactions between TCs and various chemical factors. Lately, more sophisticated and realistic models have been developed, incorporating higher spatial dimensions, cell movement, cellular heterogeneity (Perfahl et al 2011;Preziosi and Vitale 2011) and intracellular mechanical interactions and in-

teractions of cells with the tissue fluid pervading the ECM (Roose et al 2003)–these have discussed and demonstrated the importance of cell-cell and cell-matrix interactions (Anderson 2005;Zhang and Kim 2012;Toma et al 2012). There also have been some improved 3D numerical models to be applied in studying for a certain type of cancer. In addition, the coupled porous media models, composed of living TCs, necrotic cells, healthy cells, ECM and tissue fluid, have been extended to model tumor evolution (Scium et al 2012;Scium et al 2013) However, most of these models have not incorporated the pre-existing capillary network, which might greatly affect the dynamics of the oxygen supply to TCs. And early growth of the solid tumor within its specific capillary-tissue micro-environment causes variance in the porosity of the porous media, which affects the transportation of chemical factors and further impacts the tumor growth.

While there have been some notable success stories of the application of mathematical models to cancer biology, mathematics has much more to offer and there is still a long way to go. Since the biology and biochemistry of avascular tumor growth is highly complex and not completely understood, models have so far tended to be relatively simple, focusing on the interaction of certain generic processes. This is a necessary step as we extend our intuition and understanding of the novel types of interaction thrown up when modeling in the life sciences.

We see the role of mathematical modeling in cancer biology as twofold. On the one hand, mathematical models are able to verify (or dispute) hypothetical word models suggested by experimentalists. In this case the conclusion that a model is wrong can actually be more helpful, because it shows that the biologists should be looking for something else. Models can also help our intuition, provide a framework for thinking about a problem, and make predictions. If a model is well-parameterized, then these predictions can be quantitative, but even qualitative predictions can be significant (Roose et al 2007).

In this respect, even purely theoretical studies of mathematical models have value, not just to mathematics (such as new mathematical challenges and the development of new techniques), but also to biology (such as providing generic insight into how different mechanisms may interact, or whether different modeling assumptions are likely to lead to qualitatively different behavior).

Having said this, we feel that the field of cancer biology is now reaching a stage of maturity at which the next step in the modeling process must be the careful parameterization of some of the models so that specific experimental predictions can be made and

tested in close collaboration between experimentalists and theoreticians. As more and more biological details become available, particularly on the subcellular level as signal transduction pathways and biochemical networks are uncovered, these models are likely to become more and more complex. However, we need to guard against building overly complicated models which are poorly parameterized. While such models appear realistic, they may be little more than curve fitting, and may not give as much insight as simpler better-parameterized models.

In the future, large multi-scale models are likely to be needed, as researchers attempt to integrate detailed subcellular information to make predictions on the tumor scale (Roose et al 2007). It is not clear at present whether these models will be continuum or discrete, or a hybrid of the two, since there are problems associated with each approach.

One area where mathematics can be of assistance is in providing a bridge between discrete and continuum models through homogenization. This can be either what we might call static, in which a discrete model is homogenized to give its continuum counterpart, or what we might call dynamic, in which key pieces of information from the discrete model are needed at the continuum level, and vice versa, so that the two models are coupled.

1.3 Detection of cancer cells

1.3.1 How is cancer diagnosed?

There are some symptoms may be associated with cancer: changes in bowel or bladder habits, a sore that does not heal, unusual bleeding or discharge, thickening or lump in the breast or any other part of the body, indigestion or difficulty swallowing, obvious change in a wart or mole, or nagging cough or hoarseness. These symptoms are not always a sign of cancer. They can also be caused by less serious conditions. Only a doctor can make a diagnosis. It is important to see a doctor if you have any of these symptoms. Cancer may not cause any symptoms. This is why you should have screening tests done to find them early.

If a patient have a sign or symptom that might mean cancer, the doctor usually orders various tests and exams. These may include imaging procedures, which produce pictures of areas inside the body, endoscopy, which allows the doctor to look directly inside certain organs, and laboratory tests. In most cases, the doctor also orders a biopsy, a procedure in which a sample of tissue is removed. A pathologist examines the tissue under a microscope to check for cancer cells.

1.3.2 Cancer screening

Cancer screening aims to detect cancer before symptoms appear.[1] This may involve blood tests, urine tests, other tests, or medical imaging. The benefits of screening in terms of cancer prevention, early detection and subsequent treatment must be weighed against any harms.

Universal screening, mass screening or population screening involves screening everyone, usually within a specific age group. Selective screening identifies people who are known to be at higher risk of developing cancer, such as people with a family history of cancer.

Screening can lead to false positive results and subsequent invasive procedures (Miller et al 2009). Screening can also lead to false negative results, where an existing cancer is missed. Controversy arises when it is not clear if the benefits of screening outweigh the risks of the screening procedure itself, and any follow-up diagnostic tests and treatments.

Screening tests must be effective, safe, well-tolerated with acceptably low rates of false positive and false negative results. If signs of cancer are detected, more definitive

and invasive follow-up tests are performed to reach a diagnosis. Screening for cancer can lead to cancer prevention and earlier diagnosis. Early diagnosis may lead to higher rates of successful treatment and extended life. However, it may also falsely appear to increase the time to death through lead time bias or length time bias.

It is important to remember that when your doctor suggests a screening test, it does not always mean he or she thinks you have cancer. Screening tests are done when you have no cancer symptoms. There are different kinds of screening tests. Screening tests include the following:

Imaging

Imaging procedures that make pictures of areas inside the body. These images can be made in several ways. In many cases, the doctor uses a special dye so that certain organs show up better on film. The dye may be swallowed or put into the body through a needle or a tube.

X-rays are the most common way doctors made pictures of the inside of the body. In a special kind of x-ray imaging, a CT or CAT scan uses a computer linked to an x-ray machine to make a series of detailed pictures.

In radionuclide scanning, such as a bone scan or PET scan, the patient swallows or is given an injection of a mildly radioactive substance. A machine (scanner) measures radioactivity levels in certain organs and prints a picture on paper or films. By looking at the amount of radioactivity in the organs, the doctor can find abnormal areas.

Ultrasonography is another procedure for viewing the inside of the body.High-frequency sound waves that cannot be heard by humans enter the body and bounce back. Their echoes produce a picture called a sonogram. These pictures are shown on a monitor like a TV screen and can be printed on paper.

In MRI, a powerful magnet linked to a computer is used to make detailed pictures of areas in the body. These pictures are viewed on a monitor and can also be printed.

Endoscopy

Endoscopy means looking inside and typically refers to looking inside the body for medical reasons using an endoscope, an instrument used to examine the interior of a hollow organ or cavity of the body. Unlike most other medical imaging devices, endoscopes are inserted directly into the organ. Endoscope can also refer to using a bore-scope in technical situations where direct line of-sight observation is not feasible.

Endoscopy allows the doctor to look into the body through a thin, lighted tube called an endoscope. The exam is named for the organ involved (for example, colonoscopy to look inside the colon). During the exam, the doctor may collect tissue or cells for closer examination.

Laboratory Tests

Medical procedures that test samples of tissue, blood, urine, or other substances in the body. Although no single test can be used to diagnose cancer, laboratory tests such as blood and urine tests give the doctor important information. If cancer is present, the lab work may show the effects of the disease on the body. In some cases, special tests are used to measure the amount of certain substances called tumor markers in the blood, urine, and other body fluids, or tumor tissue. The levels of these substances may become abnormal when certain kinds of cancer are present.

Biopsy

An exam of the body to check general signs of health, including checking for signs of disease, such as lumps or anything else that seems unusual. A history of the patients health habits and past illnesses and treatments will also be taken. The physical exam, imaging, endoscopy, and lab tests can show that something abnormal is present, but a biopsy is the only sure way to know whether the problem is cancer. In a biopsy, the doctor removes a sample of tissue from the abnormal area or may remove the whole tumor. A pathologist examines the tissue under a microscope. If cancer is present, the pathologist can usually tell what kind of cancer it is and may be able to judge whether the cells are likely to grow slowly or quickly.

Staging

When cancer is found, the patient's doctor needs to know the stage, or extent, of the disease to plan the best treatment. The doctor may order various tests and exams to find out whether the cancer has spread and, if so, what parts of the body are affected. In some cases, lymph nodes near the tumor are removed and checked for cancer cells. If cancer cells are found in the lymph nodes, it may mean that the cancer has spread to other organs.

1.3.3 Risks and benefits

However, medical screening for cancer is controversial in cases when it is not yet known if the test actually saves lives. Screening can lead to substantial false positive result and subsequent invasive procedures (Miller et al 2009). The controversy arises when it is not clear if the benefits of screening outweigh the risks of follow-up diagnostic tests and cancer treatments. Cancer screening is not indicated unless life expectancy is greater than five years and the benefit is uncertain over the age of 70 (Spalding and Sebesta 2008). Several factors are considered to determine whether the benefits of screening outweigh the risks and the costs of screening. These factors include:

- Possible harms from the screening test: Some types of screening tests, such as X-ray images, expose the body to potentially harmful ionizing radiation. There is a small chance that the radiation in the test could cause a new cancer in a healthy person. Screening mammography, used to detect breast cancer, is not recommended to men or to young women because they are more likely to be harmed by the test than to benefit from it. Other tests, such as a skin check for skin cancer, have no significant risk of harm to the patient. A test that has high potential harms is only recommended when the benefits are also high.

- The likelihood of the test correctly identifying cancer: If the test is not sensitive, then it may miss cancers. If the test is not specific, then it may wrongly indicate cancer in a healthy person. All cancer screening tests produce both false positives and false negatives, and most produce more false positives. Experts consider the rate of errors when making recommendations about which test, if any, to use. A test may work better in some populations than others. The positive predictive value is a calculation of the likelihood that a positive test result actually represents cancer in a given individual, based on the results of people with similar risk factors.

- The likelihood of cancer being present: Screening is not normally useful for rare cancers. It is rarely done for young people, since cancer is largely a disease found in people over the age of 50. Countries often focus their screening recommendations on the major forms of treatable cancer found in their population. For example, the United States recommends universal screening for colon cancer, which is common in the US, but not for stomach cancer, which is less common; by contrast, Japan recommends screening for stomach cancer, but not colon cancer,

which is rarer in Japan. Screening recommendations depend on the individual's risk, with high-risk people receiving earlier and more frequent screening than low-risk people.

- Possible harms from follow-up procedures: If the screening test is positive, further diagnostic testing is normally done, such as a biopsy of the tissue. If the test produces many false positives, then many people will undergo needless medical procedures, some of which may be dangerous.

- Whether suitable treatment is available and appropriate: Screening is discouraged if no effective treatment is available. When effective and suitable treatment is not available, then diagnosis of a fatal disease produces significant mental and emotional harms. For example, routine screening for cancer is typically not appropriate in a very frail elderly person, because the treatment for any cancer that is detected might kill the patient.

- Whether early detection improves treatment outcomes: Even when treatment is available, sometimes early detection does not improve the outcome. If the treatment result is the same as if the screening had not been done, then the only screening program does is increase the length of time the person lived with the knowledge that he had cancer. This phenomenon is called lead-time bias. A useful screening program reduces the number of years of potential life lost (longer lives) and disability-adjusted life years lost (longer healthy lives).

- Whether the cancer will ever need treatment: Diagnosis of a cancer in a person who will never be harmed by the cancer is called over-diagnosis. Over-diagnosis is most common among older people with slow-growing cancers. Concerns about over-diagnosis are common for breast and prostate cancer.

- Whether the test is acceptable to the patients:If a screening test is too burdensome, such as requiring too much time, too much pain, or culturally unacceptable behaviors, then people will refuse to participate. Cost of the test: Some expert bodies, such as the U.S. Preventive Services Task Force, completely ignore the question of money. Most, however, include a cost-effectiveness analysis that, all else being equal, favors less expensive tests over more expensive tests, and attempt to balance the cost of the screening program against the benefits of using those funds for other health programs. These analyses usually include the total cost of the screening program to the health-care system, such as ordering the test,

performing the test, reporting the results, and biopsies for suspicious results, but not usually the costs to the individual, such as for time taken away from employment.

- The extent to which a cancer is treatable: if a person has a low life expectancy or otherwise is in the end stages of a chronic condition, then such a patient may have a better life by ignoring the cancer even if one were found. If the diagnosis of cancer would not result in a change in care then cancer screening would not likely result in a positive outcome. Over-diagnosis in this case occurs, for example, in patients with end-stage renal disease and organizations recommend against cancer screening for such patients (Chertow et al 1996).

1.4 MDEs – a novel bio-markers for early cancer diagnosis

1.4.1 MDEs family

Numerous experiments have proved that matrix-degrading enzymes (MDEs) can degrade extracellular matrix (ECM) components, causing tumor cells (TCs) to become detached from the primary tumor. MMPs are the major components of MDEs, and increased levels of several MMPs have been reported in the body fluids of cancer patients (Hadler-Olsen et al 2013). The MMPs are a family of structurally and functionally related endoproteinases that are collectively capable of degrading the ECM. Evidence suggests that MMPs also have "sheddase" activity, giving them the ability to release bioactive molecules form the cell surface. This further increases the number of potentially relevant substrates, making MMPs ideal candidates from molecules that mediate host: tumor interactions. MMPs were classically thought to contribute to tumor metastasis via their MDEs activity, but in recent years studies have implicated MMPs at virtually all stages of tumor progression from initial development of the tumor, growth, angiogenesis, invasion, and metastasis and growth at the secondary site (Fingleton 2003).

There are abundant data to show that MMPs are over-expressed in multiple tumor types when compared to normal tissues. These studies are not ideal, but for guiding the targeting a certain MMP in cancer. In these instances, the up-regulation of the MMP in question may be just a secondary effect of remodeling of matrix or growth characteristics of the tumor. However, in cases in which increased MMP levels have been shown to be strong indicators of a negative diagnosis, it is more likely that targeting those enzymes will impact tumor progression.

1.4.2 Roles of MMPs in cancer

In most organs, the principle components of the ECM are collagens and numerous other proteins including laminin, entactin, and proteoglycans that make up the basement membrane. Tumor cells over-express proteases and/or induce expression of these enzymes in neighboring stromal cells in order to degrade the basement membrane and invade the surrounding tissue. Several MMPs have been implicated in the ECM degradation associated with tumor growth and angiogenesis. This proteolytic activity is also required for a cancer cell to invade a nearby blood vessel (intravasation) and then extravasate at a distant location and invade the distant tissue in order to seed a new metastatic site, presented in Fig.1.10.

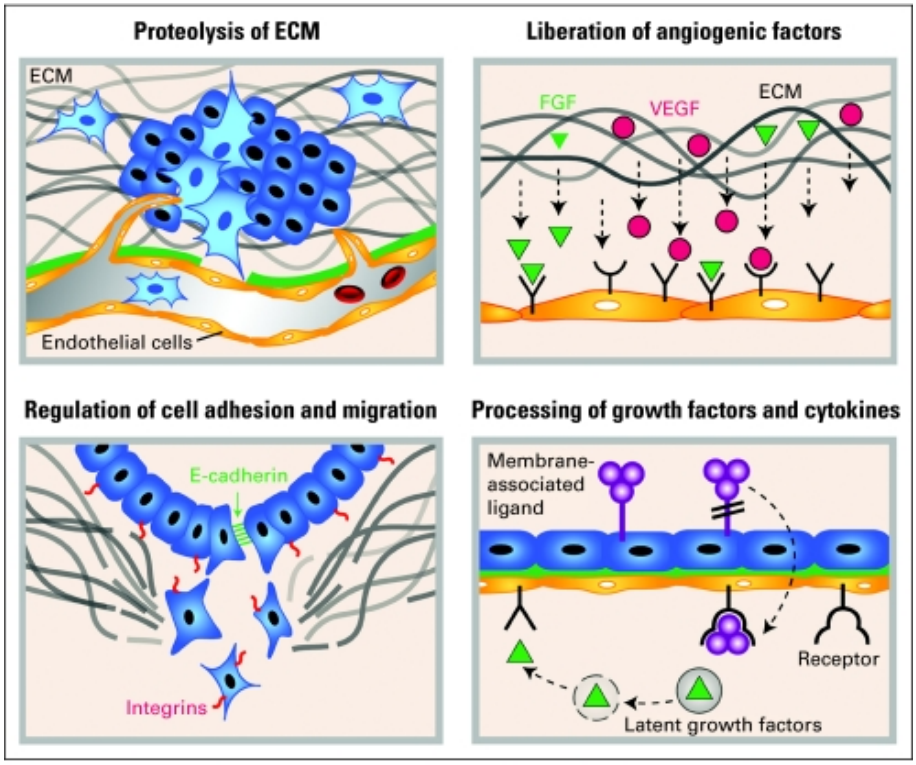

Figure 1.10: Multiple functions of MMPs in cancer progression. (counterclockwise) MMPs degrade components of ECM, facilitating angiogenesis, tumor cell invasion, and metastasis. MMPs modulate the interactions between tumor cells by cleaving E-cadherin, and between tumor cells and ECM by processing integrins, which also enhances the invasiveness of tumor cells. MMPs also process and activate signaling molecules, including growth factors and cytokines, making these factors more accessible to target cells by either liberating them from the ECM (eg, vascular endothelial growth factor and basic fibroblast growth factor) and inhibitory complexes (eg, transforming growth factor-), or by shedding them from cell surface (Roy et al 2009).

1.4.3 MMPs as diagnostic factor for cancer

To date, many bio-markers have been used as cancer diagnosis tools; among these markers, matrix metalloproteinases (MMPs), a family of proteolytic enzymes, have been proposed as potential diagnostic markers for early detection in cancer patients (Roy et al 2009; Campbell et al 2010; Hadler-Olsen et al 2013). Large amount of date have been obtained relating to MMP over-expression in various tumor types when compared to normal tissues, and several studies have studied that certain MMPs in specific cancers can be useful as indicators of disease progression, thereby improving management of specific cancers.

Liotta et al (1980) suggested that the measured level of MMP activity might serve as an in vitro biochemical marker for the metastatic potential of malignant cells. Over the last decade, several studies have assessed the diagnostic value of MMP-2, MMP-7 and MMP-9 for various cancers (Hurst et al 2007; Roy et al 2008; Mroczko et al 2009; Shpitzer et al 2009; Patel et al 2011; Wang et al 2014). All these experimental studies reported that the measured levels of MMPs in body fluids are higher in cancer patients when compared with those of the healthy control individuals. However, despite a huge number of studies, it has been difficult to establish MMPs as cancer biomarkers until now, mainly because of the complex multi-functional behavior of their components and the fact that the same MMPs are unregulated in many different types of cancer (Hadler-Olsen et al 2013), as presented as below.

Breast cancer

Evidence is emerging that members of the MMP family can serve not only as potential markers for diagnosis and prognosis, early detection, and risk assessment, but also as indicators of tumor recurrence, metastatic spread, and response to primary and adjuvant therapy for breast cancer (Wu et al 2008;Rocca et al 2004;Moses et al 1998).

Pancreatic cancer

Nowhere is the need more urgent for sensitive and specific bio-markers for early diagnosis and to screen high-risk patients than in pancreatic cancer. This disease is extremely difficult to diagnose in its early stages due to a lack of specific symptoms and the limitations of current diagnostic methods. Several studies have evaluated differentially expressed bio-markers for pancreatic cancer using tissue, blood, or pancreatic juice. Serum and tissue levels of MMP-9 are significantly higher in patients with pan-

creatic ductal adenocarcinoma than in patients with chronic pancreatitis and healthy controls (Tian et al 2008). Similarly, plasma as well as tumor tissues from patients with pancreatic ductal adenocarcinoma have significantly elevated MMP-7 levels (KF et al 2007) which may predict shortened survival of patients.

Lung cancer

Several studies have reported that plasma and/or serum levels of MMP-9 and TIMP-1 are elevated in patient with stage III or IV lung cancer when compared with those in patients with nonmalignant lung diseases (Jumper et al 2004;Ko et al 2006). Several single nucleotide polymorphisms within the MMP-1 gene have been shown to be significantly associated with the risk of early-onset lung cancer in particular for subgroups with high smoking intensity (Sauter et al 2008).

Bladder cancer

As is expected, a majority of the bio-marker studies in patients with bladder cancer have focused on urine. Studies from our group and others have shown that urinary MMP-2 and MMP-9 levels correlate with presence of bladder cancer as well as stage and grade of disease (Gerhards et al 2001;R et al 2008;Eissa et al 2003).

Colorectal cancer

serum MMP-7 levels were reported to predict decreased survival in patients with advanced colorectal cancer (Maurel et al 2007). A study of paired colorectal tumor and normal mucosal tissues revealed the significant correlation between MMP-1 levels and pathology (Baker and Leaper 2003).

Ovarian cancer

Elevated plasma MMP-2 levels have also been shown to correlate with lymph node metastasis (Langenskild et al 2005). Enhanced MMP-9 staining in primary tumors was found to be an independent marker of poor prognosis in a study with T3-T4 node-negative patients (Langenskild et al 2005).

Prostate cancer

MMP-2, -9, -15, and -26 expression in tissue or serum have been positively correlated with Gleason score in prostate cancer(Riddick et al 2005;Wood et al 1997).

Among these MMPs, the activities of plasma MMP-2 and -9 increased significantly in metastatic prostate cancer (Morgia et al 2005).

Brain tumor

Elevated tissue levels of MMP-2 and MMP-9 have been reported in aggressive brain tumors (Jlinoj et al 2000;Rao et al 1996;Choe et al 2002). Positive MMP-2 expression in tissue was also associated with shorter survival in patients with malignant brain tumors (Jlinoj et al 2000).

The context in which these or any other bio-markers are utilized in the clinic is a critical consideration. It has been suggested that, rather than being used as screening tools, MMPs might best be used to provide useful clinical information as part of a longitudinal assessment of a patient's disease progression and therapeutic efficacy with the patient himself/herself serving as an internal control.

1.4.4 Theoretical studies for MDEs as a cancer factor

There have also been theoretical efforts to develop models of avascular tumors with continuous and discrete individual approaches (Frieboes et al 2010; Mahmood et al 2011). Most continuous avascular tumor models describe the malignant mass as a homogeneous viscous fluid, and use reaction-diffusion-advection equations (Roose et al 2007). These models, which have received considerable attention, only investigate the one-dimensional growth of a single population of tumor cells with constant density. Recently, more sophisticated and realistic models have been developed that incorporate higher spatial dimensions, cell movement, cellular heterogeneity (Perfahl et al 2011; Preziosi and Vitale 2011; Scium et al 2012; Scium et al 2013), intracellular mechanical interactions, and interactions of cells with the tissue fluid that pervades the ECM (Anderson 2005; Zhang and Kim 2012; Toma et al 2012). However, most of these models have not incorporated the pre-existing capillary network, which greatly affects the dynamics of the oxygen supply to the TCs. Furthermore, early growth of a solid tumor within its specific capillary-tissue micro-environment causes variance in the porosity of the porous media, which then affects the transportation of chemical factors and further affects tumor growth. This process has not yet been fully and systematically studied.

Therefore, the mathematical model presented here incorporates a specific micro-environment for avascular tumor growth in a novel manner and couples the convection-diffusion of MDEs and oxygen. Based on this theoretical model, this paper aims to investigate the diffusion of MDEs in the micro-environment of the avascular tumor, and,

particularly within the capillaries, to predict the diagnostic value of MDEs as cancer bio-markers.

Chapter 2.

A 3D mathematical coupled model for the transport of oxygen in microcirculation

At first, we numerically simulated the transport of oxygen in microcirculation, i.e. oxygen exchanges between capillaries and tissues, and aimed at examining the effect of convection-diffusion of oxygen on oxygen transport at this level of micro-circulation. For this, we developed a more comprehensive mathematical coupled model, taking account of the solid deformation of capillaries and their surrounding tissues, the seepage of tissue fluid, the molecular diffusion of oxygen, and the convection-diffusion of oxygen within capillary as well within tissues.

2.1 Abstract

This present study models solid deformation of both capillary and tissue resulting from capillary fluctuation, and couples this into the seepage of tissue fluid, then uses their seepage velocity to calculate the convection-diffusion of oxygen in microcirculation. This 3D mathematical model is based on a porous media theory and focuses to examine the effect of deformation, seepage and convection on oxygen transport quantitatively, which have not been paid enough attention in the previous studies. The results indicate that (1) solid deformation appears more significant in the middle of capillary, where the maximum value of volumetric deformation reaches about 0.5%; (2) solid deformation can help tissue fluid to flow more uniformly, also can help oxygen to be transported more uniformly, eventually has an increase in the oxygen concentration by 0.1%$\sim$0.5%; (3) convection-diffusion given by coupled deformation and seepage model has a 16% maximum, 3% average increase in oxygen concentration than by the pure diffusion model, and has a greater effect in the middle of capillary than near the ends of capillary; (4) convection-diffusion allows oxygen to be transported more uniformly; (5) larger values of permeability coefficient, or smaller values of the diffusion coefficient produce a more obvious effect on oxygen transport.

2.2 General Coupled Mathematical Model with Solid Deformation, Fluid Seepage, and Convection–Diffusion and Molecular Diffusion

A general coupled mathematical model for solute transport in microcirculation with solid deformation, fluid seepage, and convection–diffusion and molecular diffusion of a solute is developed below.

2.2.1 Basic assumptions

Based on the physiological regulations of oxygen transport in the microcirculation, the following assumptions are proposed:

1. The computational domain is modeled as a porous medium, which is assumed to be isotropic and uniform.

2. A solid scaffold in the porous medium is modelled as continuously elastic, with deformation that complies with Hooke's law.

3. The microcirculatory system is assumed to be a saturated porous medium, as the interstitial spaces are normally filled with tissue fluid.

4. The volume deformation of the saturated porous medium includes two parts: deformation of the solid framework and of the pore.(Bear 1988) Because the volume deformation of the framework is substantially smaller than that of the pore, we assume the volume deformation of the porous medium to be equal to the pore deformation.

5. The pore pressure in the tissue complies with Biot's effective stress law.

6. The fluid seepage complies with Darcy's law.

7. Mass transport by convection–diffusion and molecular diffusion follows Fick's law.

8. The microcirculatory system is considered to be a thermodynamic equilibrium system.

2.2.2 Governing equations of solid deformation

The capillary network and cells are modeled as solids, while all other phases are fluids. From assumption 2, solid deformation can be expressed by the general form of Hooke's equation:

$$\sigma_{ij}^{'} = \lambda e \delta_{ij} + 2\mu \varepsilon_{ij}, \tag{2.1}$$

$$\Theta^{'} = \sigma_{x}^{'} + \sigma_{y}^{'} + \sigma_{z}^{'} = Ke, \tag{2.2}$$

where $\sigma_{ij}^{'}$ is the effective stress tensor, ε_{ij} is the strain tensor, λ, μ are Lamé constants, e is the volumetric deformation, δ_{ij} is the Kronecker tensor, K is the volume modulus, $\Theta^{'}$ is the effective volume stress, and $\sigma_{x}^{'}, \sigma_{y}^{'}, \sigma_{z}^{'}$ represent the effective stress in the x, y, and z directions, respectively. From assumption 5, the total stress can be expressed as

$$\sigma_{ij} = \sigma_{ij}^{'} + \alpha p \delta_{ij}. \tag{2.3}$$

The stress equilibrium can be written as

$$\sigma_{ij,j} + F_i = 0. \tag{2.4}$$

Substituting Eq. (2.3) into (2.4), we obtain

$$\sigma_{ij,j}^{'} + F_i + (\alpha p)_{,i} = 0. \tag{2.5}$$

Substituting Eq. (2.1) into (2.5), the solid deformation equation under the effect of pore pressure is expressed by the Lamé–Navier equation:

$$(\lambda + \mu) u_{i,ji} + \mu u_{i,jj} + F_i + (\alpha p)_{,i} = 0. \tag{2.6}$$

We assume that the compression strain is positive and the tensile strain is negative. λ, μ are Lamé coefficients, F_i is the external force, $\alpha = 1$ is the effective stress coefficient, p is the pore pressure, and $u_{i,j}$ is the displacement tensor. In addition, λ, μ, K can all be expressed as a function of the Youngs modulus E and Poisson ratio v of the material: $\lambda = \frac{Ev}{(1+v)(1-2v)}, \mu = \frac{E}{2(1+v)}, K = \frac{E}{3(1-2v)}$.

2.2.3 Governing equations of fluid seepage

The mass equilibrium equation per unit volume of fluid is given by

$$\operatorname{div}\left(\rho \vec{q}\right) = \frac{\partial (n\rho)}{\partial t} - W = \rho \frac{\partial n}{\partial t} + n \frac{\partial \rho}{\partial t} - W, \tag{2.7}$$

where ρ is the fluid density, t is time, n is porosity, q is the seepage velocity of fluid per unit of volume/time/area, i.e., $cm^3 s^{-1} cm^{-2} = cm/s$, and W represents a source

and sink of fluid. According to assumption 6, we have $q_i = kp_{,i}$, where p is pore pressure in Eq. (2.3) and k is the permeability coefficient. From assumptions 3 and 4, $\frac{\partial e}{\partial t} = -\frac{\partial n}{\partial t}$. According to the micro-compressibility of fluid, $\frac{\partial \rho}{\partial t} = -\beta\rho\frac{\partial p}{\partial t}$, in which β is the compressibility coefficient of water. Substituting this into Eq. (2.7), we get the fluid seepage equation under solid deformation:

$$\left(kp_{,i}\right)_{,i} = \beta n\frac{\partial p}{\partial t} + \frac{\partial e}{\partial t} + W, \tag{2.8}$$

where βn denotes the compressibility coefficient of the tissue fluid. Compared with oxygen transport models that consider only molecular diffusion, the modifications in this coupled mathematical model are as follows:

- The interaction between fluid seepage and the solid deformation of cells and capillary wall is considered, and the term $\frac{\partial e}{\partial t}$ is added to the seepage Eq. (2.8).
- The term $(\alpha p)_{,i}$ related to pore pressure is added to the solid deformation in Eq. (2.6).

2.2.4 Governing equations of convection and diffusion

From assumption 7, the diffusion flux can be expressed by Fick's tensor equation:

$$J_i = -D\frac{\partial C}{\partial x_i}, \tag{2.9}$$

where J_i is the diffusion flux tensor, C_{o_2} is the concentration of the solution as a function of time and position, and D is the diffusion coefficient. The mass conservation for oxygen in the microcirculation is given as

$$\frac{\partial C_{o_2}}{\partial t} = \frac{\partial}{\partial x_i}\left(D\frac{\partial C_{o_2}}{\partial x_i}\right) - \frac{\partial}{\partial x_i}\left(C_{o_2}V_i\right) + I, \tag{2.10}$$

where V_i denotes the seepage velocity of fluid and $V_i = q_i = kp_{,i}$. I is a source and sink term for oxygen, and is related to its solubility in fluid and its consumption. The first term on the right-hand side represents oxygen transport by diffusion, and the second term represents oxygen transport by convection.

2.2.5 Coupled model

The coupled model for oxygen transport combines Eqs. (2.6), (2.8), and (2.10):

$$\begin{aligned}
&\left(kp_{,i}\right)_{,i} = \beta n\frac{\partial p}{\partial t} + \frac{\partial e}{\partial t} + W \\
&\left(\lambda+\mu\right)u_{i,ji} + \mu u_{i,jj} + F_i + \left(\alpha p\right)_{,i} = 0, \\
&\frac{\partial C_{o_2}}{\partial t} = \left(DC_{o_2,i}\right)_{,i} - \left(C_{o_2}V_i\right)_{,i} + I.
\end{aligned} \tag{2.11}$$

All the equations expressed as tensors are solved using a finite element method (FEM).

2.3 Application of Coupled Model for Oxygen Transport

Based on the above coupled model for solute transport, this section examines the oxygen distribution in the microcirculation. We require C_{o_2} to solve Eq. (2.10), and this is calculated from the partial pressure of oxygen in plasma P_{o_2}.

2.3.1 Hemoglobin saturation

Small amounts of oxygen are carried in dissolved form in the plasma. Hemoglobin (Hb) is the primary vehicle for transporting oxygen in the blood. The relationship between the fractional saturation of Hb with oxygen S_{o_2} and the blood oxygen partial pressure P_{o_2} is given by the most common form of the two-parameter Hill's equation:

$$S_{o_2} = \frac{(P_{o_2}/P_{50})^m}{1+(P_{o_2}/P_{50})^m}, \tag{2.12}$$

where P_{50}=27.2 mmHg is the oxygen tension at 50% saturation, and $m = 2.6$ is a dimensionless exponent used in this model. When the arterial blood reaches the capillary bed, its P_{o_2} value is about 95 mmHg at the arteriole end. In interstitial tissue, P_{o_2} averages only 40 mmHg, the same value as when entering the systemic veins (Hall 2010). Therefore, we take P_{o_2}=95 mmHg at the arteriole end and P_{o_2}=40 mmHg at the venule end. The total oxygen volume concentration within the capillary vessel can be expressed as:

$$C_{o_2} = 1.39 S_{o_2} \varphi \delta + K_{o_2}(1-\varphi) P_{o_2}. \tag{2.13}$$

The first term on the right-hand side represents the concentration of oxygen bound to Hb, where $\varphi = 0.45$ is the volume concentration of red blood cells (RBCs) in the blood, $\delta = 0.25$ is the volume concentration of Hb in an RBC, and S_{o_2} is obtained from Eq. (2.12). The second term indicates that the concentration of oxygen dissolved in plasma follows Henry's Law, where K_{o_2} is the solubility of oxygen in plasma in the human body.

2.3.2 Oxygen exchange between RBC and plasma

To enable oxygen molecules to pass through the capillary wall into the tissues, oxygen bound to Hb has to dissociate from the Hb and pass through the RBC membrane into the plasma. The following assumptions about the oxygen source are proposed:

1. Reduced oxygen in suspension in RBCs for diffusion into the plasma can be supplied instantaneously by dissociation from Hb.

2. Oxygen can be transported instantaneously through the RBC membrane.

3. The Hb concentration is a constant in the process of oxygen bound to Hb and dissociated from Hb.

4. The Hb molecule is much larger than that of oxygen, so whether oxygen is absorbed by Hb or released from Hb, the diffusion coefficient of Hb remains constant.

t_0 is the initial time. Assume that C_{o_2} in plasma decreases at a rate of $\Delta C(x,t_0)$ from t_0 to t_1. C_{o_2} at t_1 can be expressed as:

$$C_{o_2}(x,t_1) = C_{o_2}(x,t_0) - \Delta C(x,t_o). \tag{2.14}$$

Because of the difference in the O_2 concentration in plasma and in surrounding tissue, O_2 is diffused from the capillaries to the tissue, and C_{o_2} in plasma decreases, i.e., $P_{o_2}(x,t_0)$ decreases to $P_{o_2}(x,t_1)$. At this time, however, O_2 in the RBCs has not yet been diffused to the plasma. According to Eq. (2.13), C_{o_2} at t_1 can therefore be expressed as:

$$C_{o_2}(\mathrm{x},t_1) = 1.39 S_{o_2}(P_{o_2}(x,t_0))\varphi\delta + K_{o_2}(1-\varphi)P_{o_2}(\mathrm{x},t_1). \tag{2.15}$$

From assumptions 1 and 2, the blood oxygen partial pressure at t_1 re-balances instantaneously, denoted by $P'_{o_2}(\mathrm{x},t_1)$. Therefore, C_{o_2} at t_1 can also be expressed as:

$$C_{o_2}(\mathrm{x},t_1) = 1.39 S_{o_2}\left(P'_{o_2}(x,t_1)\right)\varphi\delta + K_{o_2}(1-\varphi)P'_{o_2}(\mathrm{x},t_1). \tag{2.16}$$

Combining Eq. (2.15) and (2.16), we obtain an equation for P'_{o_2}. This can be solved using an iterative method to calculate the value of $P'_{o_2}(\mathrm{x},t_1)$. An iterative method is feasible here, because the numerical relative error for iterations at t_1 is only 0.004345%, well within the margin of error. Then, $P'_{o_2}(x,t_1)$ is used as the new value of $P_{o_2}(x,t_1)$ to find C_{o_2} at t_2. It has been demonstrated that RBCs cause a large deformation in the capillaries (Morsi et al 1999), which also indicates that blood flows slowly in the capillaries. Therefore, in theory, the inertial force term can be neglected and a porous media model can be applied. For the issue of oxygen transport, the flow of RBCs is assumed to be uniform with respect to blood in the capillaries.

2.3.3 Source and sink of oxygen

Two essential parameters must be considered to solve the oxygen transport problem: the density of cells and the oxygen consumption rate. Cells are known to consume

oxygen at a rate of $6.25 \times 10^{-17} M\,cells^{-1}\,s^{-1}$ (Casciari et al 1992), and we assume the density of tumor cells in tissue to be $6.7 \times 10^{7} cells\,ml^{-1}$ (Anderson 2005), Because 1 M of oxygen occupies 22400 ml, we can calculate that $C_{used\,O_2} = 6.25 \times 10^{-17} \times 6.7 \times 10^{7} \times 22400 = 9.38 \times 10^{-5} \mathrm{ml\,O_2\,ml^{-1}\,tissue\,s^{-1}}$. Because the density of cells in tissue and the oxygen consumption rate will vary in different organs, and even between normal cells and tumor cells, we assume the oxygen consumption rate for normal body cells, $c_{used_{o_2}} = 5.38 \times 10^{-5} \mathrm{ml\,O_2\,ml^{-1}\,tissue\,s^{-1}}$. This mathematical model is solved by an FEM in which each element represents a volume unit, rather than a single cell.

2.3.4 Capillary fluctuation

Capillary fluctuations act as the source of power for solid deformation. There are several time scales of pressure variation within a given capillary. First, there are cardiac oscillations, which can be observed throughout the length of the capillary. Their normal amplitude is about $0.01 \sim 0.02 \times 10^{4} \mathrm{Nm^{-2}}$ (Type I). The propagation of these oscillations through the microcirculation is discussed below. The second form of these fluctuations lasts for 15–20 s and is associated with pressure variations in the region of $0.04 \sim 0.07 \times 10^{4} \mathrm{Nm^{-2}}$; the pattern of such changes is random (Type II). The third type of pressure variation is more substantial and long-lasting; it is in the region of $0.13 \times 10^{4} \mathrm{Nm^{-2}}$ and occurs over a period of 5–8 min, followed by a return to the steady state condition in about 2–3 min (Type III) (Zweifach 1974;Caro et al 2012).

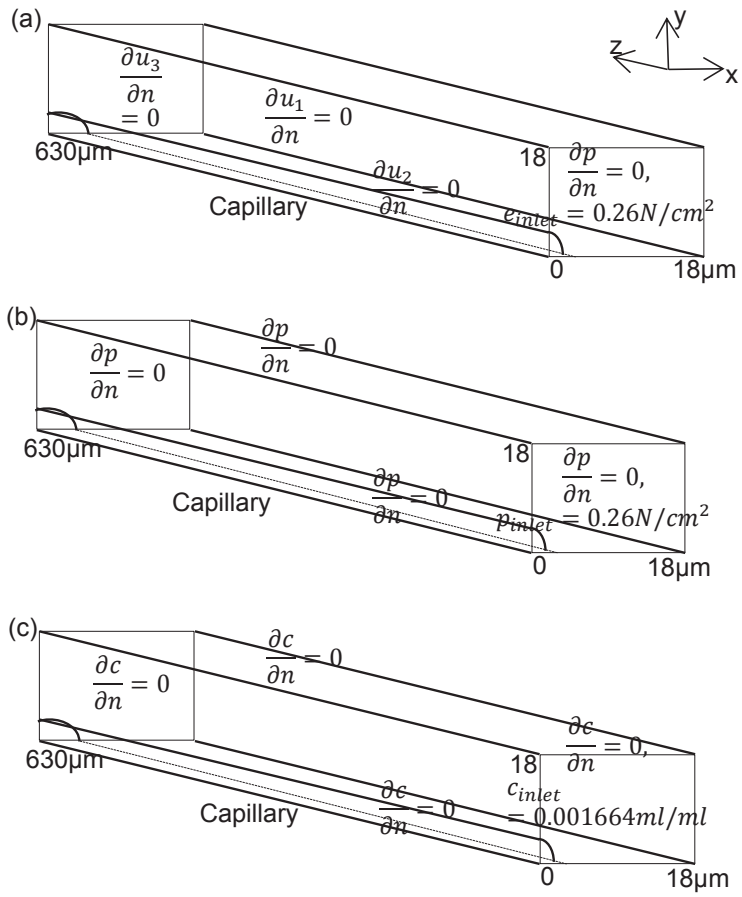

Figure 2.1: Geometry and physical condition of (a) solid deformation model (b) seepage model (c) convection–diffusion and molecular diffusion model.

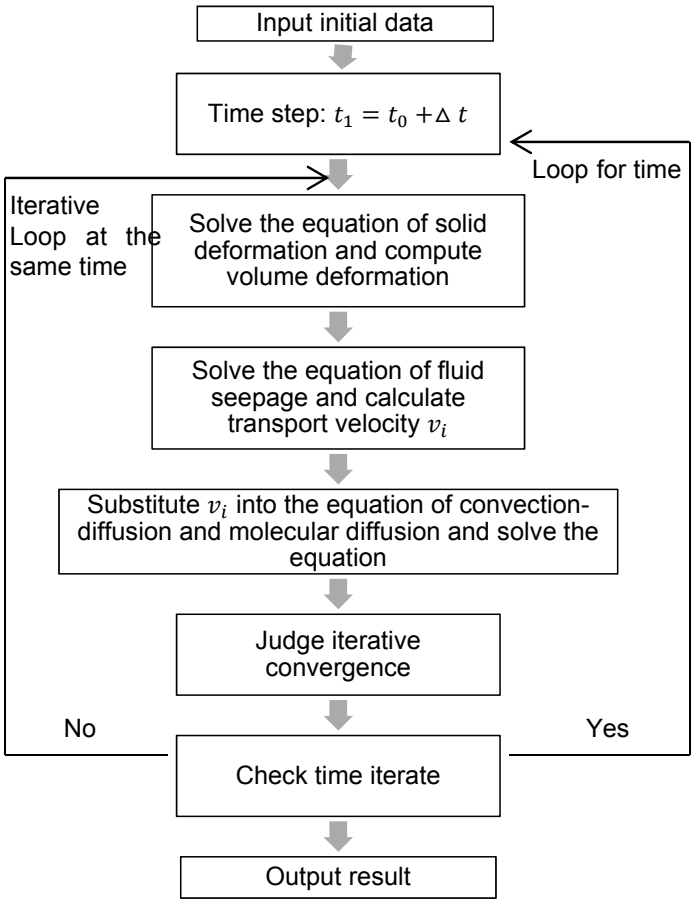

Figure 2.2: Flowchart of the FEM program for time-dependent oxygen transport, where $\Delta t = 0.0625$ s and $t_0 = 0$.

2.4 Numerical simulation of oxygen transport by the coupled model

2.4.1 Geometry and boundary condition of the model

Krogh first proposed a parallel capillary-tissue cylinder arrangement in the microcirculatory region (Krogh 1919a). This classic model has been widely applied to study many microcirculation problems in which the capillaries are parallel and evenly arranged, and each section of capillary is responsible for the oxygen supply of a corresponding neighboring section of the surrounding tissue. Based on this, we consider the geometric structure as parallel capillaries surrounded by tissue fluid. By assuming the geometric structure of the capillary network to be symmetrical, we take the computational area to be a cuboid including a quarter of a capillary section and the corresponding surrounding tissue, where the z-axis represents the length of the capillary and the x-axis represents half of the distance between two adjacent capillaries. The radius of the capillary is 3 μm, the thickness of the capillary wall is 0.3 μm, the distance between two adjacent capillaries is 36 μm, and the length of each capillary is 630 μm. To model the phenomenon of oxygen supply more realistically, we incorporate the arteriole end and the venule end.

The geometry and boundary conditions of the physical model are shown in Fig. 2.1: for the solid deformation model, the normal displacement on all six surfaces is zero; for the seepage model, the permeability flux is assumed to be zero on all six surfaces, i.e., $\frac{\partial p}{\partial n} = 0$; for the convection–diffusion and molecular diffusion model, the normal derivative of oxygen concentration $\frac{\partial C_{o_2}}{\partial n} = 0$ on all six surfaces. At the arteriole end of the capillary, $P_{t_0} = 0.26\mathrm{N/cm^2}$ in the x, y, and z-axis directions of the nodes, and $C_{o_2}(t_0) = 0.001664\mathrm{cm^3/cm^3}$ (calculated from Eq. (2.13)).

2.4.2 Finite element method

To solve these coupled equations, we use an FEM to compute their discrete solutions, and control relative error for iterations less than 0.005%, which are programmed in-house code designed by Fortran 90 in single-precision floating-point format. A flowchart of the program is shown in Fig. 2.2. The computation is carried on a 3D domain measuring 18×18×630 μm, which is divided into 9×9×13 hexahedron meshes. Numerical tests using grids of twice the resolution gave only a small improvement in accuracy (relative error was less than 1/100). For the time terms, a forward difference method was applied with a time step of 1/16 s. As described in Sect. 2.3.4, the present

Table 2.1: Parameters used in this mathematical model

Parameter	Description	Value	Unit
k_t:a	Permeability coefficient in tissue	$8 \times 10^{-6} \sim 8 \times 10^{-8}$	$\mathrm{cm\,s^{-1}}$
k_w:a	Permeability coefficient at capillary wall	$2 \times 10^{-6} \sim 2 \times 10^{-8}$	$\mathrm{cm\,s^{-1}}$
k_c:a	Permeability coefficient in the capillary	0.005	$\mathrm{cm\,s^{-1}}$
p_{inlet}(I):b	Pressure at inlet end under type I	0.026	$\mathrm{N\,cm^{-2}}$
p_{inlet}(II):b	Pressure at inlet end under type II	0.065	$\mathrm{N\,cm^{-2}}$
p_{inlet}(III):b	Pressure at inlet end under type III	0.13	$\mathrm{N\,cm^{-2}}$
$p_{t_0} : b$	Initial pore pressure	0.26	$\mathrm{N\,cm^{-2}}$
D_t:c	Diffusion coefficient in tissue	$2 \times 10^{-5} \sim 2 \times 10^{-7}$	$\mathrm{cm^2\,s^{-1}}$
D_w:c	Diffusion coefficient at capillary wall	$10^{-5} \sim 10^{-7}$	$\mathrm{cm^2\,s^{-1}}$
D_c:c	Diffusion coefficient in the capillary	0.0003	$\mathrm{cm^2\,s^{-1}}$
n_0:e	Initial porosity	0.35	dimensionless
K_{O_2}:e	Oxygen solubility of blood at 37°C, 1atm	0.023	$\mathrm{ml\,ml^{-1}\,(atm)^{-1}}$
$c_{used_{o_2}}$:c	Oxygen consumption rate in tissues	5.38×10^{-5}	$\mathrm{ml\,O_2\,ml^{-1}\,tissue\,s^{-1}}$
$P_{o_2}(t_0)$:d	initial oxygen partial pressure	100	mmHg
E_t:e	Young modulus in tissue	10.0	$\mathrm{N\,cm^{-2}}$
E_w:e	Young modulus at capillary wall	20.0	$\mathrm{N\,cm^{-2}}$
E_c:e	Young modulus in capillary	0.05	$\mathrm{N\,cm^{-2}}$
v:e	Poisson ratio	0.45	dimensionless
Δt	Time step	0.0625	s
$n\beta$:e	compressibility coefficient of tissue fluid	10^{-7}	dimensionless
α:e	effective stress coefficient	1	dimensionless

a: Chapman et al 2008; He and Himeno 2012, b: Zweifach 1974, c: Anderson 2005, d: Hall 2010, e: Bear 1988

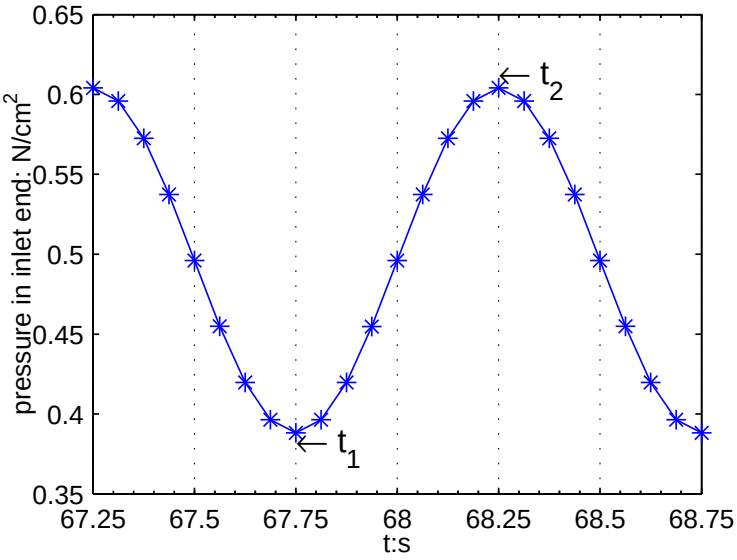

(a) capillary fluctuation, $k_1 = 8 \times 10^{-6}$

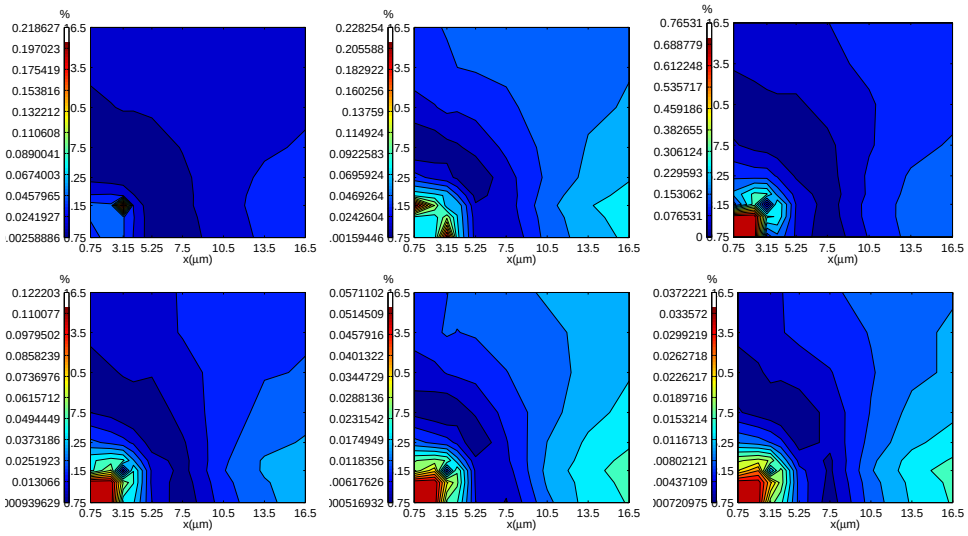

(b) volumetric deformation between t_1 and t_2, $k_1 = 8 \times 10^{-6}$

model considers capillary fluctuations as a power source, so the wave pattern of fluctuations must be represented accurately and completely. Some numerical tests were also carried out to determine an appropriate time step. The results indicate that the wave pattern of the fluctuations can be represented well at 1/16 s, but there is only a small difference (relative error of 0.5%) when using 1/32 s. Thus, we select a time step of 1/16 s for the entire computational process. These comparisons with different grid sizes and time steps indicate that the numerical methods are valid and feasible. The parameters used to solve this mathematical model are shown in Table 2.1. All of the numerical results are stable and have converged.

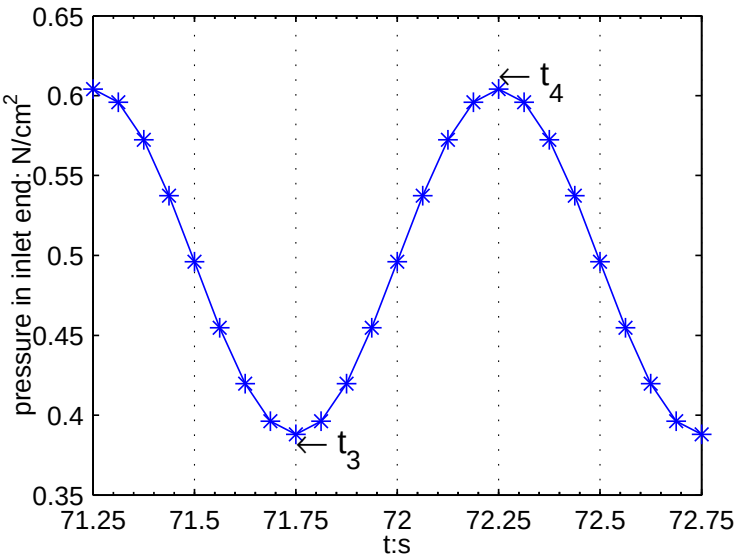

(c) capillary fluctuation, $k_1 = 8 \times 10^{-7}$

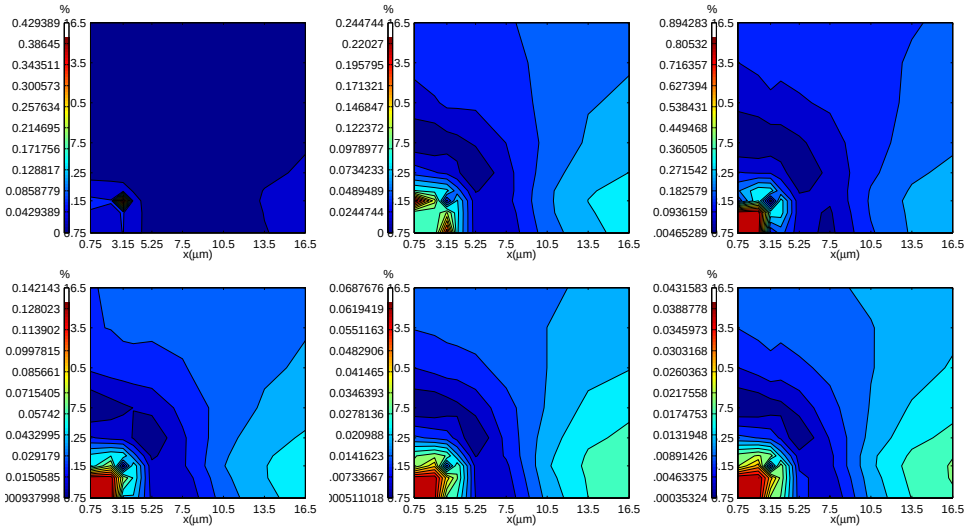

(d) volumetric deformation between t_3 and t_4, $k_1 = 8 \times 10^{-7}$

Figure 2.3: The effect of capillary fluctuation on volumetric deformation: the pressure in the inlet end of capillary over time, when (a) $k_1 = 8 \times 10^{-6}$, (c) $k_1 = 8 \times 10^{-7}$; the percentage of volumetric deformation under the impact of capillary fluctuation in some x-y slices (b) at z=225μm, z=275μm, z=325μm, z=375μm, z= 425μm, z= 475μm (left to right, and top to bottom), from t_1 to t_2 shown in (a), when $k_1 = 8 \times 10^{-6}$, (d) at z=225μm, z=275μm, z=325μm, z=375μm, z= 425μm, z= 475μm (left to right, and top to bottom), from t_3 to t_4 shown in (b), when $k_1 = 8 \times 10^{-7}$. The unit of k is $\mathrm{cm\,s^{-1}}$.

2.5 Results

2.5.1 The numerical results for solid deformation

Volumetric deformation under capillary fluctuation

In this present model, we coupled solid deformation into seepage and obtained the results of seepage velocity from the coupled deformation and seepage model, then use the seepage velocity as the velocity for convection-diffusion to calculate the oxygen concentration.

As described in Sect. 2.3.4, the present model considers capillary fluctuations as a power source, so the wave pattern of fluctuations must be represented accurately and completely. Some numerical tests were also carried out to determine an appropriate time step. The results indicate that the wave pattern of capillary fluctuations can be simulated well at 1/16 s, but there is only a small difference (relative error of 0.5%) when using 1/32 s. Thus, we select a time step of 1/16 s for the entire computational process, and the pressure in the inlet end of capillary over time which can represent the wave pattern of capillary fluctuation is shown in Fig.2.3a,b, where two couples of time are marked, i.e. t_1, t_2 and t_3, t_4, representing the pressure under the impact of capillary fluctuation from trough to peak. Correspondingly, the relative volumetric deformation distributions from t_1 to t_2 and t_3 to t_4 are presented by percentage in Fig.2.3c,d. This clearly indicates that capillary fluctuation has a greater effect on volumetric deformation in the middle of capillary region than around the inlet end and around the outlet end, and the largest value of relative volumetric deformation from trough to peak reaches about 0.7% when $k_1 = 8 \times 10^{-6}\mathrm{cm\,s^{-1}}$, and reaches about 0.8% when $k_1 = 8 \times 10^{-7}\mathrm{cm\,s^{-1}}$. The greatest deformation appears in the tissue where surrounds the middle of capillary and is furthest from capillary.

2.5.2 The numerical results for seepage

Pore pressure under capillary fluctuation

Seepage could be affected by solid deformation which is caused by capillary fluctuation, and the distributions of pore pressure under the impact of volumetric deformation of microcirculatory structure are shown in Fig.2.4, which examples the change of pore pressure from trough to peak in half a second corresponding to the volumetric deformation presented in Fig.2.3a,c. These results indicate that with the increased pressure of capillary resulting from capillary fluctuation, capillary and tissues would be deformed

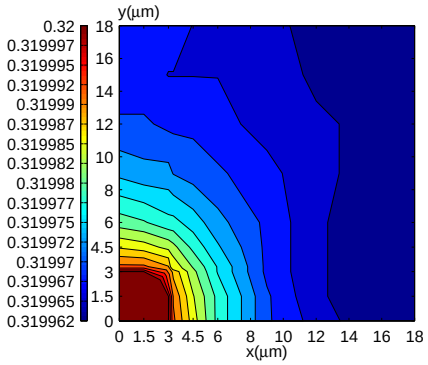

(a) t=67.75s

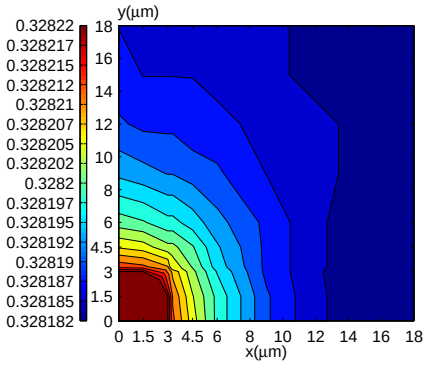

(b) t=67.8125s

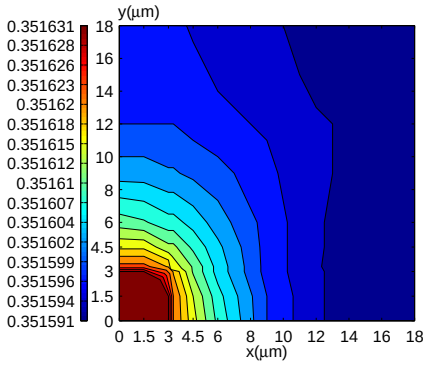

(c) t=67.875s

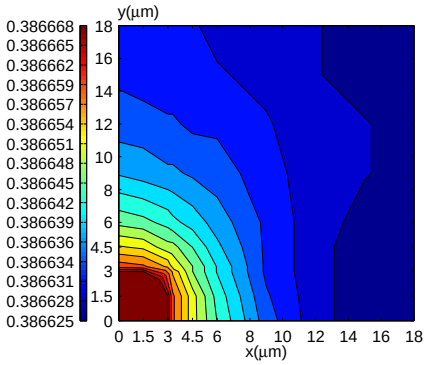

(d) t=67.9375s

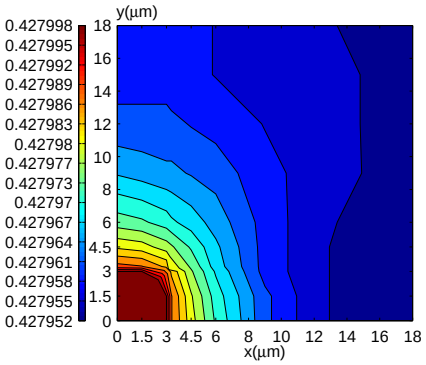

(e) t=68s

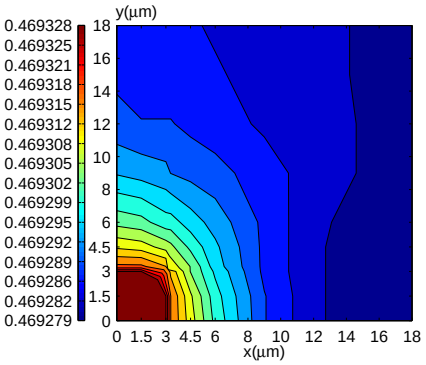

(f) t=68.0625s

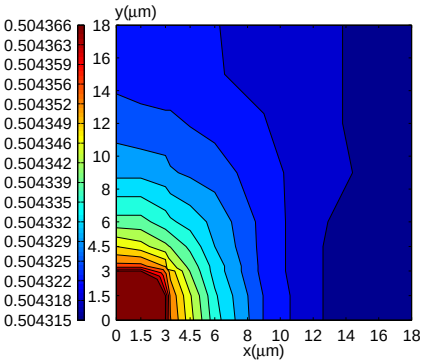

(g) t=68.125s

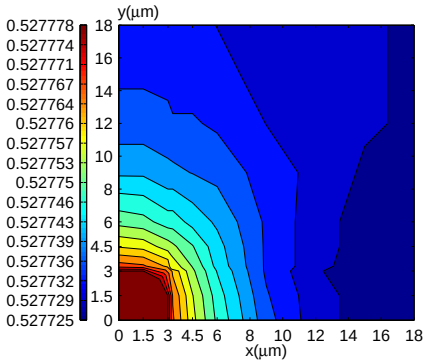

(h) t=68.1875s

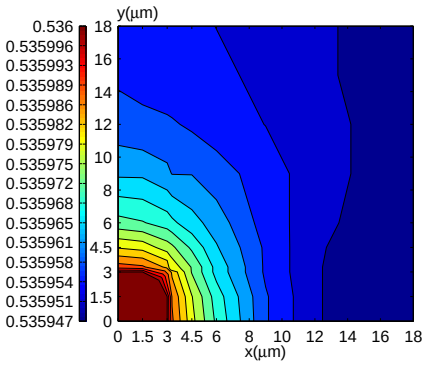

(i) t=68.25s

Figure 2.4: An example of the distribution of pore pressure from trough to peak in half a second at z=350μm when $k_1 = 8 \times 10^{-6}\mathrm{cm\,s^{-1}}$. The time points corresponds to the period from t_1 to t_2 in Fig.2.3a, respectively at (a) t=67.75s (b) t=67.8125s (c) t=67.875s (d) t=67.9375s (e)t=68s (f) t=68.0625s (g) t=68.125s (h) t=68.1875s (i) t=68.25s.

that causes pore pressure to increase.

Pressure distribution corresponding to three extreme values of capillary fluctuation

According to the experiments data on three forms of the capillary fluctuation within a given capillary (details in Sect. 2.3.4), they correspond to three extreme values for the pressure variations in the arteriole end: $p_{inlet} = 0.39\mathrm{N/cm^2}$ basically, $p_{inlet} = 0.546\mathrm{N/cm^2}$ under the combined fluctuations of Type I and II, $p_{inlet} = 0.611\mathrm{N/cm^2}$ under the combined fluctuation of Type I, II and III. Corresponding to the three values of p_{inlet} in Fig.2.5under the same condition of $k_t = 8 \times 10^{-6}\mathrm{cm\,s^{-1}}$, $k_w = 2 \times 10^{-6}\mathrm{cm\,s^{-1}}$ and $D_t = 2 \times 10^{-6}\mathrm{cm^2\,s^{-1}}$, $D_w = 10^{-6}\mathrm{cm^2\,s^{-1}}$. Comparing these results, the same pore pressure behavior can be observed:

- the pressure gradient decrease along the direction of blood flow;
- within the tissue surrounding the middle capillary, the pore pressure decreases in the direction from the capillary to the tissue;
- the pressure varies little across the same x-y slice of the middle capillary.

Seepage velocity distribution

The seepage velocity distribution at t=133.0625s, $p_{inlet} = 0.39\mathrm{N/cm^2}$ is shown in Fig.2.6, 2.7. Fig.2.6 shows the seepage velocity distribution across various x-y slices, which also indicate that counter-current flow occurs near the arteriole end and venule end of capillary. It's in agreement with the findings from pore pressure distribution. The seepage velocity distribution in various y-z slices is shown in Fig.2.7. The velocity of tissue fluid in the middle of capillary changes little with the direction of blood flow. The velocity is lower in tissue farther from the capillary.

Counter-current flow phenomenon

The results of pore pressure show the flow of blood and fluid in tissue, and indicate that some fluid seepage from the capillary vessel into the peripheral tissues on the arteriole end (Fig.2.5a). There is a partial return into the capillary vessel from the tissue near the arteriole end (Fig.2.6b). In the middle of the capillary, fluid seeps from the capillary vessel to the body tissue (Fig.2.5c,d); thus, near the venule end of the capillary, a small amount of fluid returns into the capillary vessel (Fig.2.5e, Fig.2.6e). At the

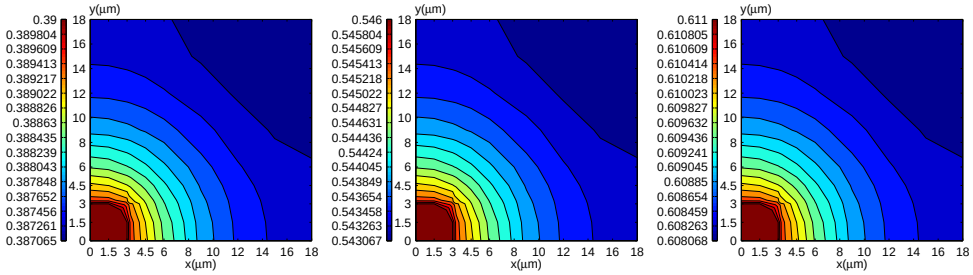

(a) z=0μm

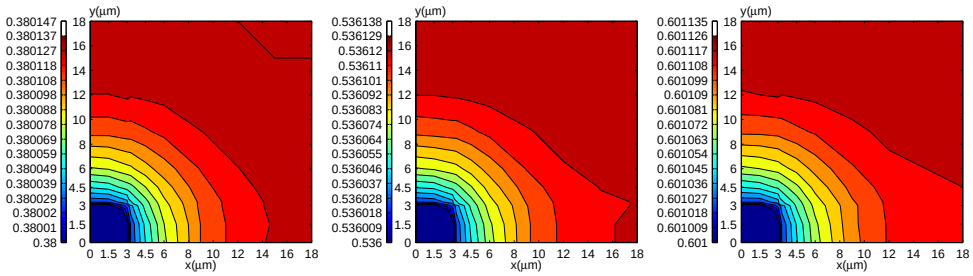

(b) z=50μm

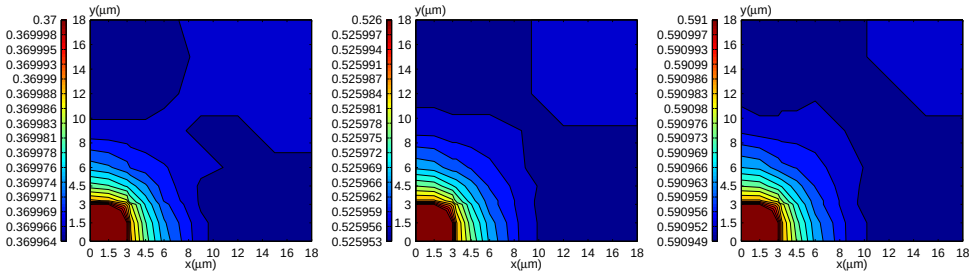

(c) z=100μm

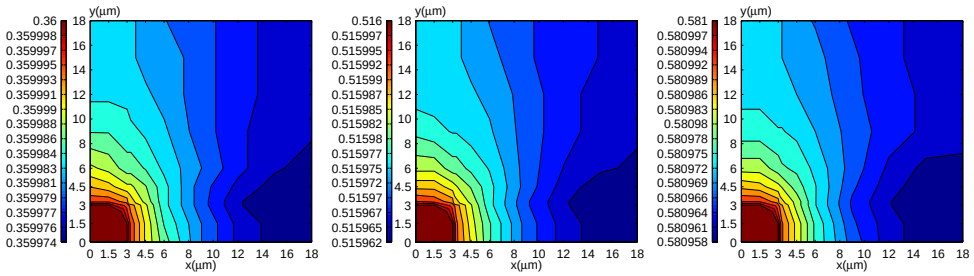

(d) z=150μm

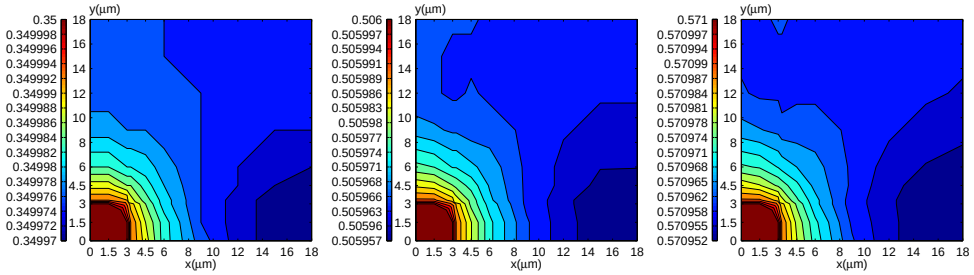

(e) z=200μm

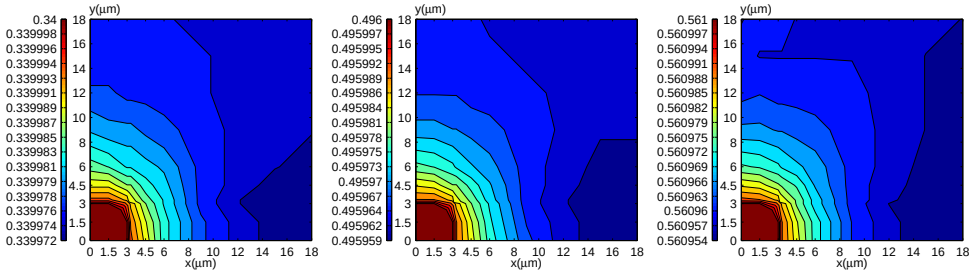

(f) z=250μm

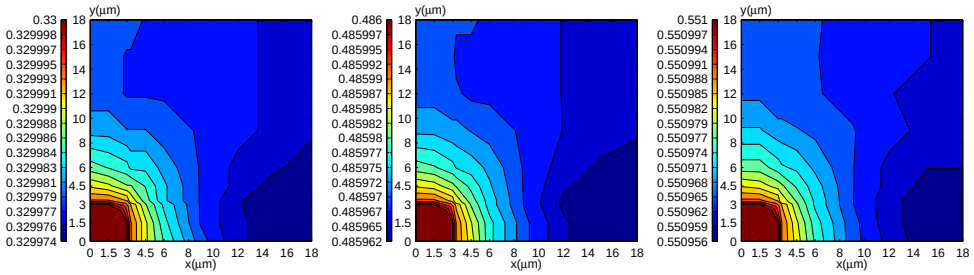

(g) z=300μm

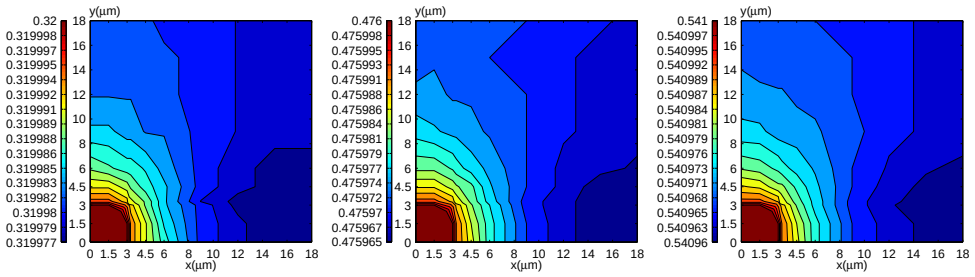

(h) z=350μm

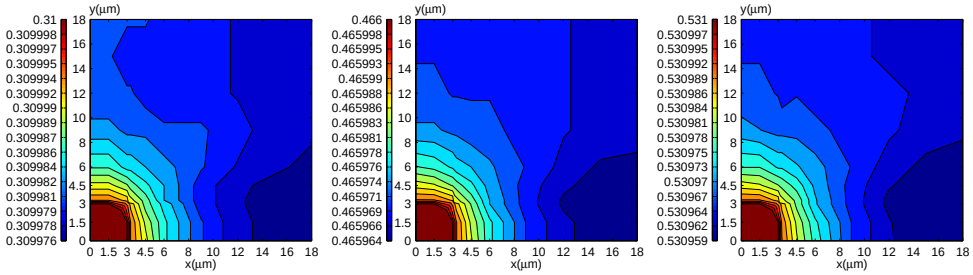

(i) z=400μm

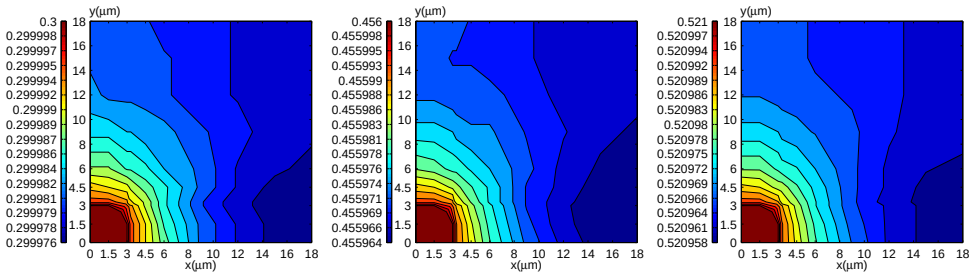

(j) z=450μm

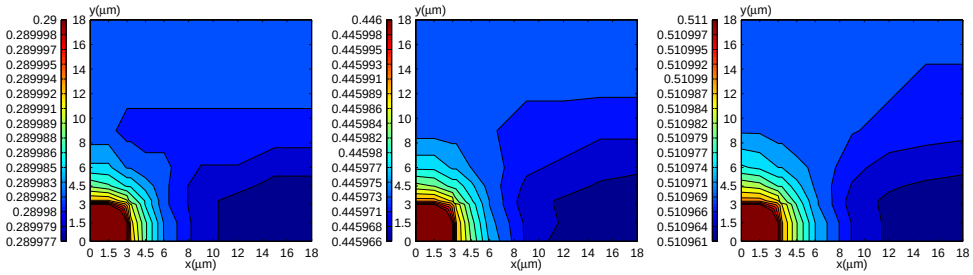

(k) z=500μm

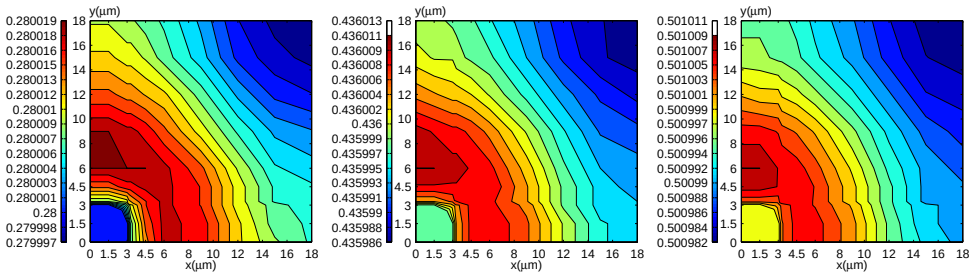

(l) z=550μm

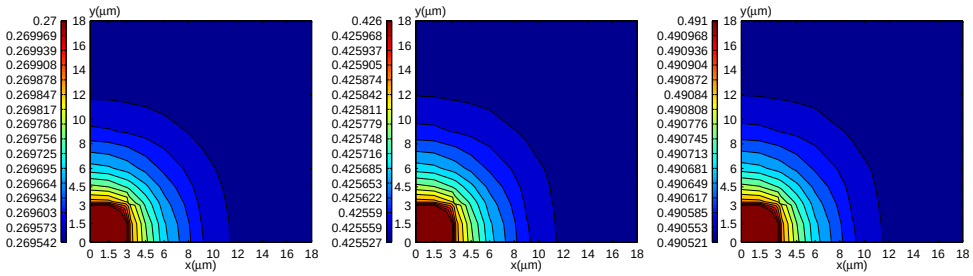

(m) z=600μm

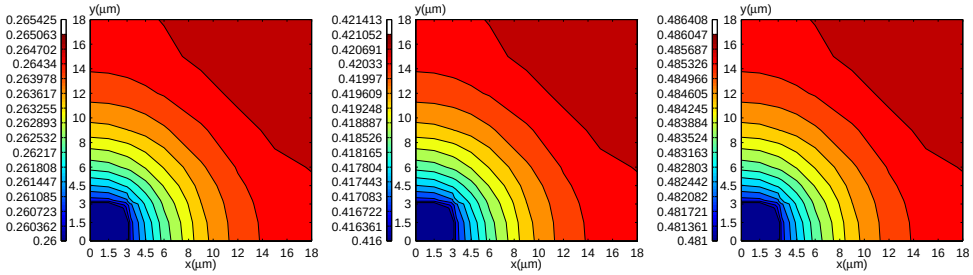

(n) z=630μm

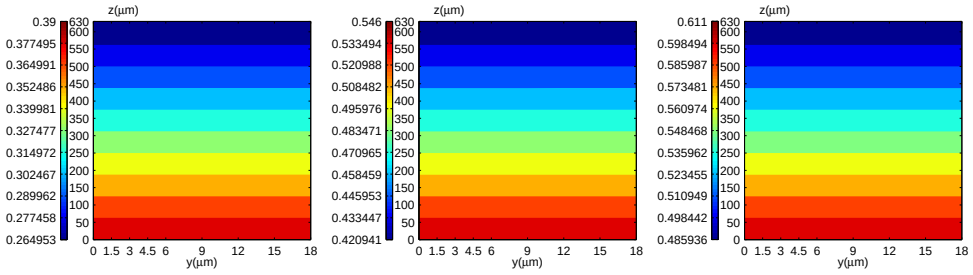

(o) along the direction of blood flow

Figure 2.5: Comparison of the distribution of pore pressure in: (a-n) x-y slices and (o) along the direction of blood flow. Pore pressure at the inlet end is 0.39 (left column), 0.546 (middle column), and 0.611 $\mathrm{N/cm^2}$ (right column). The x-y slices are located at (a) z = 0 μm (b) z = 50 μm (c) z = 100 μm (d) z = 150 μm (e) z = 200 μm (f) z = 250 μm (g) z = 300 μm (h) z = 350 μm (i) z = 400 μm (j) z = 450 μm (k) z = 500 μm (l) z = 550 μm (m) z = 600 μm (n) z = 630 μm (o) x = 0 μm. Permeability coefficient $k_1 = 8 \times 10^{-6} \mathrm{cm\,s^{-1}}$.

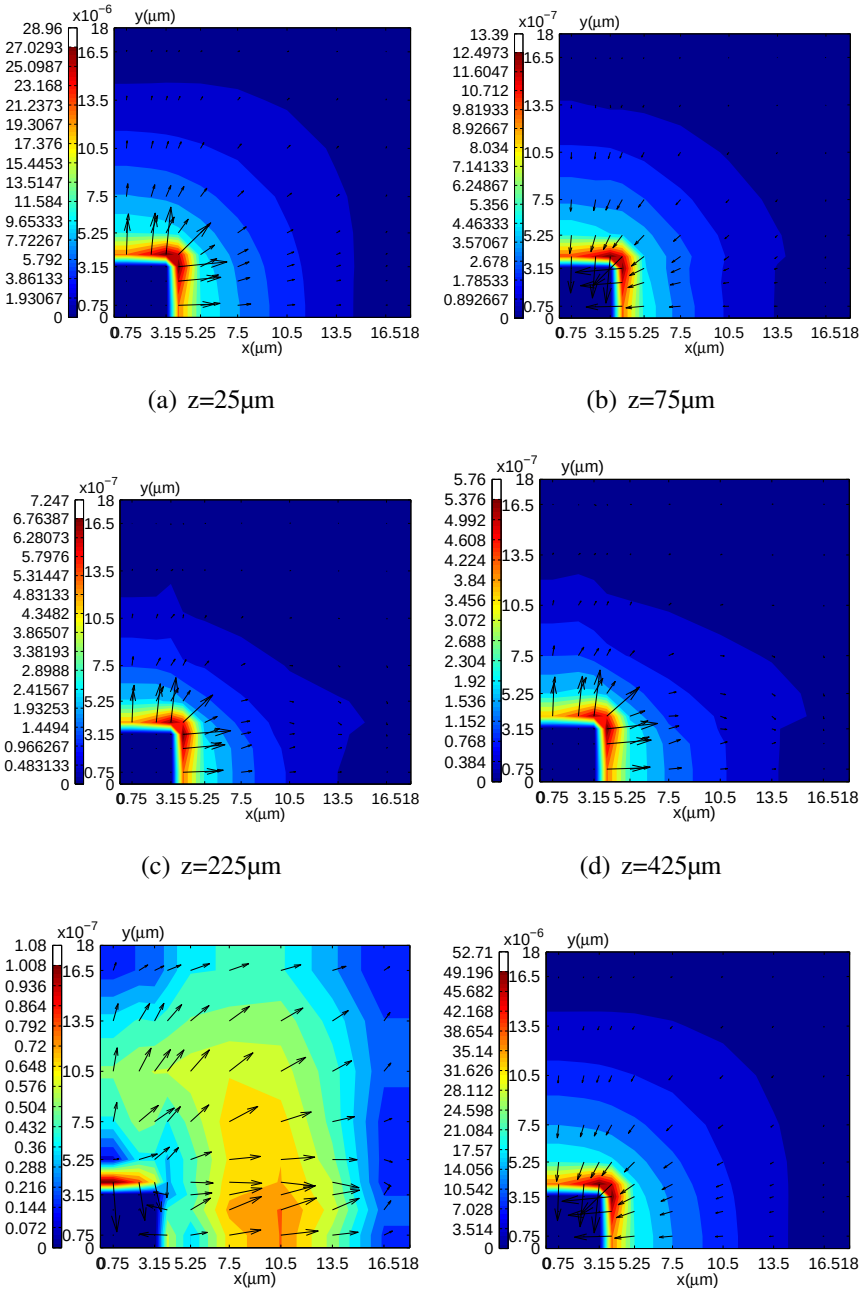

(a) z=25μm (b) z=75μm

(c) z=225μm (d) z=425μm

(e) z=525μm (f) z=615μm

Figure 2.6: Seepage velocity distribution of fluid with unit of $\mathrm{cm\,s^{-1}}$, at $t = 133.0625s, p_{inlet} = 0.39\mathrm{N/cm^2}, k_1 = 8 \times 10^{-6}\mathrm{cm\,s^{-1}}$. The sub-figures are all located in x-y slice and respectively at (a) z=25μm (b) z=75μm (c) z=225μm (d) z=425μm (e)z=525μm (f) z=615μm. Color scale shows the magnitude of V_i on x-y plane and the arrows indicate the seepage direction.

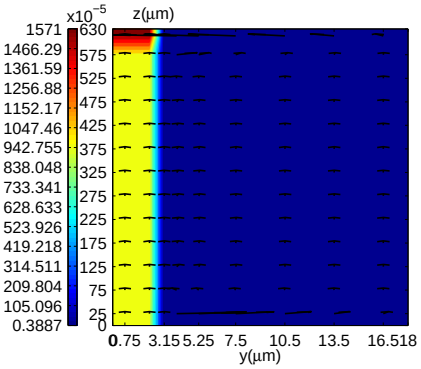

(a) x=0.75µm

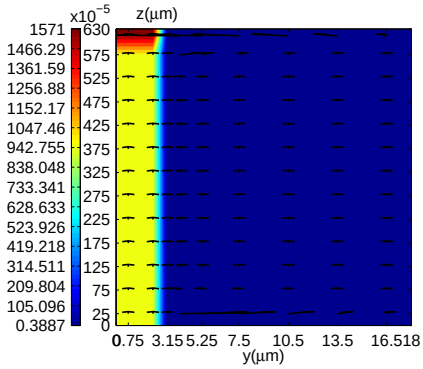

(b) x=2.25µm

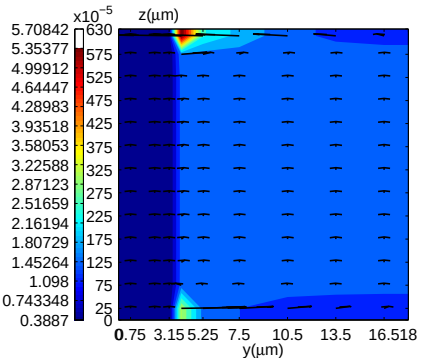

(c) x=3.15µm

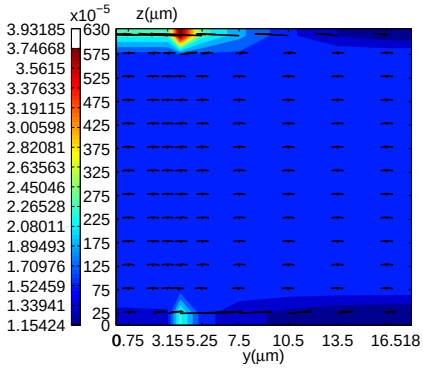

(d) x=3.90µm

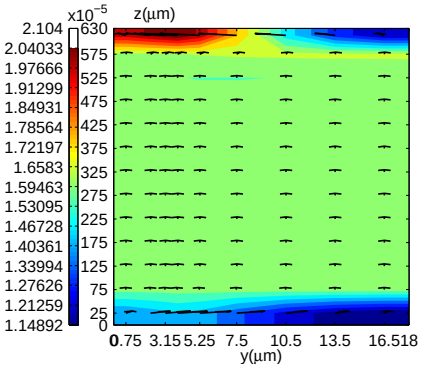

(e) x=5.25µm

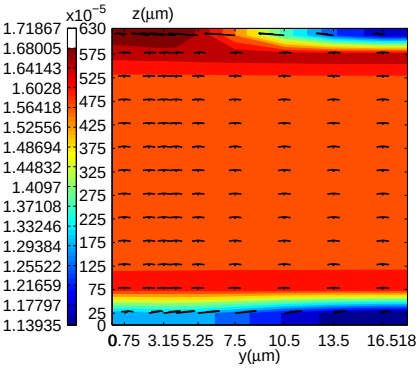

(f) x=7.50µm

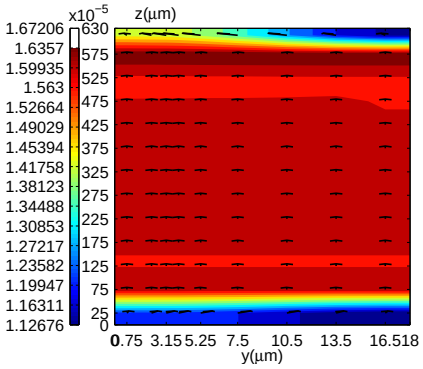

(g) x=10.50µm

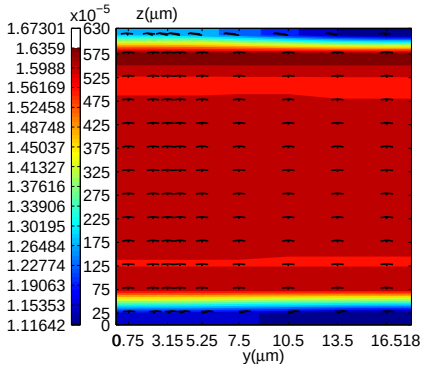

(h) x=13.50µm

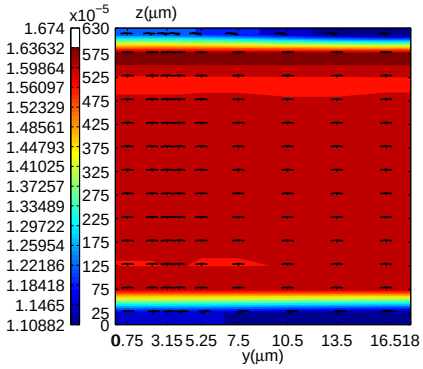

(i) x=16.50µm

Figure 2.7: Seepage velocity of fluid along the direction of blood flow with unit of $\mathrm{cm\,s^{-1}}$, at t=133.0625s, $p_{inlet} = 0.39\mathrm{N/cm^2}, k_1 = 8\times10^{-6}\mathrm{cm\,s^{-1}}$. The sub-figures are all located in y-z slice and respectively at (a) x=0.75µm (b) x=2.25µm (c) x=3.15µm (d) x=3.90µm (e) x=5.25µm (f) x=7.50µm, (g) x=10.50µm, (h) x=13.50µm, (i) x=16.50µm. Color scale shows the magnitude of V_i on y-z plane and the arrows only show the velocity direction.

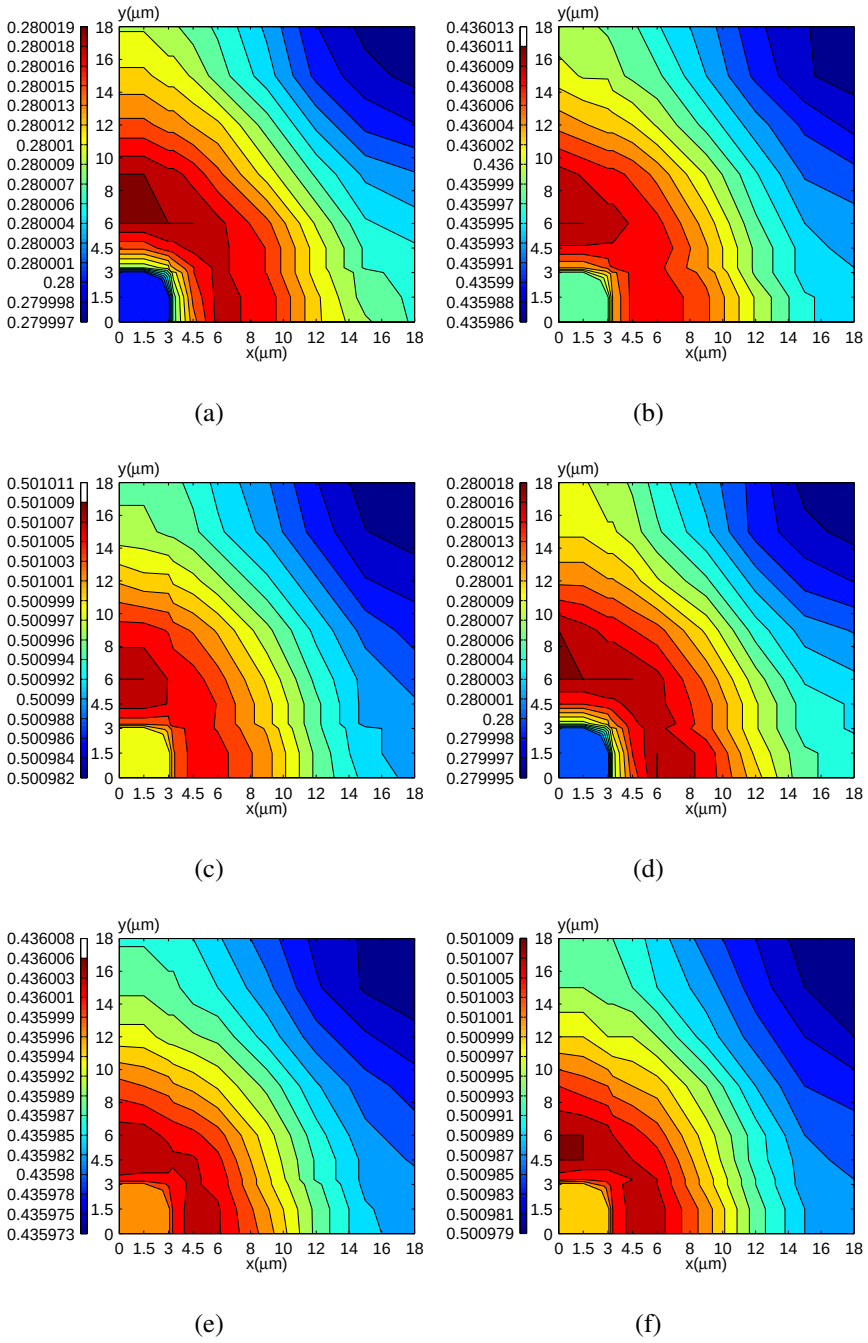

Figure 2.8: Comparison of pressure distribution with different permeability coefficient in a x-y slice at z=550μm (near the outlet of the capillary) when $D_2 = 2 \times 10^{-6}\mathrm{cm}^2\,\mathrm{s}^{-1}$ and (a-c) $k_1 = 8 \times 10^{-6}\mathrm{cm\,s}^{-1}$ (d-f) $k = 8 \times 10^{-8}\mathrm{cm\,s}^{-1}$, (a),(d) under $p_{inlet} = 0.39\mathrm{N/cm}^2$ (b),(e) $p_{inlet} = 0.546\mathrm{N/cm}^2$ (c),(f) $p_{inlet} = 0.611\mathrm{N/cm}^2$, respectively. The unit of pore pressure is $\mathrm{N/cm}^2$

venule end of capillary, fluid is finally drawn from the tissue into the capillary vessel (Fig.2.5f). These results indicate that the counter-current flow (from tissue to capillary) located occurs near the arteriole end and the venule end of capillary.

This particular phenomenon reflects an unique feature of the fluid field in the microcirculation, because this counter-current flow allows oxygen to be transported to each cell uniformly. That is, when the arterial blood reaches single capillaries, the oxygen concentration in the blood is much higher than in the peripheral tissues. This causes a tremendous concentration difference between the capillaries and the tissue, oxygen therefore diffuses rapidly from the capillary blood into its surrounding tissue, where excess oxygen would partly be stocked. Thus, to supply adequate oxygen to cells that are further away from the arteriole end, the oxygen near the arteriole end must partly return to the capillary vessel from the tissue to be carried to other regions through the blood. This is a more efficient method of supplementing and consuming oxygen for all body cells. The sudden change in pore pressure gradient allows the oxygen to partly return into the capillary by convection-diffusion. Similarly, because the oxygen in the blood continues to be carried to the tissues, oxygen within the capillary becomes depleted near the venule end, meaning that the oxygen concentration within the tissue near the venule end becomes relatively higher. To reach cells that are farther from the arteriole end, the oxygen has to partly return to the capillary near the venule end. A certain percentage of oxygen in the blood must be carried into the venule (P_{O_2} = 40 mmHg at the venule end). At the venule end of the capillary, deoxygenated blood is carried from the tissues back to the heart. If physiologically some non-homogenous materials could be produced surrounding the arteriole end that leads the permeability in arteriole end to be less, the counter-current flow might not appear. But if only basing on the heterogeneity of capillaries and tissue, this counter-current flow would appear. The results also may provide some explanation for why more fluid is often found remaining in the tumor tissue. For example, high permeability coefficient together with a high tissue boundary pressure may lead to the counter-current flow, which in turn causes more fluid to be stocked within the tissue, and thus oxygen transport is affected.

The effect of different permeability coefficients on the counter-current flow is examined in Fig.2.8, this indicates that counter-current flow becomes more obvious with the increasing permeability coefficient, which agrees with the study (He and Himeno 2012). He'work shows that the interstitial fluid will be reabsorbed into the capillary and that counter-current flow occurs counter-current flow occurs near the outlet end if the seepage is sufficiently strong.

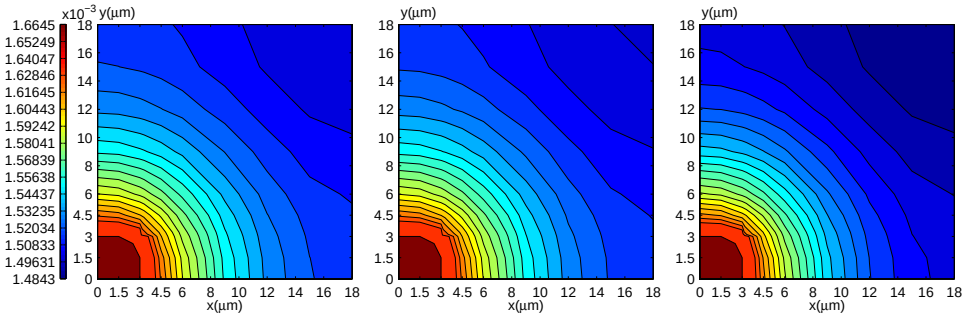

(a) z=0μm

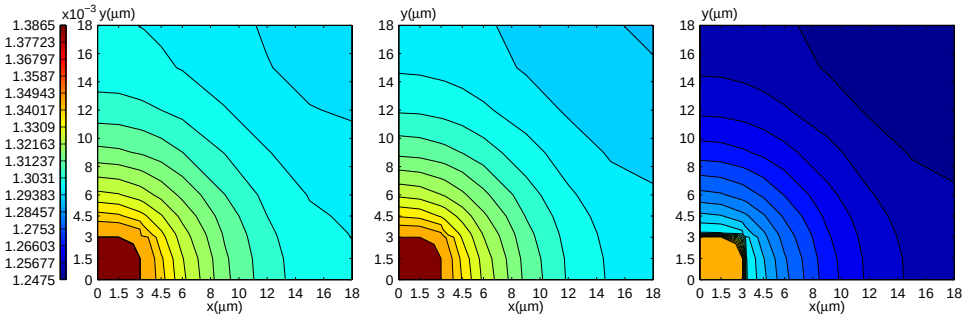

(b) z=50μm

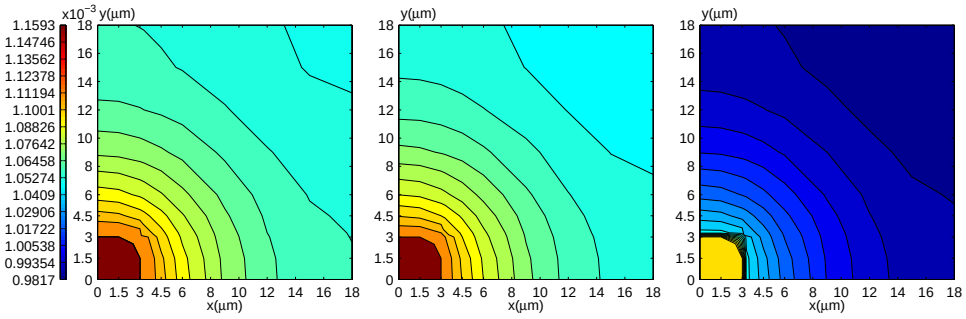

(c) z=100μm

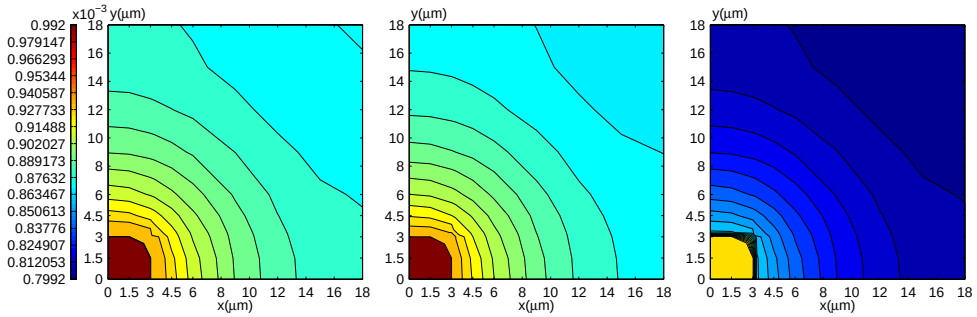

(d) z=150μm

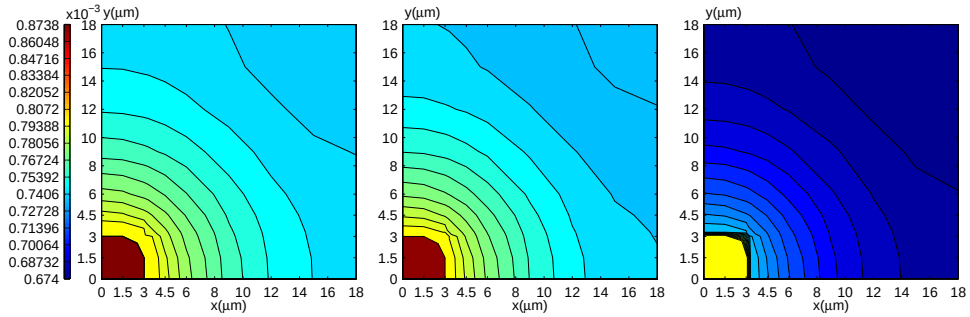

(e) z=200μm

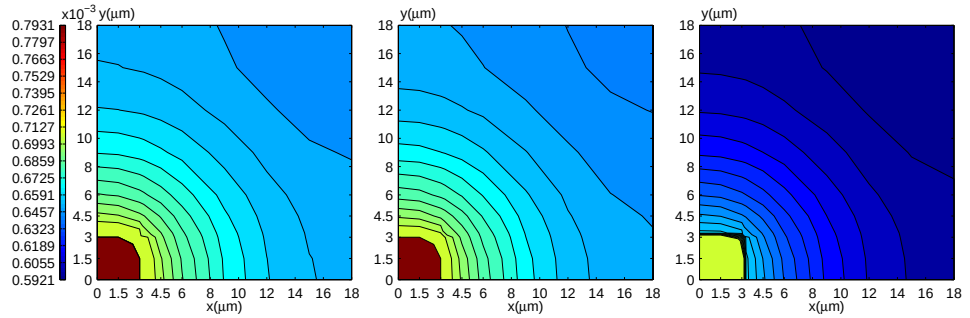

(f) z=250μm

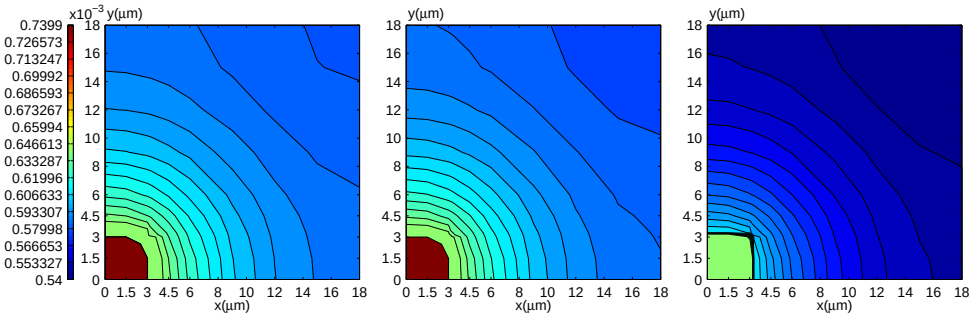

(g) z=300μm

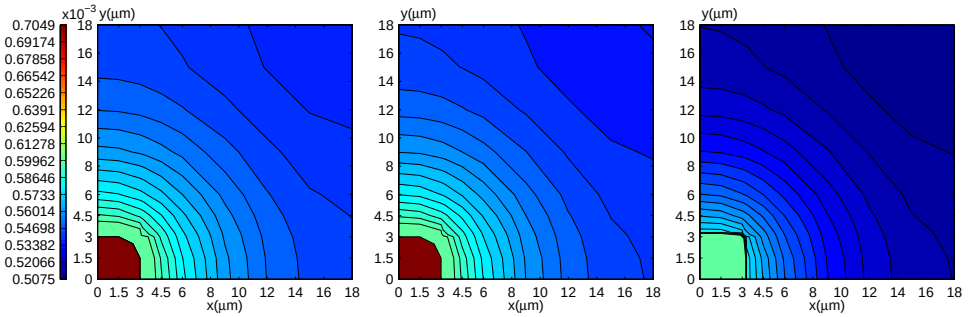

(h) z=350μm

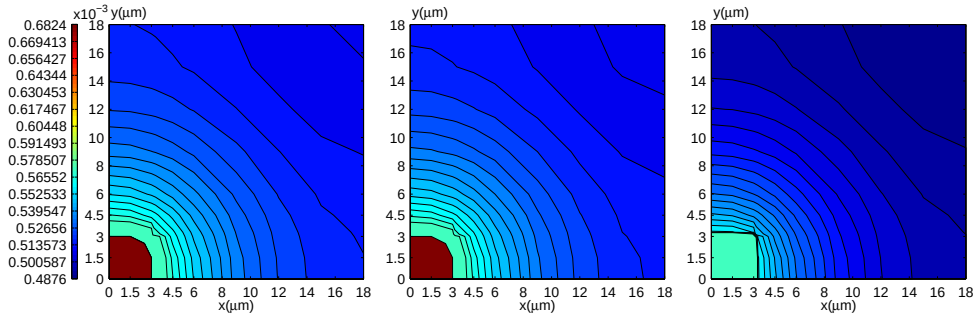

(i) z=400μm

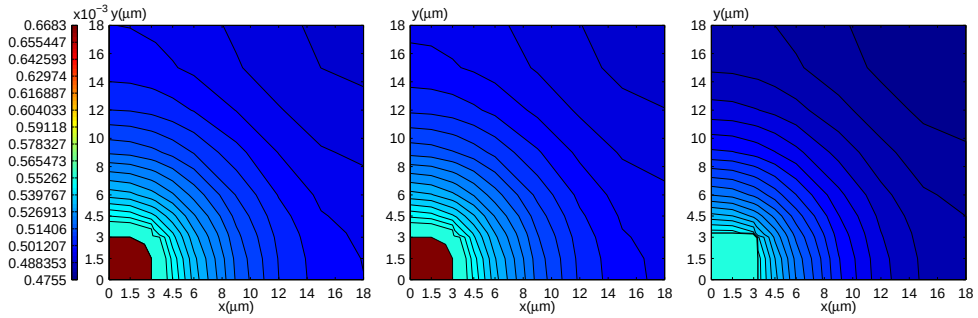

(j) z=450μm

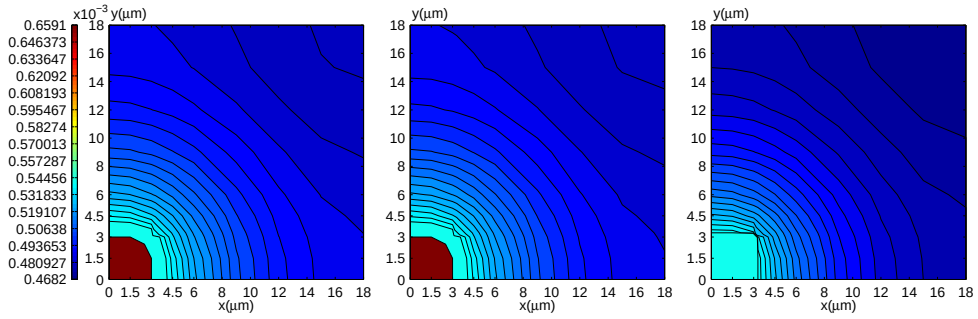

(k) z=500μm

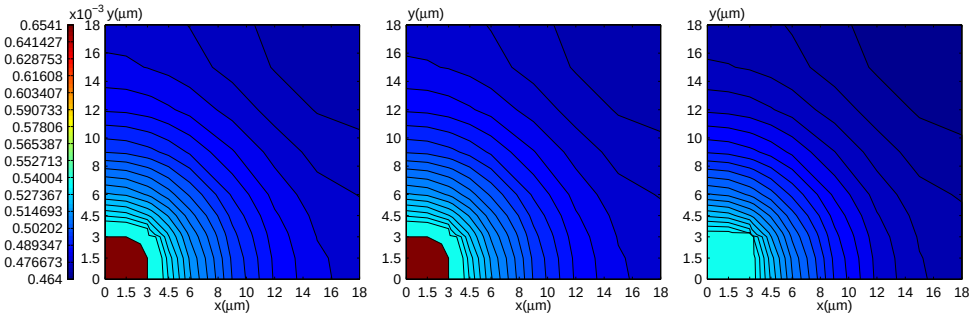

(l) z=550μm

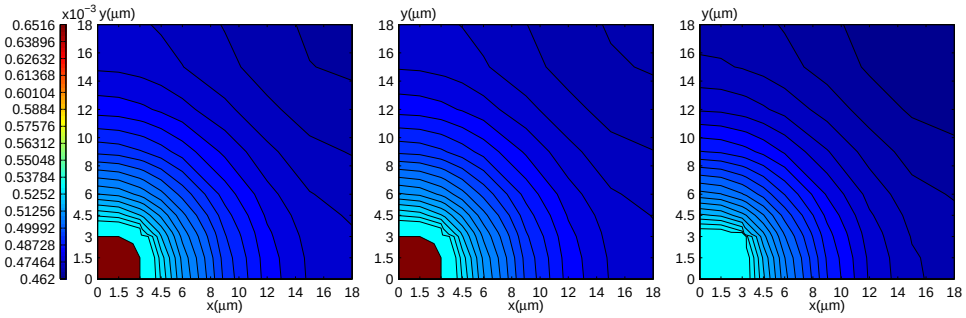

(m) z=600μm

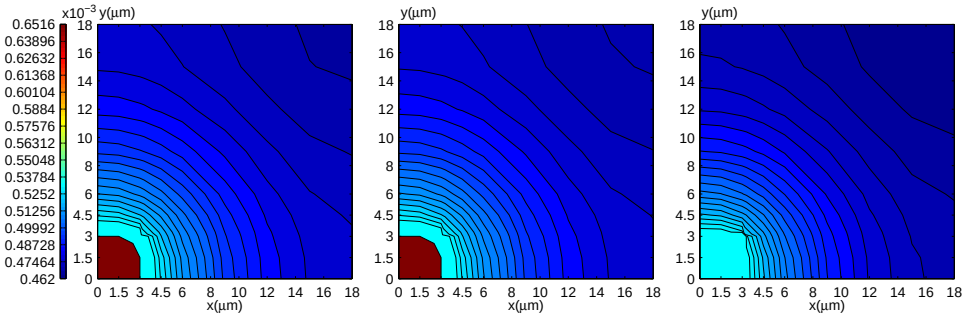

(n) z=630μm

Figure 2.9: A comparison of oxygen concentration distribution along the direction of blood flow given by the coupled solid deformation, fluid seepage, convection-diffusion and molecular diffusion model i.e. this present model (left column), by the coupled fluid seepage, convection-diffusion and molecular diffusion model, i.e. no coupling solid deformation (middle column), and by a pure molecular diffusion model, i.e. no coupling convection (right column). The three models use the same parameters: diffusion coefficient $D_1 = 2 \times 10^{-6}\mathrm{cm}^2\,\mathrm{s}^{-1}$ and the permeability coefficient $k_1 = 8 \times 10^{-6}\mathrm{cm}\,\mathrm{s}^{-1}$ used in the coupled model. The x-y slices are located at (a) z = 0 μm (b) z = 50 μm (c) z = 100 μm (d) z = 150 μm (e) z = 200 μm (f) z = 250 μm (g) z = 300 μm (h) z = 350 μm (i) z = 400 μm (j) z = 450 μm (k) z = 500 μm (l) z = 550 μm (m) z = 600 μm (n) z = 630 μm. The unit of oxygen concentration is $\mathrm{ml}\,\mathrm{ml}^{-1}$.

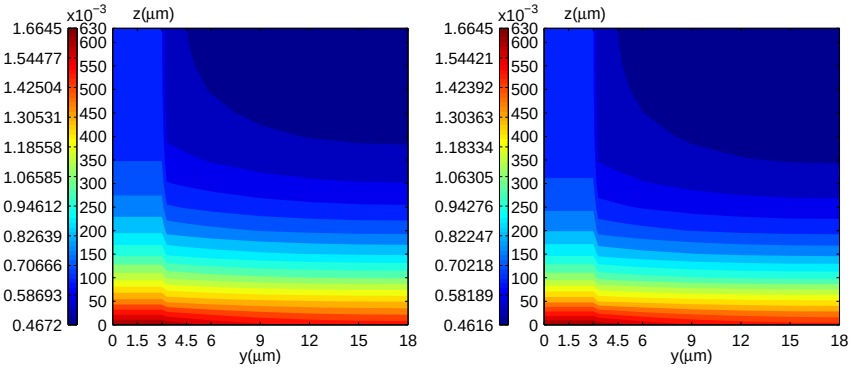

(a) x=0μm

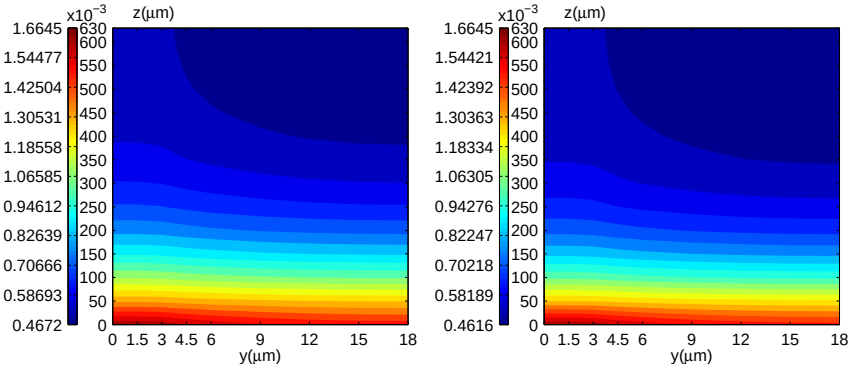

(b) x=3.3μm

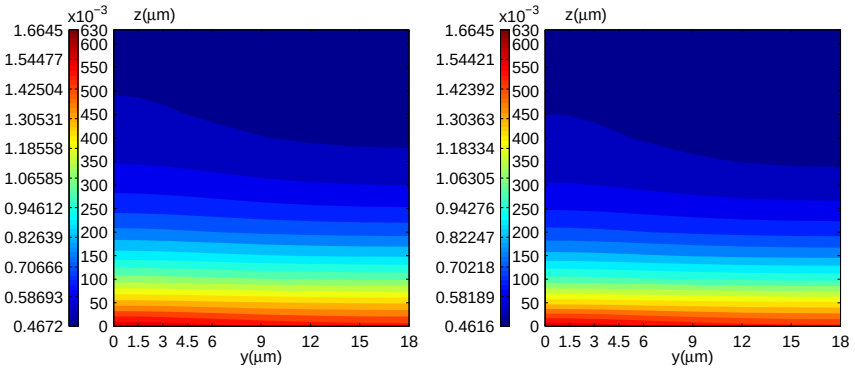

(c) x=6μm

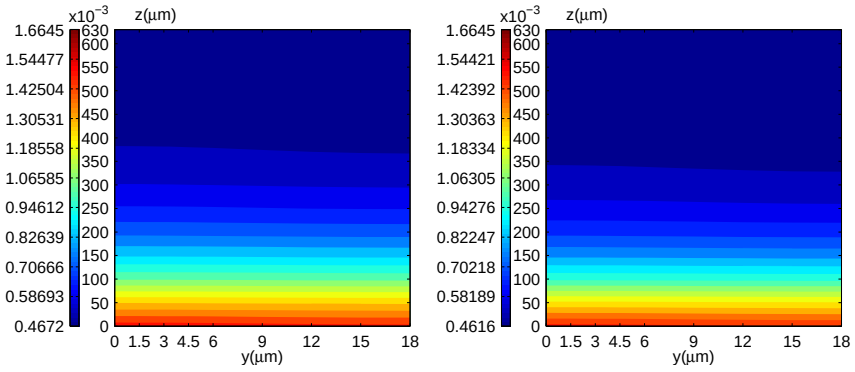

(d) x=18μm

Figure 2.10: The comparison of oxygen concentration distribution in the direction of blood flow between using the model coupled convection-diffusion and molecular diffusion (left side), and using the model only considered molecular diffusion (right side). Using same diffusion coefficient $D_1 = 2 \times 10^{-6}\text{cm}^2\,\text{s}^{-1}$ and the permeability coefficient $k_1 = 8 \times 10^{-6}\text{cm}\,\text{s}^{-1}$ in the coupled model. The y-z slices located at (a)x=0μm (b)x=3.3μm (c)x=6μm (d)x=18μm. The unit of oxygen concentration is $\text{ml}\,\text{ml}^{-1}$.

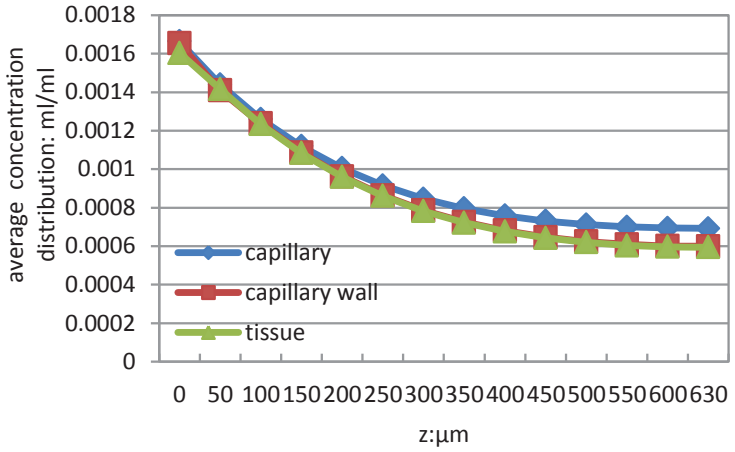

Figure 2.11: Change in mean oxygen concentration in the direction of blood flow at $D_1 = 2 \times 10^{-6}\text{cm}^2\,\text{s}^{-1}, k_1 = 8 \times 10^{-6}\text{cm}\,\text{s}^{-1}$ in three sub-domains: within the capillary, at the capillary wall, and in the surrounding tissue. Oxygen concentration given in units of ml/ml.

2.5.3 The numerical results for oxygen concentration

Oxygen concentration given by coupled convection and diffusion model

To examine how convection–diffusion impacts on oxygen transport, the oxygen concentration distributions given by the coupled model of convection–diffusion and molecular diffusion, given by the model not coupling solid deformation, and given by a model that only takes account of molecular diffusion are shown in Figs. 2.9.

Obviously, the tissue oxygen concentration changes little in the middle of the capillary vessel. Fig. 2.10 shows the change in oxygen concentration (dissolved in plasma) from arteriole end to venule end and in the surrounding tissue. The oxygen concentration reduces rapidly at the front of the capillary vessel, but reduces very slowly from around z = 200 μm. This agrees with the physiological condition whereby, when arterial blood reaches the capillary bed, oxygen in plasma is immediately transported to the tissue, and then evenly supplied to all individual cells. This is accomplished in the middle of the capillary vessel. The change in mean C_{O_2} along the direction of blood flow in the three sub-domains of intra-capillary, capillary wall, and surrounding tissue is shown in Fig. 2.11. This indicates that C_{O_2} is highest at the arteriole end of the capillary, and reduces along the direction of blood flow. It changes slowly in the latter part of the capillary, and eventually reaches a minimum value at the venule end.

2.6 Discussion

2.6.1 Effect of convection-diffusion on oxygen transport

To study how convection-diffusion impacts on oxygen transport, comparing with the oxygen concentration given by the coupled convection-diffusion and molecular diffusion model, the third column of Fig.2.9 and the second column of Fig.2.10 give the distribution of oxygen concentration given by the pure molecular diffusion model, respectively in x-y slices and in y-z slices. The same parameters are used for their comparison in Fig.2.9,2.10. We denote the oxygen concentration obtained from the coupled model of convection-diffusion and molecular diffusion as $C_{coupled}$ and that obtained from the pure molecular diffusion model as C_{diff}. The relative difference in oxygen concentration between the two models can be calculated by Eq.(2.17). This gives the relative effect of convection-diffusion to molecular diffusion.

$$r = \frac{\left(C_{coupled} - C_{diff}\right)}{C_{diff}}. \tag{2.17}$$

The curves of this relative difference along the direction of capillary in Fig.2.12. They show that convection-diffusion has an impact in the capillary vessel and also in the tissue, and has a greater effect in the middle of the capillary than near the inlet end and the outlet end of capillary. This is well in agreement with the findings from Yao'model (Yao and Gu 2007). We can see that larger values of the permeability coefficient produce a more obvious convection–diffusion effect, as do smaller values of the diffusion coefficient. The maximum of the relative difference is approximately 16%; the influence of convection–diffusion cannot be ignored in either the capillary or the tissue.

2.6.2 Effect of solid deformation on oxygen transport

Though some theoretical models considered the deformable porous media in the numerical simulation for microcirculation (Yao and Gu 2007;Byrne and Preziosi 2003), they failed to model the deformation of circulatory structure according to the physiological power source of the capillary fluctuation. For example, in Yao'work, the solute flux and convective flux in a porous medium were investigated using a mechano-electrochemical mixture theory and the dynamic unconfined compression test configuration for solute desorption experiments was carried on to simulate the solid deformation in a porous medium. Thus, basing on the experimental data of the pressure variations for capillary fluctuation, we couple the solid deformation with the fluid seepage

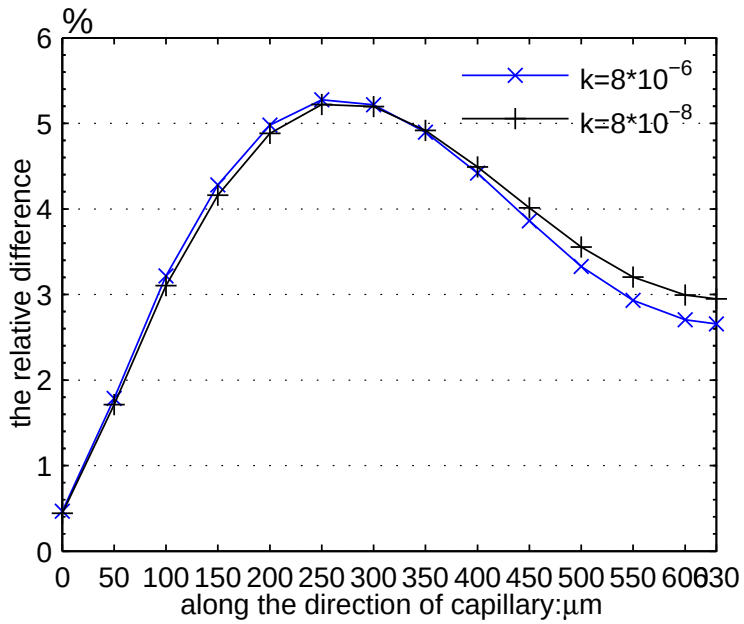

(a) $\left(C_{coupled} - C_{diff}\right)/C_{diff}, D_1 = 2 \times 10^{-5}$

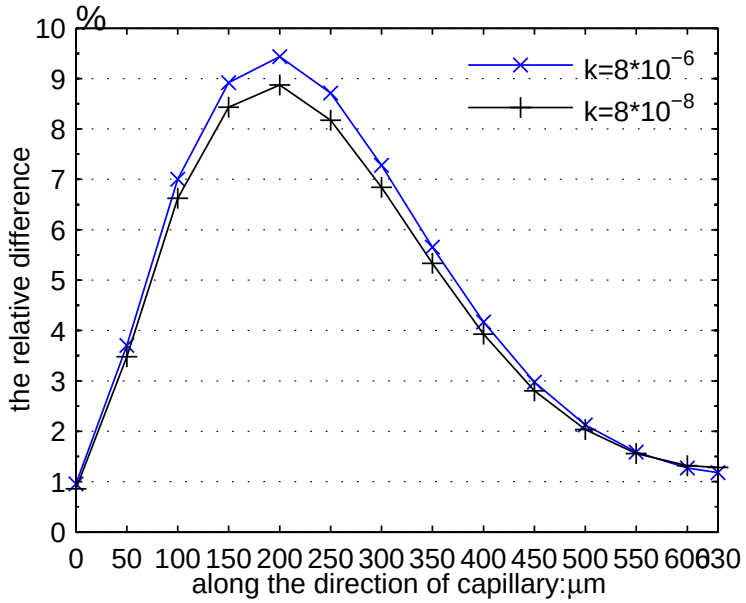

(b) $\left(C_{coupled} - C_{diff}\right)/C_{diff}, D_1 = 2 \times 10^{-6}$

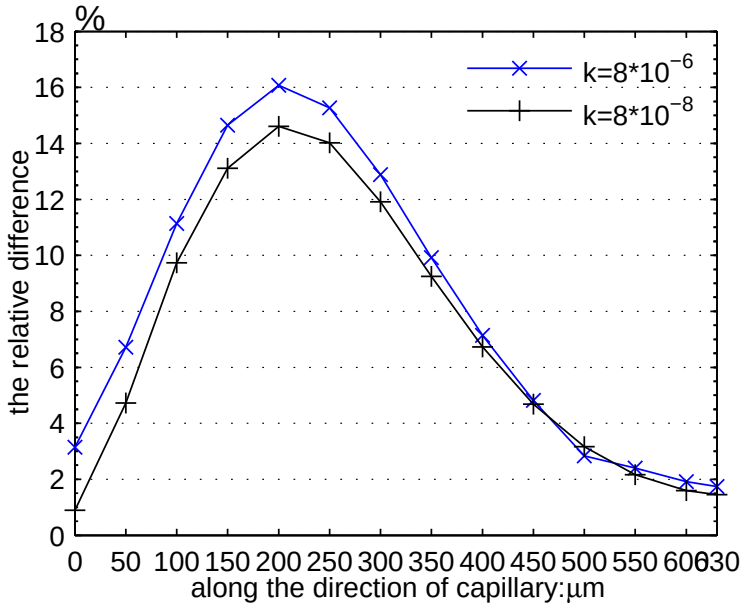

(c) $\left(C_{coupled} - C_{diff}\right)/C_{diff}, D_1 = 2 \times 10^{-7}$

Figure 2.12: Comparison of the relative effect of convection-diffusion for different values of permeability coefficient and diffusion coefficient. Vertical axis shows the relative difference of oxygen concentration, calculated by Eq.(2.17), this corresponds to the horizontal axis. The horizontal axis indicates z axis along the direction of capillary, respectively z=0, 50, 100, 150, 200, 250, 300, 350, 400, 450, 500, 550, 600, 630μm. Relative difference of convection-diffusion to molecular diffusion on oxygen transport in cases of (a) $D_1 = 2 \times 10^{-5}$ (b) $D_1 = 2 \times 10^{-6}$ (c) $D_1 = 2 \times 10^{-7}$ with the unit of $\mathrm{cm^2\,s^{-1}}$. Pink denotes $k_1 = 8 \times 10^{-8}$ and blue denotes $k_1 = 8 \times 10^{-6}$ with the unit of $\mathrm{cm\,s^{-1}}$.

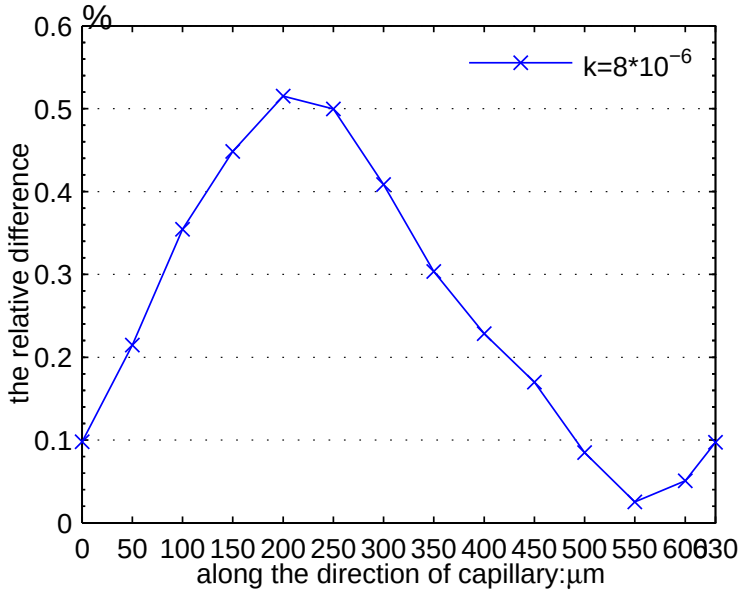

Figure 2.13: Comparison of the relative difference in oxygen distribution given by this present coupled model and by the model with no solid deformation, when $k_1 = 8 \times 10^{-6}\mathrm{cm\,s^{-1}}, D_1 = 2 \times 10^{-6}\mathrm{cm^2\,s^{-1}}$. Vertical axis shows the relative difference of oxygen concentration of each line at y direction in the x-y slices, calculated by $\left(C_{coupled} - C_{nodefor}\right)/C_{nodefor}$, this corresponds to the horizontal axis, same as Fig.2.12.

which has not been found in other models. How solid deformation affect oxygen transport can be examined by comparing the oxygen concentration given by the coupled fluid solid seepage and deformation model ($C_{coupled}$) and by the pure seepage model (denote as $C_{nodefor}$). $C_{nodefor}$ in x-y slices shown in the second column of Fig.2.9 indicate that solid deformation has an impact on oxygen transport but not too much, and the effect is greater in the front of capillary than in the latter of capillary. Moreover, the relative difference between the both models, i.e. $\left(C_{coupled} - C_{nodefor}\right)/C_{nodefor}$, in the direction of blood flow is shown in Fig.2.13. From this, we can see that the relative effect of solid deformation to oxygen concentration in the direction of capillary is about 0.5% maximum and 0.3% average. From comparing the first column and the second column in Fig.2.10, it can be observed the significant impact of solid deformation in oxygen transport is that the solid deformation can help the fluid to seepage more uniformly, further can help the oxygen to be transported more uniformly.

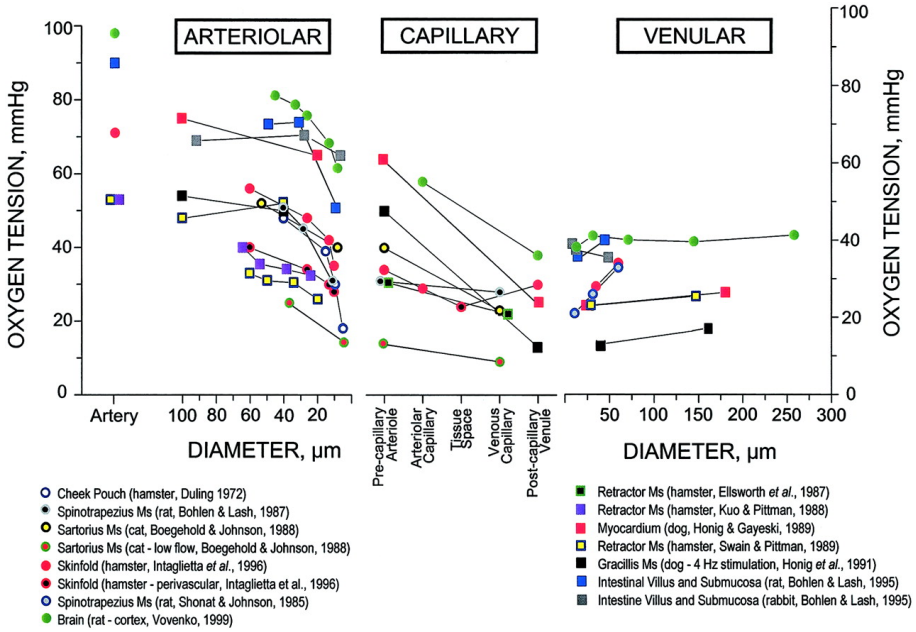

Figure 2.14: Distribution of the oxygen tension in the microcirculation found in different tissues with different techniques. Microelectrode measurements: Cheek pouch, hamster; brain cortex, rabbit; sartorius muscle, cat; spinotrapezius muscle, rat. Microspectrophotometric technique: retractor muscle, hamster; intestinal villus and submucosa, rat; intestinal villus and submucosa, rabbit. Cryoscopic technique: myocardium, dog; gracilis muscle, dog. Phosphorescence quenching: skinfold preparation, hamster; spinotrapezius muscle, rat. Squares signify that the original measurement was in terms of hemoglobin oxygen saturation (%), and circles are measurements of oxygen partial pressure (mmHg). Oxygen saturation data were converted to oxygen partial pressures using animal specific oxygen dissociation curves [dog, rabbit; rat; hamster].(Tsai et al 2003)

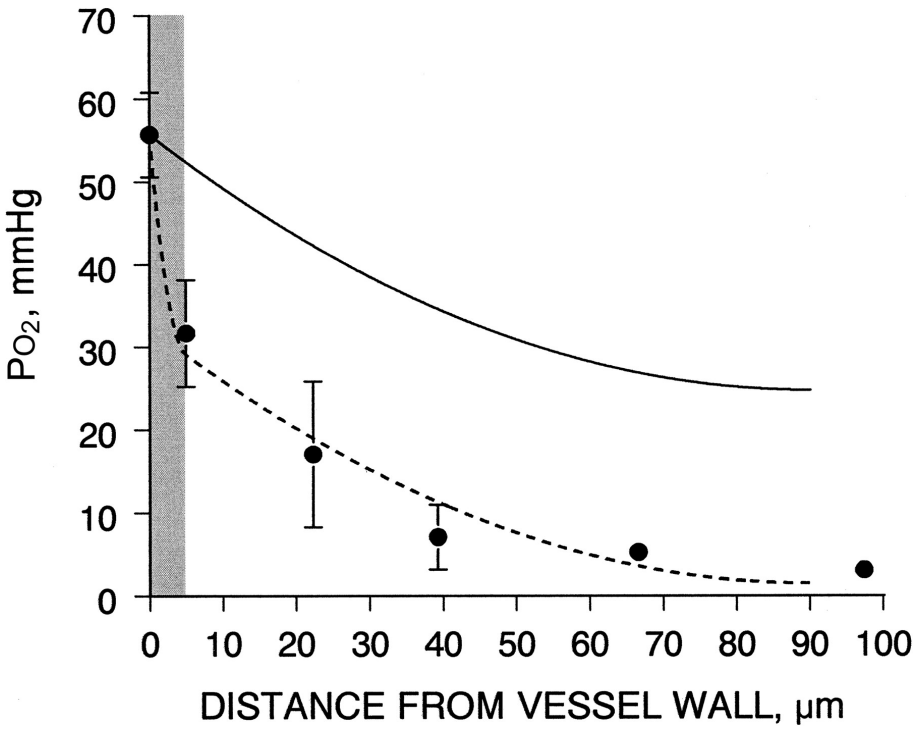

Figure 2.15: P_{O_2} profile in the immediate vicinity of the arterioles in the rat mesentery. Fitting of these data to the oxygen profile deduced by solving the diffusion equation shows that the medium beyond the blood/tissue interface must be divided into two zones with significantly different rates of oxygen consumption, where the outside of the vessel wall rate is two orders of magnitude higher than the remainder of the tissue. The shaded area represents the portion of the tissue that is occupied by the vessels wall. (Tsai et al 1998)

2.6.3 Experimental data for oxygen transport

Data on longitudinal gradients in the arteriolar network for a number of these studies (Tsai et al 2003) are shown in Fig.2.14, left. As is evident from the preceding descriptions and Fig.2.14, there are substantial differences in the longitudinal gradients in different vascular beds; the gradient is much less in the brain compared with the hamster window preparation, for example. There also appear to be differences dependent on the measurement technique employed; the gradient was reported to be much less in resting skeletal muscle with the cryoscopic method than that reported with the micro-electrode or phosphorescence techniques.

The study of Tsai et al. (Tsai et al 1998) allowed to verify the accuracy of the data and calculations by application of the law of mass conservation (also called law of mass balance) that stipulates that the amount of oxygen lost from a vascular segment must be equal to the diffusional oxygen flux, determined by the perivascular P_{O_2} gradient. These investigators measured the rate of oxygen exit both longitudinally and radially in arteriolar vessel segments of the rat mesentery. Oxygen profiles in the tissue were obtained in the tissue surrounding the arterioles, as shown in Fig.2.15. The finding of a steep fall in P_{O_2} near the vessel wall was common to all groups. The measured tissue P_{O_2} profile in the region of the vessel wall was used to calculate the rate of oxygen exit by diffusion from the vessels, and this number was compared with the longitudinal rate of decrement of oxygen content of the same vessels.

These experimental data indicate that the oxygen concentration decreases in the direction from capillary to its surrounding tissue, our simulation results of oxygen concentration are consistent with this regulation and blood oxygen concentration in capillary calculated by our mathematical model is also consistent with the data in Fig.2.14.

2.6.4 Comparison of the proposed coupled model with previous models

Because of the very low fluid velocity, many previous models of oxygen transport have neglected the effect of convection–diffusion. Some mathematical models of oxygen transport have completely neglected the convection–diffusion of oxygen within both capillaries and tissue,Macklin and Lowengrub (2007); Liu et al (2012); He and Himeno (2012); Cai et al (2011); Zhu et al (2012) whereas others have incorporated the convection–diffusion of oxygen within capillaries, but have assumed the velocity of the tissue fluid to be zero and neglected this effect within tissue.Schuff et al (2013b) Though the assumption of zero velocity for tissue fluid has been commonly used in

mathematical models, this does not take account of solid deformations resulting from capillary fluctuations—the effects of which have been demonstrated by experiments. In the present model, the solid deformation is coupled with fluid seepage into the model of oxygen transport, which has not been found in other models. Based on this combination, the seepage velocity within tissue from the coupled model is larger than that from previous models that do not account for capillary fluctuations. Thus, our results are closer to the reality than those given by the simple assumption of zero velocity.

In addition to the standard axial convection–diffusion inside the capillary vessel and molecular diffusion in the tissue, Fig. 2.12 shows the convection across the capillary wall and in the surrounding tissue. The numerical results suggest that, at this level, there is an increase of up to 16% in capillary–tissue oxygen transport due to convection across the capillary wall and in the surrounding tissue. These results also indicate that convection–diffusion has a greater effect in the middle capillary region than around the inlet and outlet of the capillary region. These results are in good agreement with those from Yao's model,Yao and Gu (2007) in which the solute flux and convective flux in a porous medium were investigated using a mechano-electrochemical mixture theory to determine the convective flux distributions within the tissue. They used a dynamic unconfined compression test configuration for solute desorption experiments to simulate solid deformation in a porous medium, but did not employ a physiological parameter to model the solid deformation.

The counter-current flow phenomenon agrees with the findings of a previous study.He and Himeno (2012) He and Himeno found the distribution of blood, interstitium pressure, and seepage velocity in the microcirculation for oxygen transport, and determined that the interstitial fluid will be reabsorbed into the capillary. They also found that counter-current flow occurs near the outlet end if the seepage is sufficiently strong. Our results agree with their findings,He and Himeno (2012) indicate that counter-current flow becomes more marked with an increasing permeability coefficient. The results may provide an explanation as to why more fluid often remains in the tumor tissue. For example, a high permeability coefficient together with a high tissue boundary pressure may lead to counter-current flow, which in turn causes more fluid to be stocked within the tissue, thus affecting oxygen transport. However, their 2D modelHe and Himeno (2012) was constructed on a plane surface that partially conserves the geometry of the micro-vessels while ignoring the 3D spatial curvature. Therefore, it cannot present the counter-flow phenomenon in 3D geometrical structures, nor the vertical velocity with respect to the direction of blood flow.

2.7 Conclusion

This present study numerically simulate an entire process of oxygen transport at the level of microcirculation by developing a 3D coupled solid deformation–fluid seepage–convection and diffusion porous media model, which newly takes account of volumetric deformation of both capillary and tissue resulting from capillary fluctuation, and couples the deformations into seepage, then the seepage coupled the deformation affects on convection-diffusion of oxygen. We quantitatively examine how solid deformation, fluid seepage and convection-diffusion affect the transport of oxygen, and have some important findings:

- Solid deformation is more significant in the middle of capillary, where the maximum value of volumetric deformation reaches about 0.5%;
- Though solid deformation has a small impact on seepage, it can help the tissue fluid to flow more uniformly, also can help the oxygen to be transported more uniformly, eventually affects on the distribution oxygen concentration by 0.1% 0.5%.
- The change in pore pressure distribution within the tissue near arteriole end and near venule end of capillary is several times larger than within the tissue surrounding the middle of capillary.
- Convection-diffusion given by coupled deformation and seepage has a 16% maximum, 3% average increase in oxygen concentration, compared to pure diffusion. Its more significant role is to allows oxygen to be transported more evenly, especially to where is away from capillary.
- Convection-diffusion has a greater effect in the middle of capillary than that near the ends of capillary. Also, larger values of permeability coefficient, or smaller values of the diffusion coefficient produce a more obvious effect on oxygen transport.

Thus, this numerical results from this more comprehensive theoretical model indicate that the convection-diffusion of oxygen transport should be necessary to be considered in the relevant studies, its important role of allowing oxygen to be transported more uniformly should be paid more attention and be studied further.

Chapter 3.

A 3D mathematical coupled model for the growth of avascular tumor

We presented the developed 3D mathematical model for studying the growth of avascular tumor, which couples with the migration of TCs, the degradation of ECM, the transport of MDEs, the seepage of tissue fluid, and the transport of oxygen, and will shows the numerical results calculated from this coupled model and the relevant discussion in this Chapter. Basing on the numerical results, we also observed some important findings on the value of Matrix-degrading enzymes (or MMPs) as novel biomarkers for early cancer diagnosis, which will also be further studied in the future.

3.1 Abstract

We develop a coupled mathematical model of avascular tumor growth based on porous media mechanics. This comprises of the migration of tumor cells (TCs), the degradation of extracellular matrix (ECM), the transport of matrix-degrading enzymes (MDEs), the seepage of tissue fluid and the supplement and consumption of oxygen. The simulation of a solid tumor grows in the micro-environment composed of the pre-existing capillaries and the surrounding tissues, and the specific property of changing porosity with the growth of TCs in a tumor micro-environment is taken into account. We propose functional coefficients for fluid seepage and oxygen diffusion, and incorporate the convection-diffusion of oxygen and the convection of MDEs. From this modified model the main findings include: first, a solid tumor originating in the inlet region undergoes necrosis in the outlet region because of a low supply of oxygen, while a solid tumor originating in the outlet region undergoes necrosis at the primary site because of overconsumption of oxygen; second, tumors further from capillaries grow faster than tumors close to adjacent capillaries; third, the pre-existing capillaries greatly impacts the transport of those chemical factors involved in tumor growth, further impacting tumor migration and necrosis.

Many previous studies have predicted the importance of MDEs for diagnosis of certain cancers, for increased MDEs (matrix-degrading enzymes) are experimentally examined in early stages of solid tumors, i.e. avascular tumors. However, no quantitative standard exists for MDEs as diagnostic bio-markers. To quantify MDE transport during the avascular stage of solid tumors, a mathematical model based on diffusion-advection models is proposed, coupling MDE convection and diffusion, the amoeboid-like migration of TCs (tumor cells), fluid seepage, ECM (extracellular matrix) degradation, and oxygen convection and diffusion. A specific capillary-tissue micro-environment for avascular tumors with changing porosity for the porous medium is incorporated. The numerical results indicate that TCs enter the blood long before cell necrosis, however, MDEs diffuse much further than the TC migration, and enter the blood circulation much earlier than TCs; when a solid tumor originates at the inlet end, MDEs enter the blood 12 cell cycles earlier than TCs; when a tumor originates at the outlet end, MDEs enter the blood 15 cell cycles earlier than TCs. These results theoretically demonstrate the diagnostic significance of MDEs for early cancers, quantitatively provide a basis to determine the tumor stage when MDEs can be detected in blood, and estimate solid tumor size by measuring MDE concentrations in blood.

3.2 Coupled mathematical model with the migration of TCs, the degradation of ECM, the transport of MDEs, the seepage of fluid tissue, and the transport of oxygen

Based on the reaction-diffusion-convection model, a coupled system of equations for the growth of an avascular tumor is developed.

3.2.1 Modeling the migration of TCs

A cell's migration follows either mesenchymal or amoeboid patterns, and indeed certain cell types can follow both of these (Pankov et al 2010). Although the exact mechanisms of these migration types remain unknown, several assumptions have been proposed, such as using Fick's random diffusion law to model the random motion of TCs (Anderson 2005). This assumption is employed here, and the conservation equation for the concentration of TCs, C_n, is given by

$$\frac{\partial C_n}{\partial t} = D_n \nabla^2 C_n + \beta C_n - \eta. \tag{3.1}$$

where D_n is the motility coefficient that measures how easily TCs are able to migrate, β is the proliferation coefficient and η represents the death coefficient, which is related to the concentration of necrotic TCs. βC_n then represents the proliferation of TCs. The haptotaxis flux of tumors, which is used to model the effect of the ECM on a TC's migration and has been used in some previous models (Anderson 2005), is not incorporated here because it has not yet been physiologically demonstrated that haptotaxis occurs *in vivo* (Condeelis and Segall 2003). We suggest that the assumption of haptotaxis of TCs to the ECM does not have enough physical background to warrant inclusion. Differing from previous models, we incorporate the effect of the ECM on TC migration into the motility coefficient of the TCs, D_n, using a functional coefficient of D_n related to the ECM concentration C_e. Assume a power laws to exist between D_n and C_e, $D_n(t) = D_0(C_{e0}/C_e(t))^{1/2}$, where D_0 is a constant representing the initial TC motility coefficient and C_{e0} is the initial concentration. As cells often divide incompletely, the cell division constant is assumed to be 1.4, and the cell cycle β is simply taken to be 12 hours. Living TCs, quiescent TCs, necrotic TCs and dead cells are all modeled, where the quiescent TCs are assumed to consume half of the oxygen of living cells and the necrotic TCs are assumed to consume a quarter of the oxygen of living cells (Anderson 2005). We assume 20% of necrotic TCs die after one cell cycle: $\eta = \eta(t_l, C_{O_2 cr})$, where the death age is $t_l = 12$hour, $C_{O_2 cr} = 1/4 C_{used O_2}$ is the critical value of oxygen

consumption for necrotic cells and C_{usedO_2} is the oxygen consumption of living cells. Note that dead cells are removed from the TC concentration, but they still occupy space in the tissue, affecting the porosity of porous media.

3.2.2 Modeling the transport of ECM, MDEs and oxygen

The degradation equation of the ECM was proposed (Anderson 2005), and is given by

$$\frac{\partial C_e}{\partial t} = -\delta C_m C_e, \tag{3.2}$$

where δ is a positive constant representing the degradation parameter of the ECM. MDEs are transported according to the reaction-diffusion-convection equation,

$$\frac{\partial C_m}{\partial t} = D_m \nabla^2 C_m - \frac{\partial}{\partial x_i}(C_m V_i) + g(C_n, C_m) - h(C_n, C_m), \tag{3.3}$$

where C_m is the MDE concentration, D_m is a positive constant of diffusion coefficient and V_i is the seepage velocity of tissue fluid. Assume $g = \mu C_n$ represents MDE production and $h = \lambda C_m$ represents MDE nature decay, where μ and λ are positive constants (Anderson 2005). Oxygen transport similarly complies with the reaction-diffusion-convection equation, where

$$\frac{\partial C_{O_2}}{\partial t} = D_{O_2} \nabla^2 C_{O_2} - \frac{\partial}{\partial x_i}(C_{O_2} V_i) + S - I, \tag{3.4}$$

where C_{O_2} is oxygen concentration, D_{O_2} is the diffusion coefficient of oxygen and is related to C_n, S is the source of oxygen and I is the sink of oxygen. Notably, many previous models (Anderson 2005;Cai et al 2011), assumed V_i is zero, i.e. the convection-diffusion term is neglected. However, the influence of convection-diffusion on macromolecular transport at a micro level has been demonstrated and applied,Schuff et al 2013a and its influence on oxygen transportation was also predicted (Pittman 2013). We therefore include both the convection-diffusion of MDEs and oxygen, and V_i is calculated from Eq. (3.5).

3.2.3 Modeling the seepage of tissue fluid

The seepage velocity $V_i = k_i p_{,i}$ is coupled into the governing equations of the MDEs and oxygen to calculate their convection-diffusion terms. The seepage of tissue fluid obeys Darcy's law, and the mass equilibrium equation per volume of fluid is given by

$$(k_i p_{,i})_{,i} = \beta n \frac{\partial p}{\partial t} + \frac{\partial n}{\partial t} + W, \tag{3.5}$$

where k is the permeability coefficient of the fluid, p is the pore pressure, n is the porosity of the porous media, βn is the compressibility coefficient of the fluid, W is the source and sink of the fluid and i from 1 to 3 respectively indicates the x, y and z-direction. In this model, the specific micro-environment for avascular tumor growth where the permeability coefficient and the diffusion coefficient of oxygen is varied with TC concentration is coupled into the seepage equation and oxygen equation. The increase of TCs leads the permeability coefficient to be reduced, and we therefore assume $k = k(n) = k(C_n)$. An power laws in porous media generally existing between the permeability coefficient and the porosity of porous media has been proved experimentally, where $k = k_0(n/(1-n))^{4.17}$ (Villar and Lloret 2001;Villar et al 2008) For the tumor micro-environment, the initial porosity is taken to be 0.3. Since TCs will fill the pores during tumor growth, the porosity reduces according to $n = 0.3 - C_n(t)$, and the volumetric concentration of TCs is given by $1 - n = 0.7 + C_n(t)$, and therefore $k = k_0[(0.3 - C_n(t))/(0.7 + C_n(t))]^{4.17}$ is employed into Eq. (3.5). In porous media the regulation of diffusion coefficient is similar to the permeability coefficient, and we assume the same mathematical expressions apply to $D_{O_2} = D_{0O_2}[(0.3 - C_n(t))/(0.7 + C_n(t))]^{4.17}$.

3.2.4 The coupled mathematical model for solid tumor growth

The coupled mathematical model for avascular tumor growth comprises Eq. (3.1), Eq. (3.2), Eq. (3.3), Eq. (3.4) and Eq. (3.5), to give

$$\begin{aligned}
&\frac{\partial C_n}{\partial t} = D_n \nabla^2 C_n + \beta C_n - \eta \\
&\frac{\partial C_e}{\partial t} = -\delta C_m C_e \\
&\frac{\partial C_m}{\partial t} = D_m \nabla^2 C_m - \frac{\partial}{\partial x_i}(C_m V_i) + \mu C_n - \lambda C_m \\
&(k_i p_{,i})_{,i} = \beta n \frac{\partial p}{\partial t} + \frac{\partial n}{\partial t} + W \\
&\frac{\partial C_{O_2}}{\partial t} = D_{O_2} \nabla^2 C_{O_2} - \frac{\partial}{\partial x_i}(C_{O_2} V_i) + S - I(C_{normal}, C_n)
\end{aligned} \tag{3.6}$$

where D_n, k and D_{O_2} are all functions of t. To solve the governing equations Eq. (3.6) we use a finite element method program.

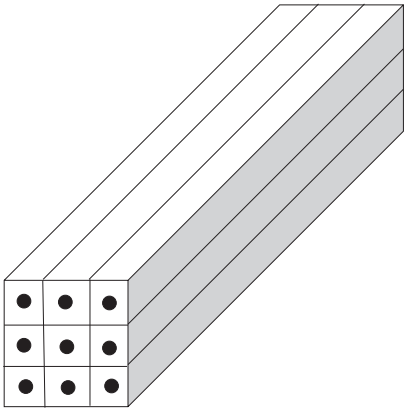

(a)

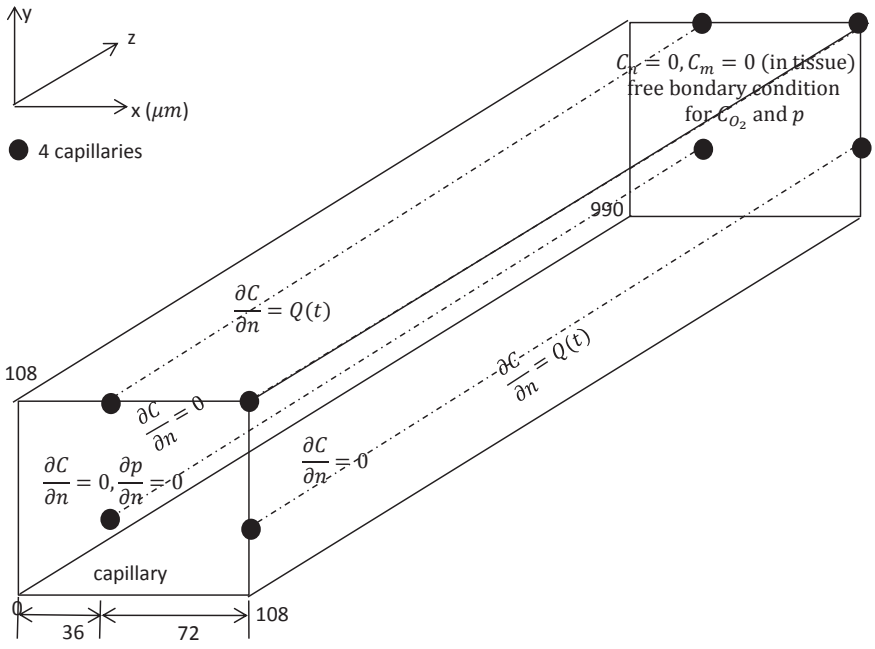

(b)

Figure 3.1: Geometry and boundary condition of the model: (a) geometric structure of the model including the capillary, the capillary wall and the surrounding tissue; (b) according to the the symmetry of the structure, the simplification of the physical model from (a) and its boundary conditions.

Table 3.1: Parameters used in this mathematical model

Parameter	Description	Value	Unit
k_t	Permeability coefficient in tissue:a	$8\times10^{-6}\sim8\times10^{-8}$	$\mathrm{cm\,s^{-1}}$
k_w	Permeability coefficient at capillary wall:a	$2\times10^{-6}\sim2\times10^{-8}$	$\mathrm{cm\,s^{-1}}$
k_c	Permeability coefficient in capillary:a	0.005	$\mathrm{cm\,s^{-1}}$
$p_(t_0)$	Initial condition of pore pressure:b	0.26	$\mathrm{N\,cm^{-2}}$
D_{o_2t}	Oxygen diffusion coefficient in tissue:c	$2\times10^{-5}\sim2\times10^{-7}$	$\mathrm{cm^2\,s^{-1}}$
D_{o_2w}	Oxygen diffusion coefficient at capillary wall:c	$10^{-5}\sim10^{-7}$	$\mathrm{cm^2\,s^{-1}}$
D_{o_2c}	Oxygen diffusion coefficient in capillary:c	0.0003	$\mathrm{cm^2\,s^{-1}}$
$c_{used_{o_2}}$	Oxygen consumption rate of living cells:c	6.25×10^{-17}	$\mathrm{M\,cells\,s^{-1}}$
D_{nt}	TCs motility coefficient in tissue:c	2×10^{-12}	$\mathrm{cm^2\,s^{-1}}$
D_{nw}	TCs motility coefficient at capillary wall:c	10^{-12}	$\mathrm{cm^2\,s^{-1}}$
D_{nc}	TCs motility coefficient in capillary:c	3×10^{-5}	$\mathrm{cm^2\,s^{-1}}$
C_n0	Initial TCs concentration:c	$6.7*10^7$	$\mathrm{cells\,cm^{-3}}$
D_{mt}	MDEs diffusion coefficient in tissue:c	10^{-9}	$\mathrm{cm^2\,s^{-1}}$
D_{mw}	MDEs diffusion coefficient at capillary wall:c	10^{-9}	$\mathrm{cm^2\,s^{-1}}$
D_{mc}	MDEs diffusion coefficient in capillary:c	$3*10^{-5}$	$\mathrm{cm^2\,s^{-1}}$
C_e0	Initial ECM concentration:c	10^{-10}	M
δ	Degradation coefficient of ECM:c	$1.3*10^2$	$\mathrm{cm^3\,M^{-1}\,s^{-1}}$
λ	Decay coefficient of MDEs:c	$1.7*10^{-8}$	$\mathrm{s^{-1}}$
μ	Production coefficient of MDEs:c	$1.7*10^{-18}$	$\mathrm{M\,cells\,s^{-1}}$
$C_{o_2}(t_0)$	Initial oxygen concentration in capillary:d	0.1664×10^{-2}	$\mathrm{ml\,ml^{-1}}$

a: Chapman et al 2008; b: Zweifach 1974; c: Anderson 2005; d: Hall 2010.

3.3 Calculating model and boundary condition

The computational area is symmetrically simplified to a cube including four parallel capillaries, the capillary wall and their surrounding tissues. The distance between two adjacent capillaries is 72μm, the radius of each capillary is 3μm, the thickness of the capillary wall is 0.3μm and the length of each capillary is 990μm. Since the size of an avascular tumor approximates 1-2mm^3, which has been experimentally proven, taking the length of the computational area to be nearly 1 mm would be reasonable. The boundary conditions are shown in Fig.3.1, where the concentration of each phase in Eq. (3.6) is generally represented by C, $\partial C/\partial n$ is the normal derivative of C and Q is the flux. For the four surfaces in the capillary direction, two surfaces are through the capillaries, wherein the concentration complies with $\partial C/\partial n = Q(t)$, and the other two surfaces are through the tissue only, wherein the concentration complies with $\partial C/\partial n = 0$; the surface located at the inlet end of capillaries complies with $\partial C/\partial n = 0$, and the pore pressure complies with $\partial p/\partial n = 0$; the surface located at the outlet complies with $C_n, C_m = 0$ and the concentration and pore pressure in the capillaries takes the free boundary conditions. The physical and mechanical parameters are listed in Table3.1.

3.4 Results

The cell cycle is taken to be 12 hours, to represent the period for cell division. TC concentration is closely related to the cell cycle, and therefore the results below are shown using the number of the cell cycle, which can not only indicate the evolution of each phase over time, but more importantly can reveal the interactions between each phase and the tumor itself. Two cases are simulated for the solid tumor originating from two different locations; case I, originating at the inlet region, i.e. at x=0μm, y=0μm, z=0μm and case II, originating at the outlet region, i.e. at x=0μm, y=0μm, z=990μm.

3.4.1 Interactions among ECM, MDEs, oxygen, and TCs

To study how the ECM, MDEs, oxygen and TCs themselves affect the avascular tumor growth, the concentration distribution results of these at five typical times are presented in Fig.3.2, Fig.3.3, and Fig.3.4 for case I. Initially, when a small amount of MDE has been produced, the ECM has not been degraded and the concentration is at 10^{-8}M of the maximum. After one cell cycle, the TCs begin to divide, and rapidly surround the primary tumor; a small amount of TC appears in the middle of the capillary bed, and correspondingly MDEs rapidly increase and are delivered further than the areas that the TCs have invaded. The ECM is greatly reduced from the primary site to the middle region, and partly reduced in the outlet region. At the 19th cell cycles the TCs have surrounded the adjacent capillary, and MDEs have been transported up to 1 mm away from the primary tumor. The ECM around the primary tumor reduces to 10^{-14}M of the minimum concentration, and hence TCs migrate much faster, spreading to the middle of the capillary bed and even partly to the outlet region. MDEs continue to spread and the concentration at about the 50th cell cycles increases to 10^3 times as large as that found after the 19th cell cycles. The ECM completely reduces to the minimum concentration inside 1 mm from the primary tumor, which indicates that the adhesion of TCs is greatly reduced. The TCs have migrated to the outlet region, with an average concentration of approximately 10^{-4}. More oxygen consumption causes serious hypoxia to occur in the middle region and the outlet region. TCs that have completely invaded the tissue further than 1 mm from the primary tumor are typically shown at the 84th cell cycles (about 1005 hours). However, lasting hypoxia leads the living TCs to become quiescent and even necrotic, before finally dying, slowing the demand for oxygen. Because of a large amount of cell death, the concentration of

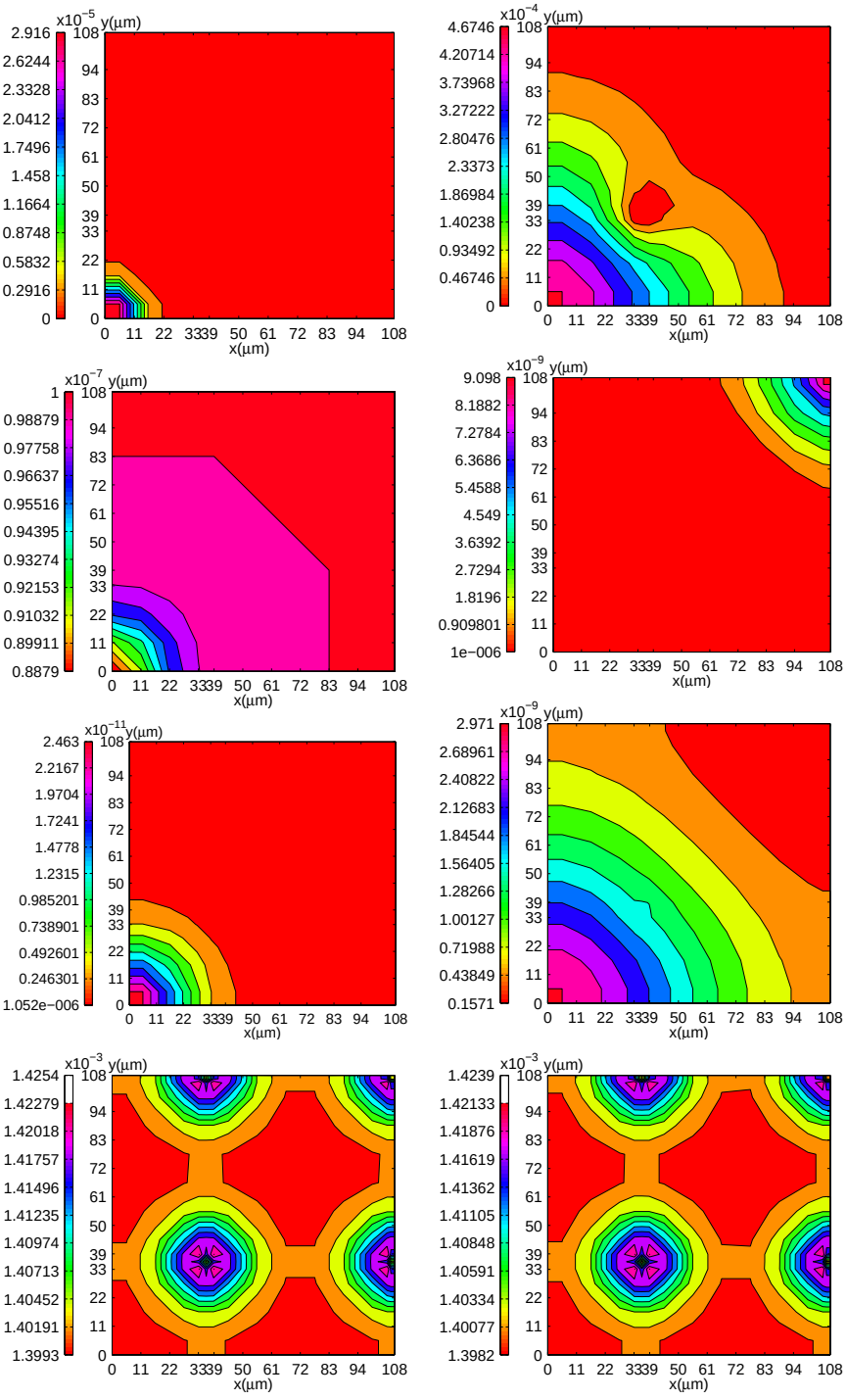

(a) 1st cell cycle, t=12.17hour (b) 19th cell cycle, t=227.54hour

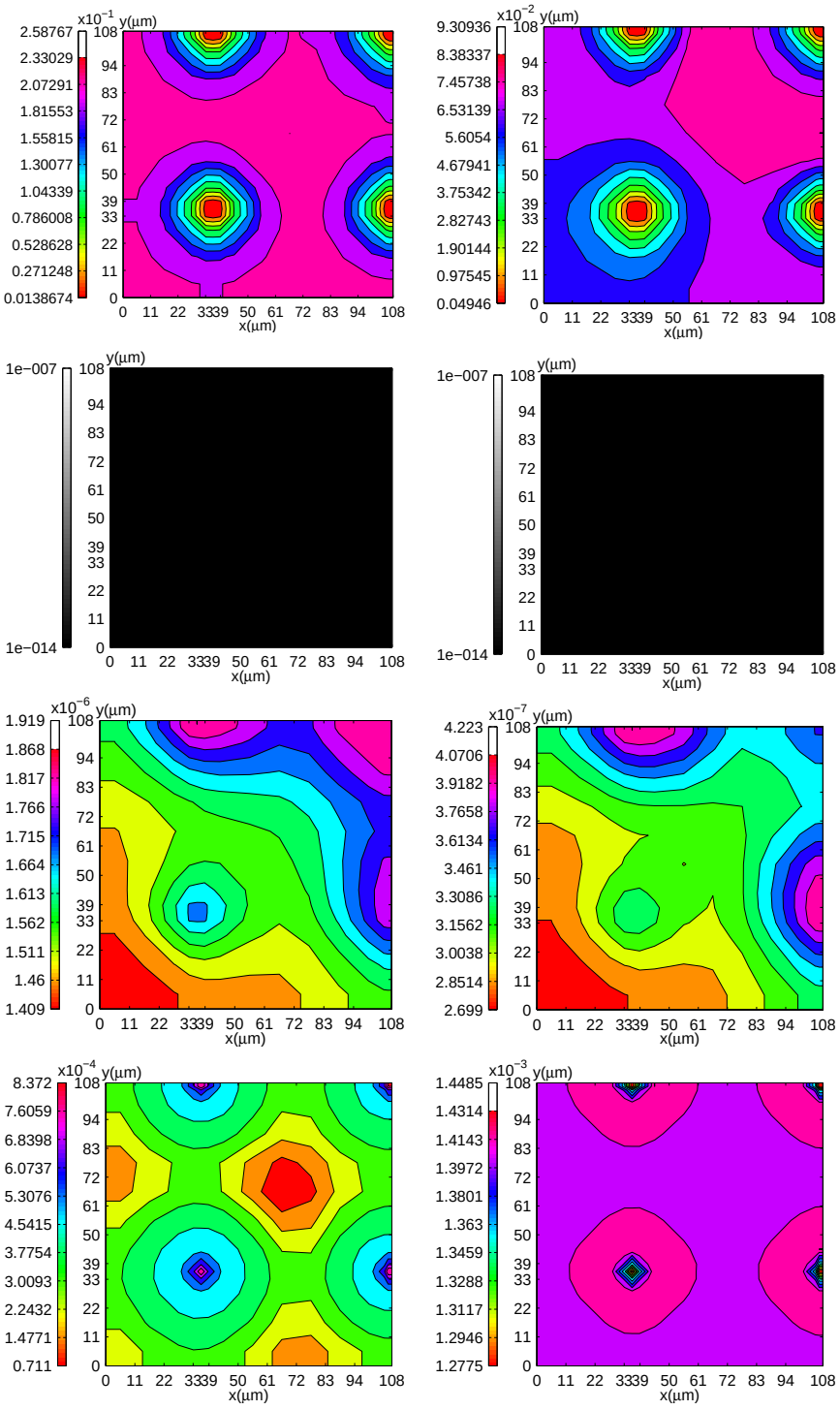

(c) 50th cell cycle, t=597.54hour (d) 84th cell cycle, t=1004.54hour

Figure 3.2: For case I, the growth of a solid tumor in the primary site (z=0μm) at four typical times is given here, at the (a) 1st (b) 19th (c) 50th and (d) 84th cell cycle, where the concentration distributions of TCs are presented in the first row (in cm^3/cm^3), those of the ECM are presented in the second row (in M), those of the MDEs are presented in the third row (in M) and those of oxygen are presented in the fourth row (in $ml\,O_2/ml\,tissue$).

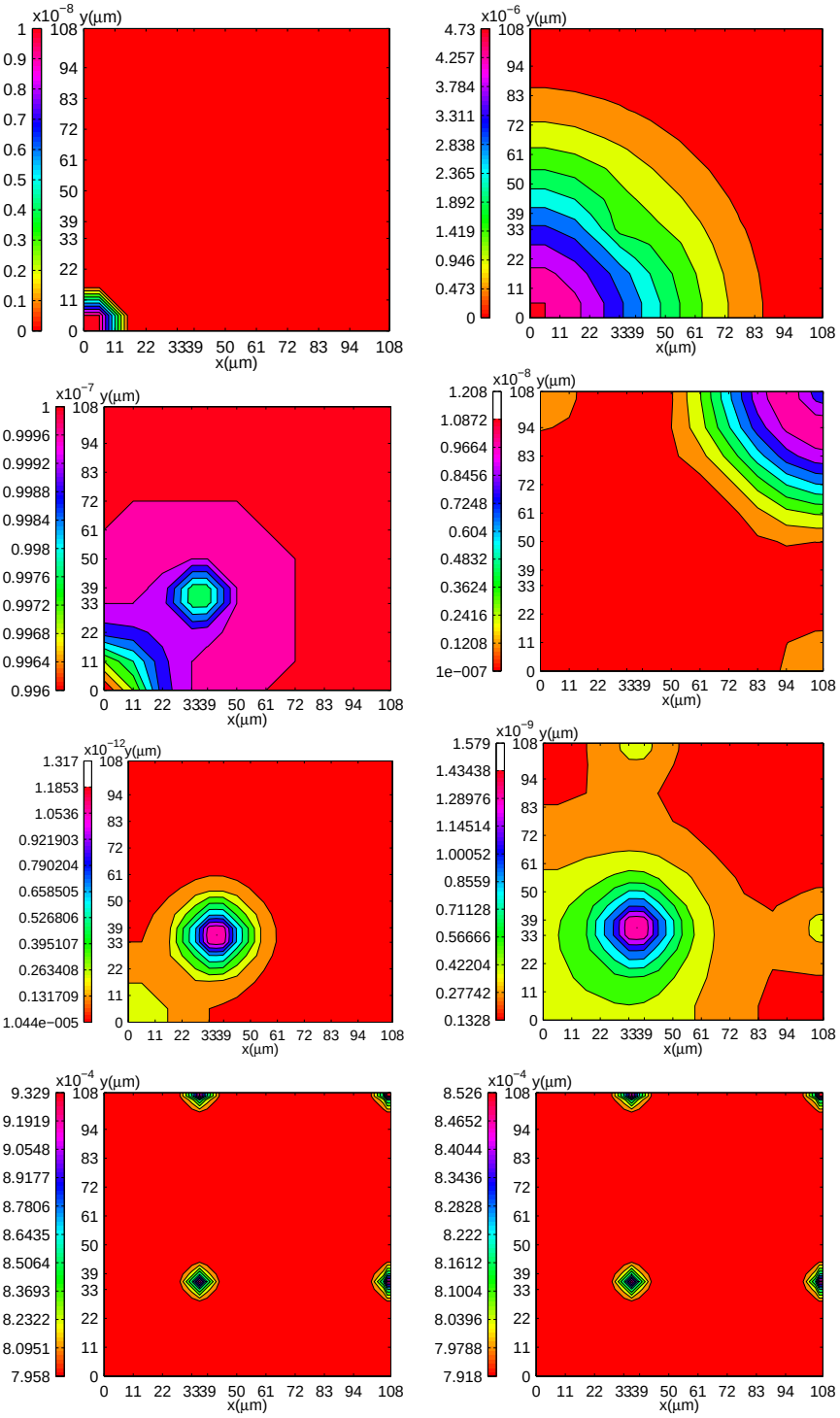

(a) 1st cell cycle, t=12.17hour (b) 19th cell cycle, t=227.54hour

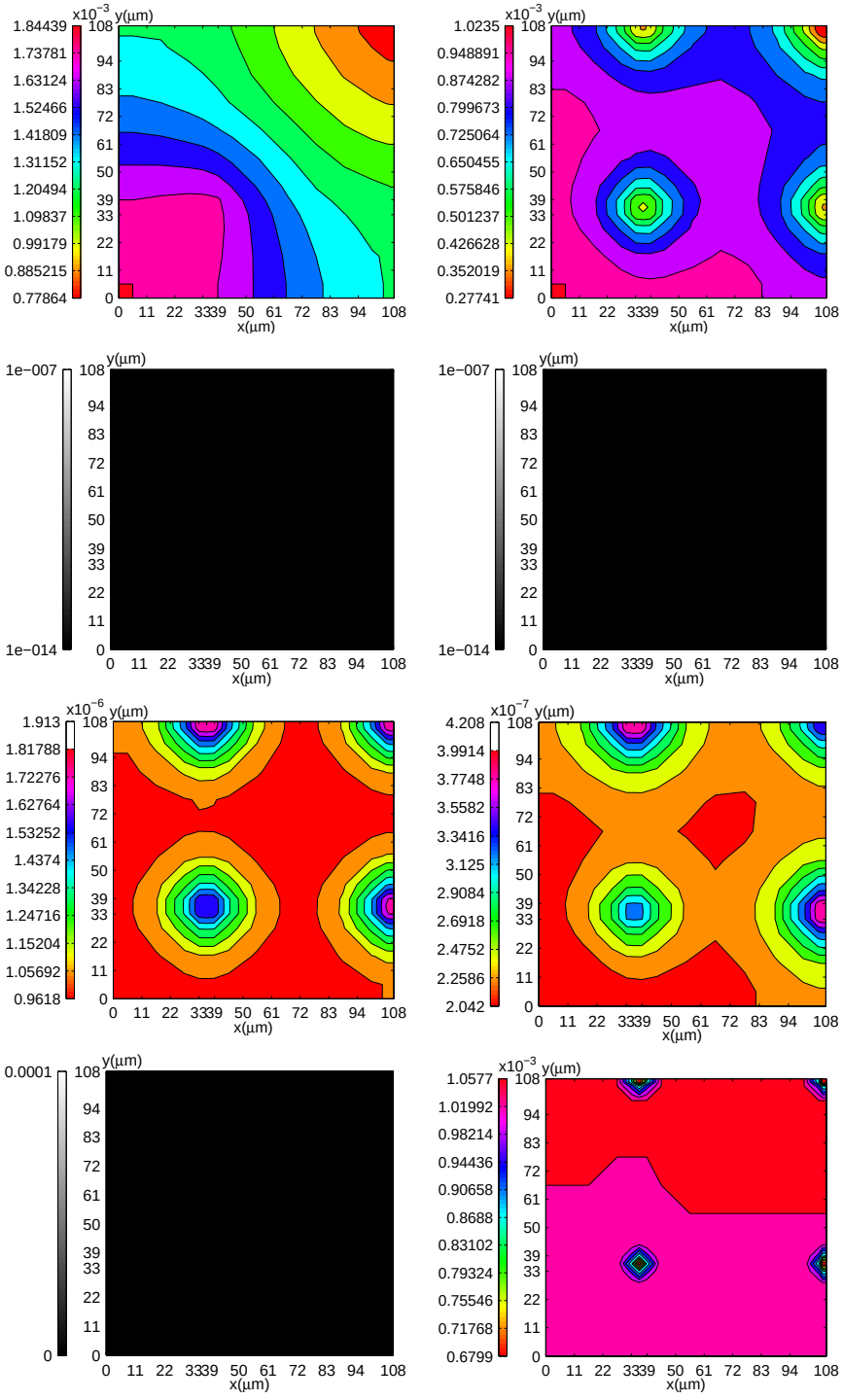

(c) 50th cell cycle, t=597.54hour (d) 84th cell cycle, t=1004.54hour

Figure 3.3: For case I, the growth of a solid tumor in the middle of capillary bed (z=550μm) at four typical times, at the (a) 1st (b) 19th (c) 50th and (d) 84th cell cycle, where the concentration distributions of TCs are presented in the first row (in cm^3/cm^3), those of the ECM are presented in the second row (in M), those of the MDEs are presented in the third row (in M) and those of oxygen are presented in the fourth row (in $ml\,O_2/ml\,tissue$).

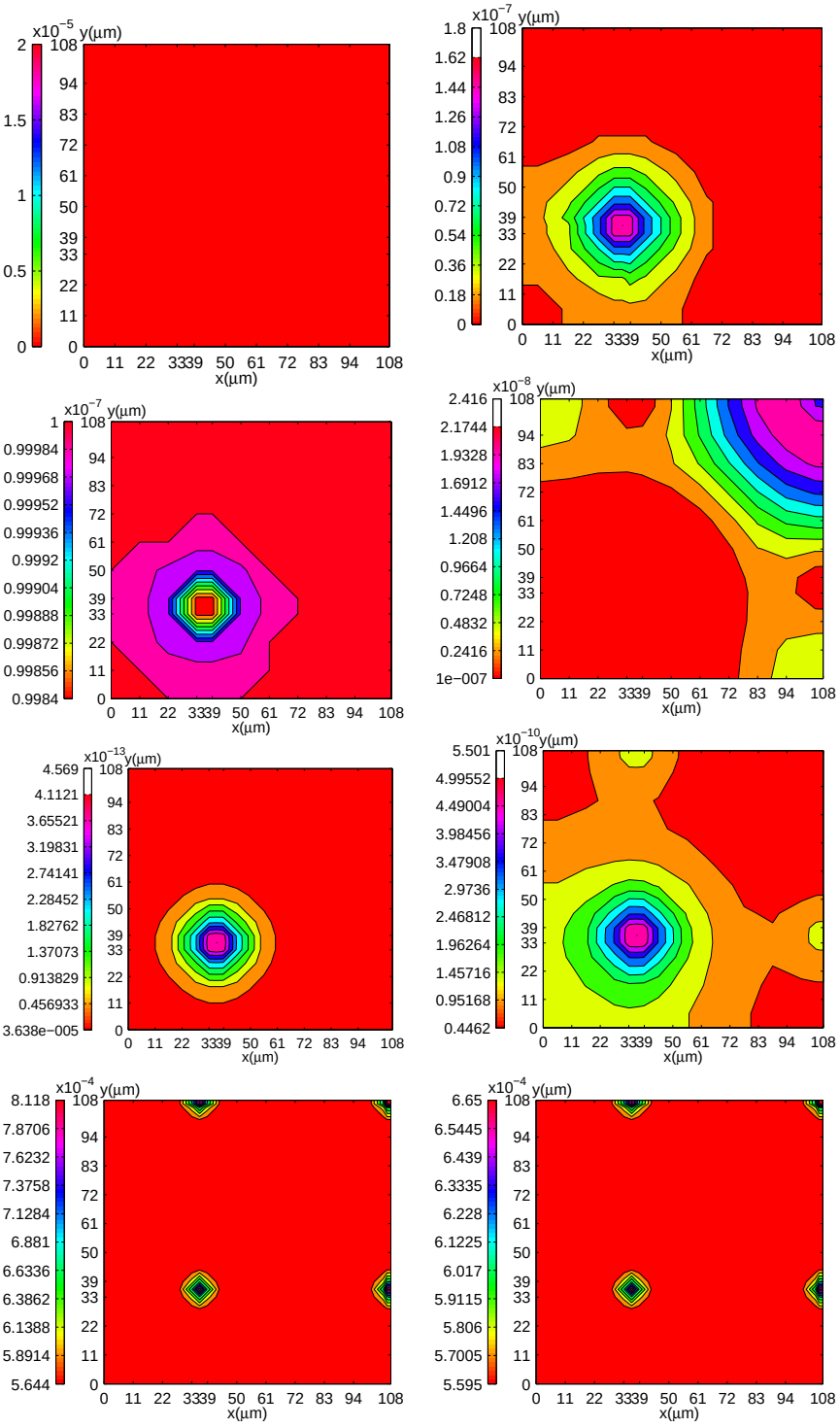

(a) 1st cell cycle, t=12.17hour (b) 19th cell cycle, t=227.54hour

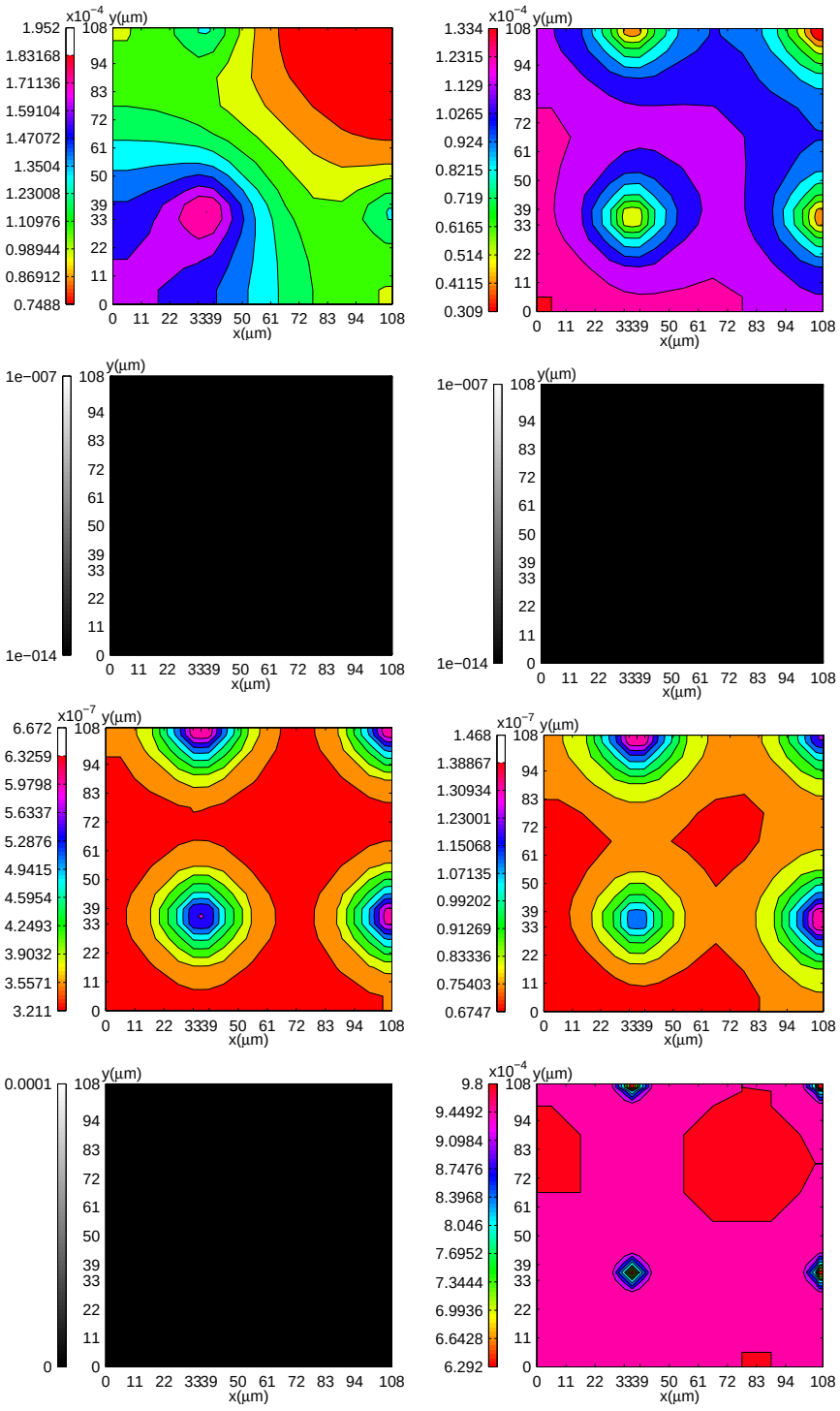

(c) 50th cell cycle, t=597.54hour (d) 84th cell cycle, t=1004.54hour

Figure 3.4: For case I, the growth of a solid tumor in the outlet of the capillary bed at four typical times is given here, at the (a) 1st (b) 19th (c) 50th (d) 84th cell cycle, where the concentration distributions of TCs are presented in the first row (in cm^3/cm^3) , those of the ECM are presented in the second row (in M), those of the MDEs are presented in the third row (in M) and those of oxygen are presented in the fourth row (in $ml\,O_2/ml\,tissue$).

oxygen progressively increases again.

3.4.2 Tumor necrosis

A comparison of necrotic process between case I and case II is now presented: the tumor evolution within the capillary, at the capillary wall and within the tissue, the TCs distribution including living TCs, quiescent TCs and necrotic TCs in one y-z slice at a fixed grid of x=33.3-38.7μm and in one x-y slice at a fixed grid of z=880-990μm are shown respectively in Fig.3.5(a), (b). The results show that the necrosis occurs first in the outlet region before rapidly spreading to the middle region. At the 42nd cell cycle, after approximately 504 hours, TCs in tissue from the outlet end to the middle region (440μm from the primary tumor) begin to become quiescent; at the 43rd cell cycle, TCs within the tissue from the outlet region up to 660μm from the primary tumor become necrotic; then, at the 45th cell cycle, the necrotic region reaches the tissue near the inlet end of the capillaries; at the 46th cell cycle, the necrotic region has completely invaded the tissue up to 1 mm from the primary tumor, except for the inlet end of the capillaries, and even TCs at the capillary walls begin to become quiescent from the outlet region; at the 47th cell cycle, TCs at the capillary walls become necrotic and the quiescent TCs at the capillary wall spread towards the inlet end; finally, at the 49th cell cycle, the region including the capillary walls and tissues within 1 mm of the primary tumor have become completely necrotic, except for the TCs closest to the inlet end of the capillaries, where oxygen remains in plentiful supply.

Comparing case II with case I, the distribution of cell condition in the same y-z slice and x-y slice is shown in Fig.3.5(c), (d). The results clearly indicate that for the tumor originating at the outlet end the necrosis occurs first in the primary site: at the 40th cell cycles, approximately 480 hours, the quiescent TCs initially occurred at the primary site, and 1 hour later the quiescent region becomes partly necrotic; at the 41st cell cycle, the quiescent region has further invaded the surrounding tissue of the adjacent capillary, and after 1 hour the necrotic region has also invaded these tissues; at the 42nd cell cycle, the quiescent region spreads to the neighboring four capillaries, and 1 hour later the necrotic region has partly invaded the tissue to a distance of about 100μm from the primary site. The results shown above depend mainly on the realistic simulation of the supply of oxygen in our model, which is shown below.

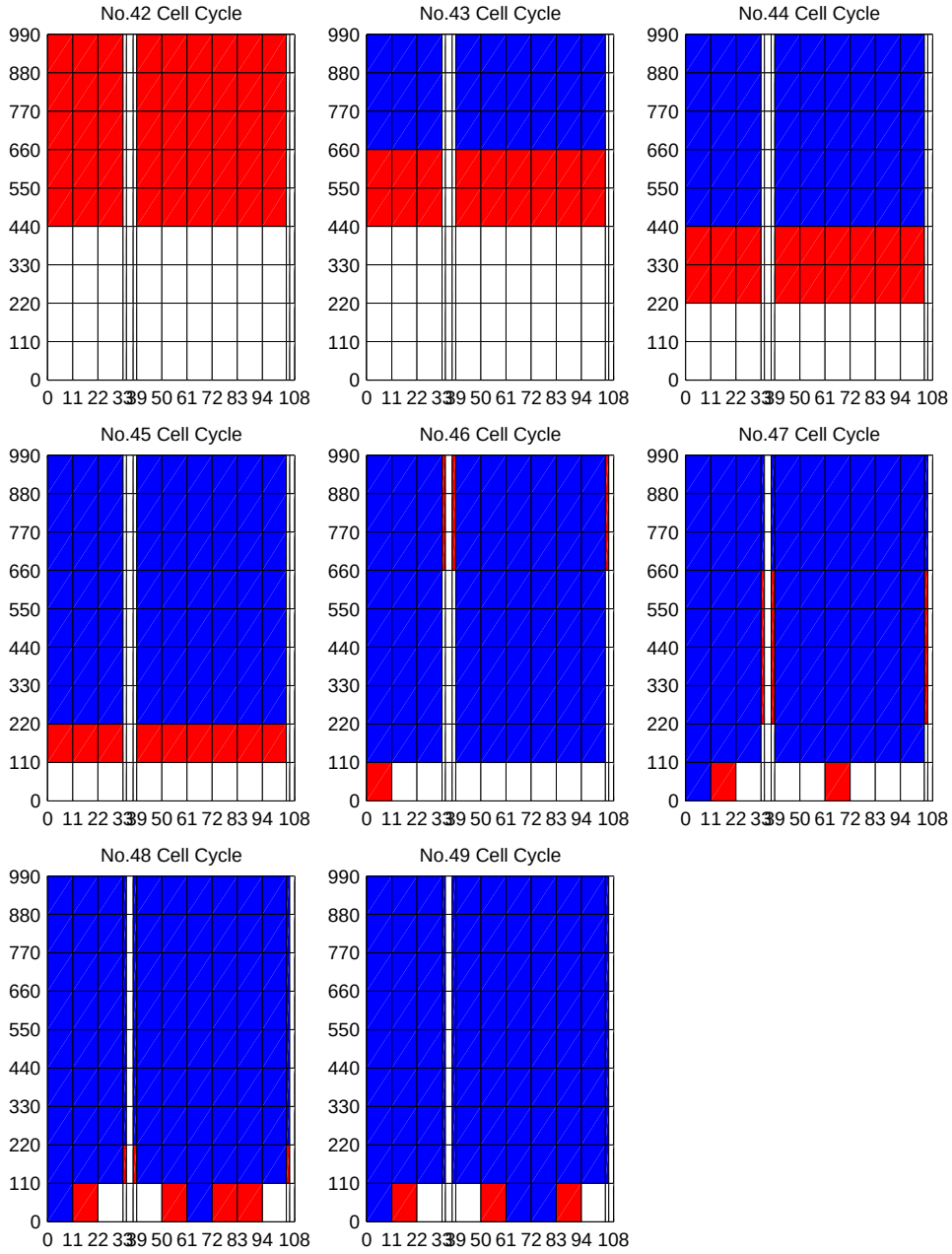

(a) TCs distribution at fixed x=38.7μm, in the case of the primary tumor originated from inlet region (case I)

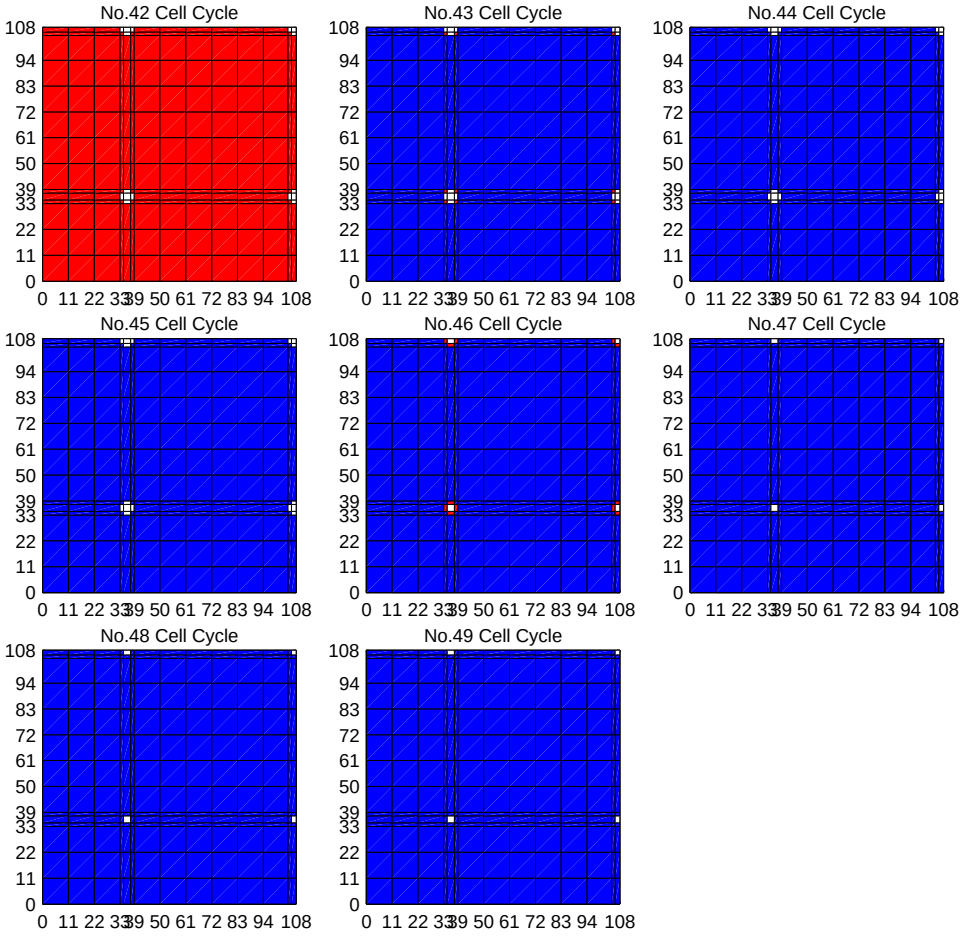

(b) TCs distribution at fixed z=990μm, in case I

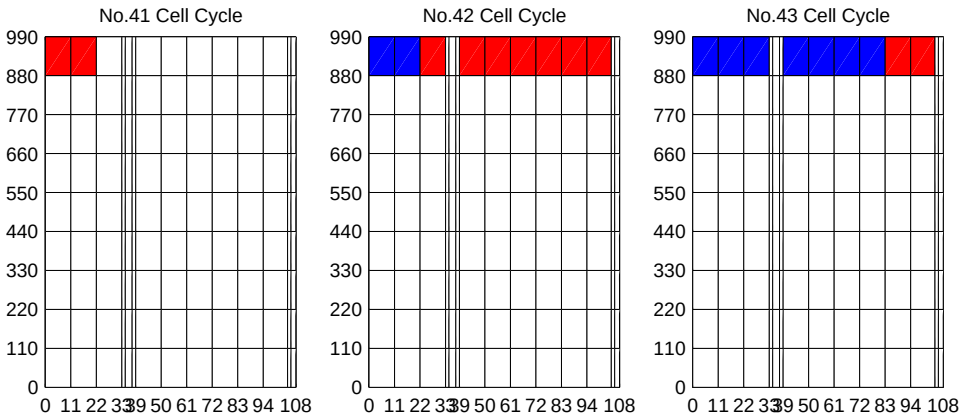

(c) TCs distribution at fixed x=38.7μm, in case II

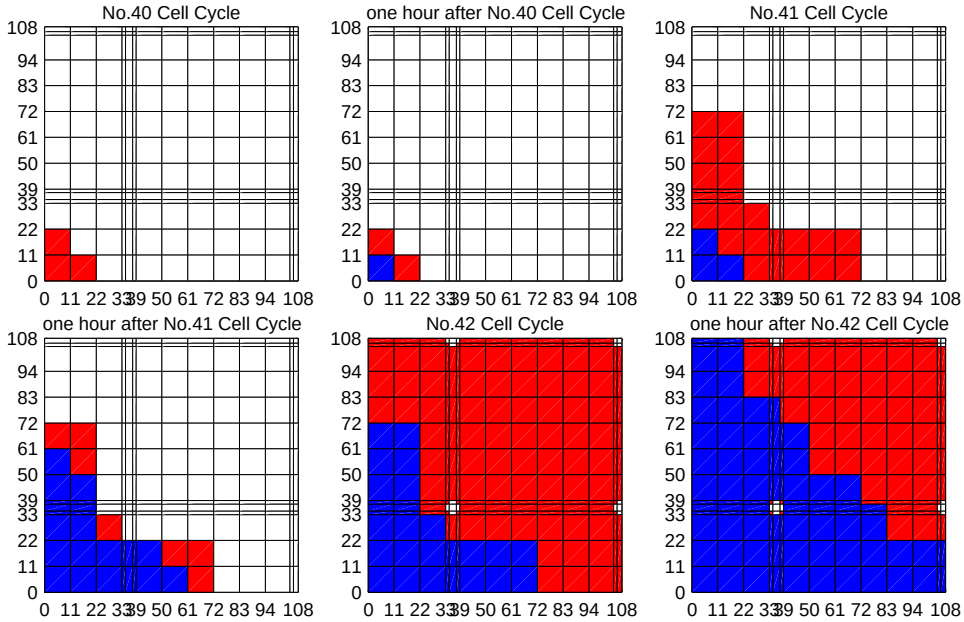

(d) TCs distribution at fixed z=990μm, in the case of primary tumor originated from outlet region (case II)

Figure 3.5: A comparison of the entire TC necrotic process between case I and case II, where white denotes living TCs, red denotes quiescent TCs and blue denotes necrotic TCs. The horizontal axis corresponds to the x-axis and the vertical axis corresponds to the z-axis in Fig.3.1: (a) TC distribution including living TCs, quiescent TCs and necrotic TCs, at fixed x=38.7μm in case I; (b) TC distribution at fixed z=990μm in case I; (c) TC distribution at fixed x=38.7μm in case I; (d) TC distribution at fixed z=990μm in case II. In (a) and (c), the grid of y=33-33.3, 38.7-39, 105-105.3 denotes the capillary wall, the grid of y=33.3-38.7, 105.3-108 denotes the capillary vessel and the remaining region denotes the tissue.

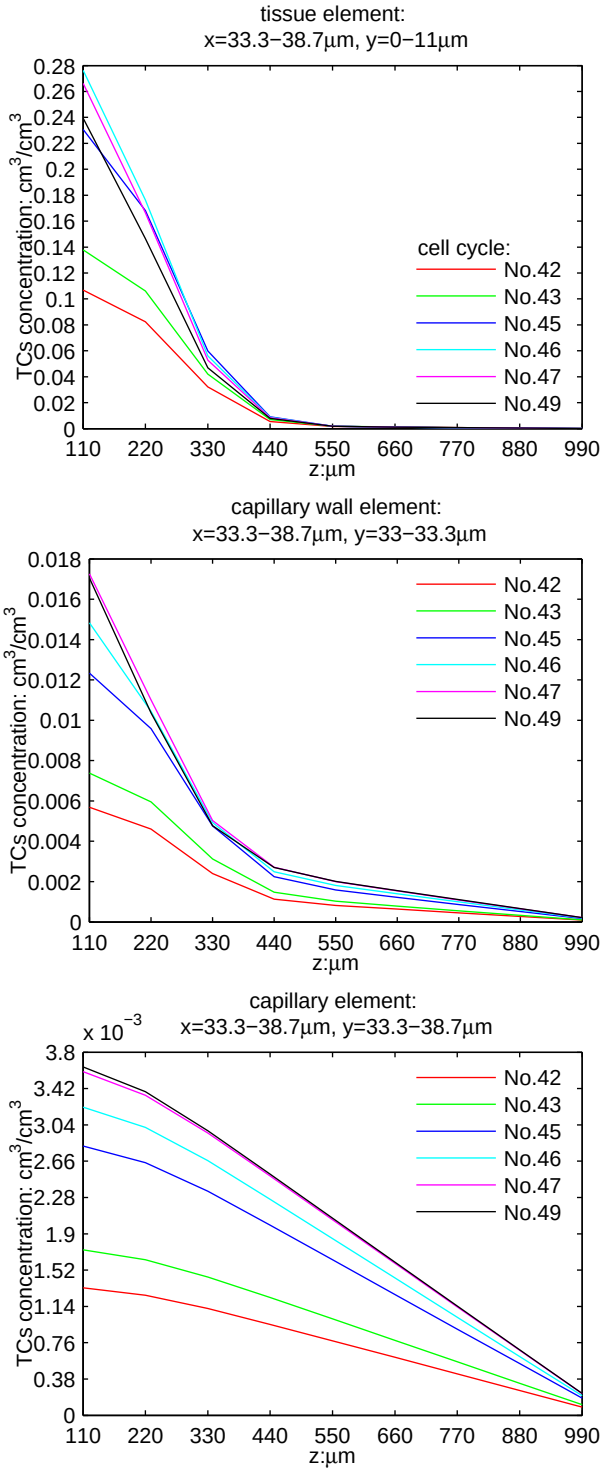

(a) TC concentration along capillary direction, in case I

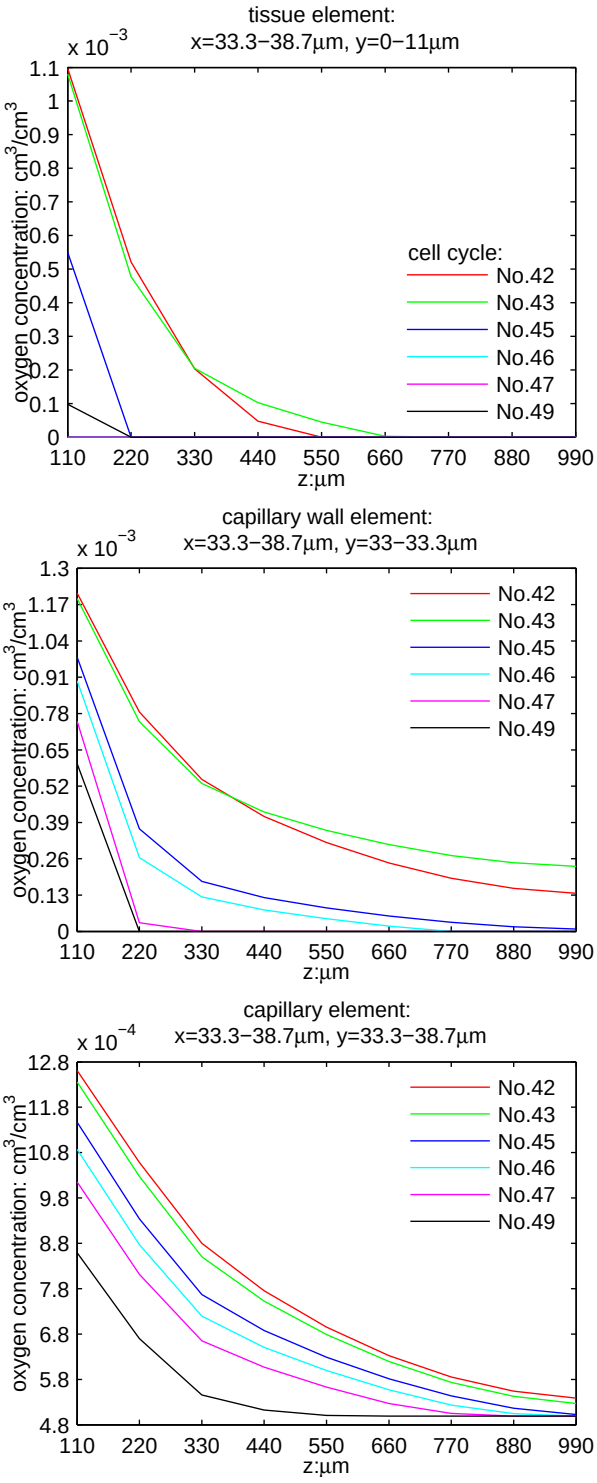

(b) O_2 concentration along capillary direction, in case I

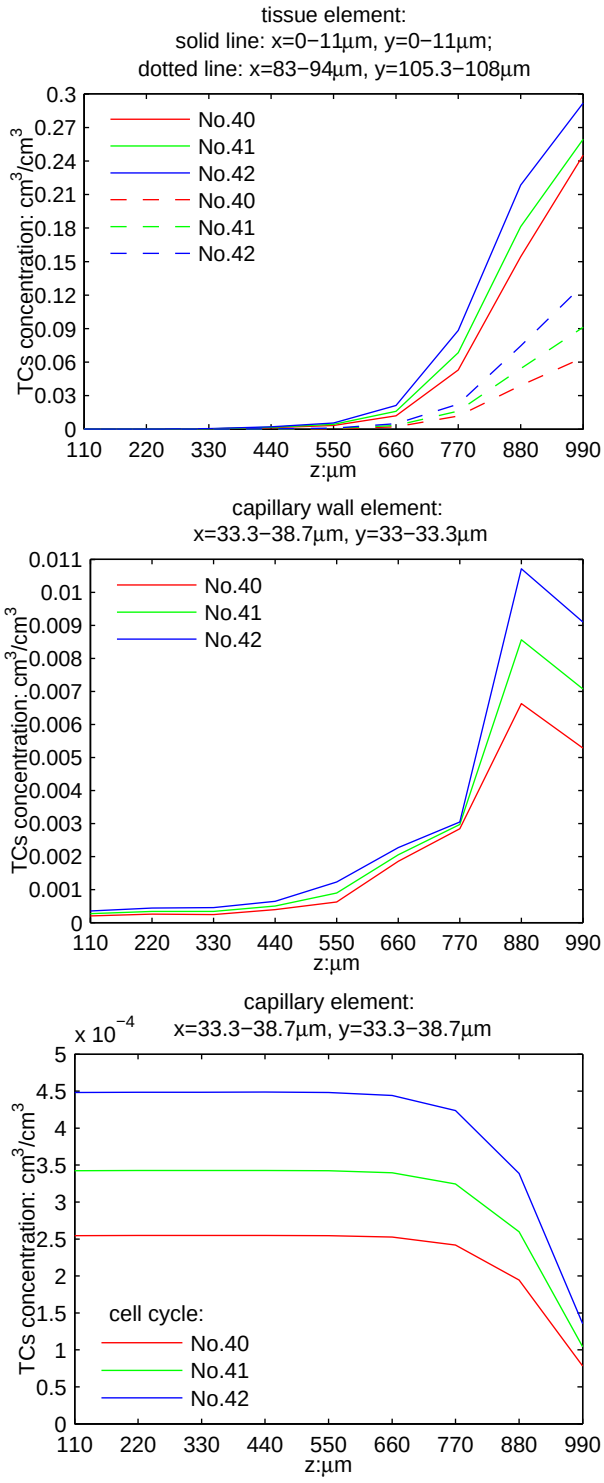

(c) TC concentration along capillary direction, in case II

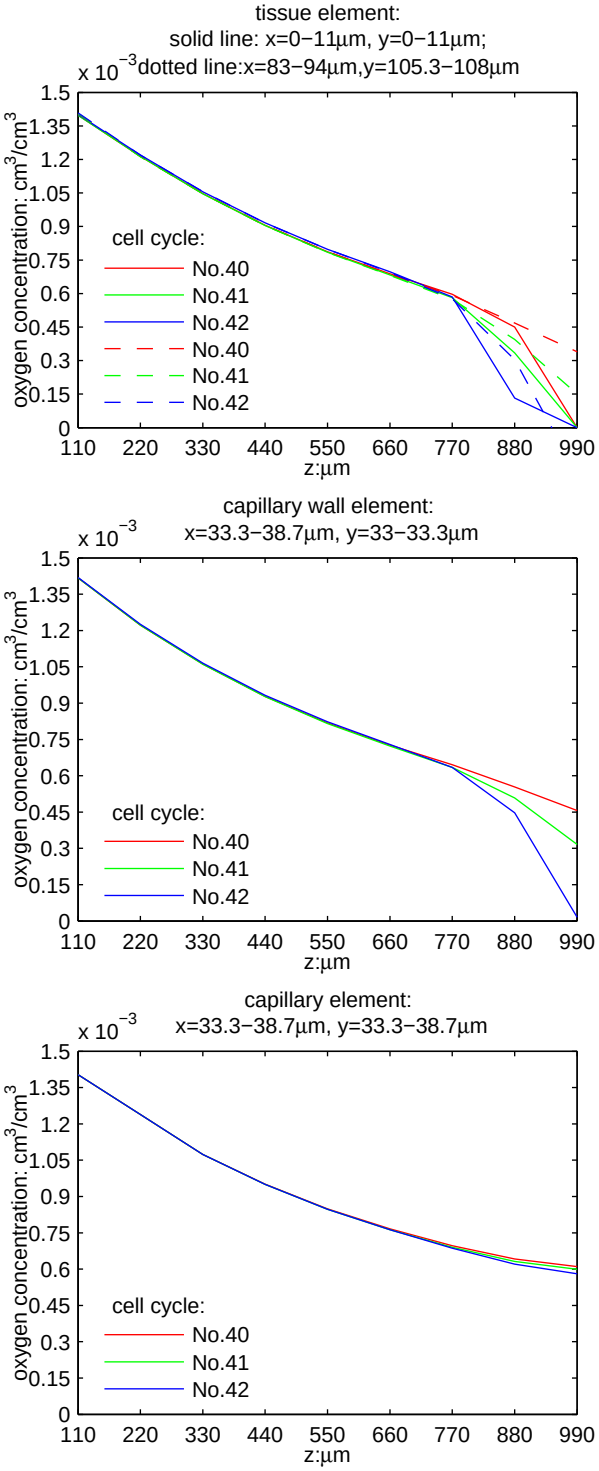

(d) O_2 concentration along capillary direction, in case II

Figure 3.6: A comparison of the effect of the TC concentration and the oxygen concentration on TC necrosis between case I and case II. The three subfigures respectively show the concentration in the tissue, at the capillary wall and in the capillary along the capillary direction from the inlet end to the outlet end. (a),(b): the color curves, which correspond to six particular cell cycles in Fig.3.5a; (c),(d): the color curves, which correspond to six particular times in Fig.3.5b.

3.4.3 The supply and consumption of oxygen

The evolution of the TCs and the oxygen at several typical cell cycles from the beginning of necrosis are compared for case I and case II, and are presented in Fig.3.6. The results indicate the cause of necrosis when a tumor originates at the inlet region. Along with TC growth, the TC concentration in the primary site increases to more than $0.1\text{cm}^3/\text{cm}^3$ at the 42nd cell cycle. In this time, TC concentration in tissue further than 440μm from the primary tumor is lower than $0.01\text{cm}^3/\text{cm}^3$, only a tenth of that at the primary site. However, the corresponding oxygen concentration within this tissue region is extremely low, less than $0.5 * 10^{-4}\text{cm}^3/\text{cm}^3$, and is less than a tenth of that at the primary site. Because of the low oxygen concentration, TCs begin to become quiescent in tissue further than 440μm from the primary tumor, and the tissue in the outlet end, where the hypoxia is most severe, is the earliest necrotic region. The TCs in tissue within 440μm remain living and continue to divide, and the concentration within 220μm increases to about $0.17\text{cm}^3/\text{cm}^3$ after 45 cell cycles. This is $0.06\text{cm}^3/\text{cm}^3$ higher than that at the 43rd cell cycle, and hence the oxygen is consumed by the increased TCs, leading to a quiescent region spreading to the tissue 220μm within the primary tumor. At 45 cell cycles the only living TCs left are located in the tissue closest to the inlet end of the capillaries, after which their concentration in the primary site increases to $0.28\text{cm}^3/\text{cm}^3$ at the 46th cell cycle and severe anoxia occurs, causing the invasion of necrosis to the primary tumor. With the occurrence of necrosis in the primary tumor, the TCs begin to reduce from the 46th cell cycle, and correspondingly the oxygen concentration partly increases. TCs are much less concentrated at the capillary wall than in the tissue, and the supply of oxygen is much greater, therefore the necrotic critical time is three cell cycles later than in the tissue. Similar to the tissue, the capillary walls begin to necrotize from the outlet end. Cells in the capillaries are not yet necrotic because of an adequate oxygen supply.

Fig.3.6(c), (d) show that the process of the initial necrosis occurring in case II is different from case I: at the 40th cell cycle the TC concentration within up to $0.24\text{cm}^3/\text{cm}^3$ of the primary site is four times higher than that in the tissue approximately 100μm from the primary site. A large amount of oxygen is consumed by these TCs at the primary site, resulting in early necrosis. As the TC concentration at the capillary wall is roughly one order of magnitude lower than in the tissue, the necrosis first occurs at the capillary wall two cell cycles later than in tissue. When the TC concentration increases to more than $0.009\text{cm}^3/\text{cm}^3$, the necrosis occurs at the outlet end of the capillary wall closest to

the primary tumor. Cells within the capillary are not yet necrotic. The results reveal that necrosis of the tumor is affected by the consumption of oxygen together with the supply of oxygen, but it is insufficient to simply attribute this to the fast growth of TCs causing the overconsumption of oxygen. As shown above, for a solid tumor originating at the inlet end, the earliest necrosis occurs at the outlet end where the TC concentration is lowest. This is primarily because fast growth of TCs surrounding the front capillary changes both the micro-environment where the tumor grows and reduces the porosity of the porous medium, which blocks the pathway of oxygen transport to the outlet end. Therefore, necrosis occurs even at the extremely low TC concentration present there. However, in the tissue surrounding the front capillary where oxygen is in sufficient supply, necrosis occurs because large amounts of oxygen are consumed. For a solid tumor originating at the outlet end, necrosis occurs earliest in the primary site, where the TC concentration is highest. This is because TCs increase from the outlet end, but oxygen is transported from the inlet end, and therefore the porosity surrounding the latter capillary reduces and the impact on the pathway of oxygen transport is small. Necrosis occurs mainly because oxygen consumption exceeds the supply.

3.4.4 Avascular tumor evolution

From the results in Fig.3.7, it is observed that the growth of avascular tumors can be divided into three stages, including the growth stage, a necrosis stage and cell death stage. In the first stage, fast tumor growth in the tissue begins from the 30th cell cycles, and reaches a peak after the 42nd cell cycle. From the 42nd the 46th cell cycle, the TC concentration in different locations successively reaches its peaks, after which the living TCs begin necrosis, and finally die. For high levels of cell death, the TCs significantly reduce in tissue within 300μm of the primary site, and slowly reduce after about the 75th cell cycle (900 hours). Fig.3.8 notes that before 240 hours there is almost no difference between case I and case II because of the growth of the tumor with sufficient oxygen supply, which is mainly influenced by the cell cycle and the motility coefficient. This agrees well with the findings presented (Scium et al 2013). Moreover, an important finding here is that before the tumor becomes necrotic, parts of it that are more distant from the capillaries grow faster than those that are close to a capillary. This finding will be discussed in detail in sect.3.5.2.

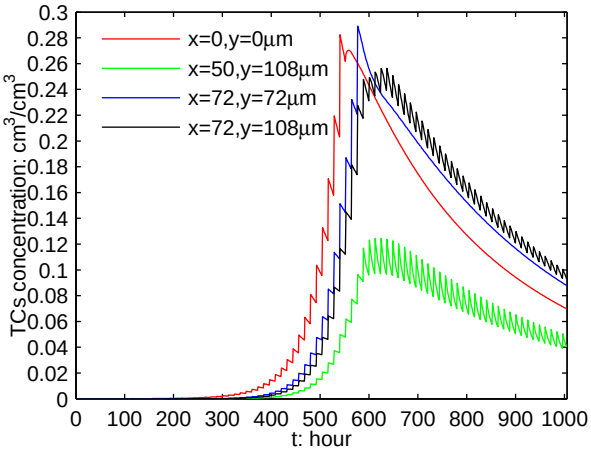

(a) z=0-110μm

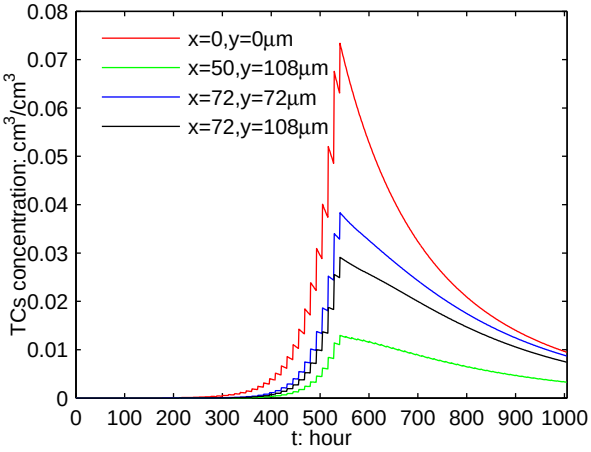

(b) z=220-330μm

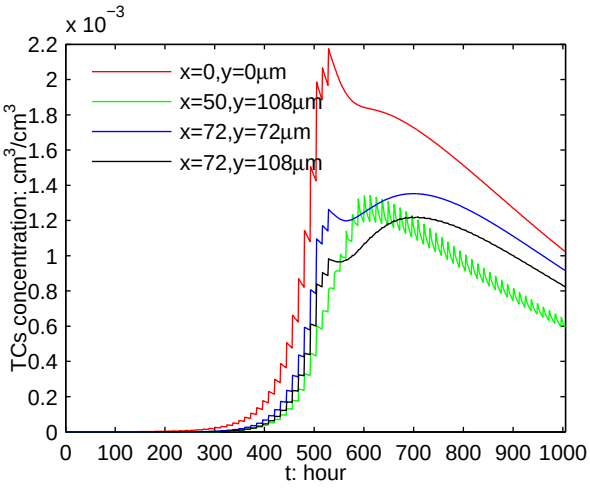

(c) z=440-550μm

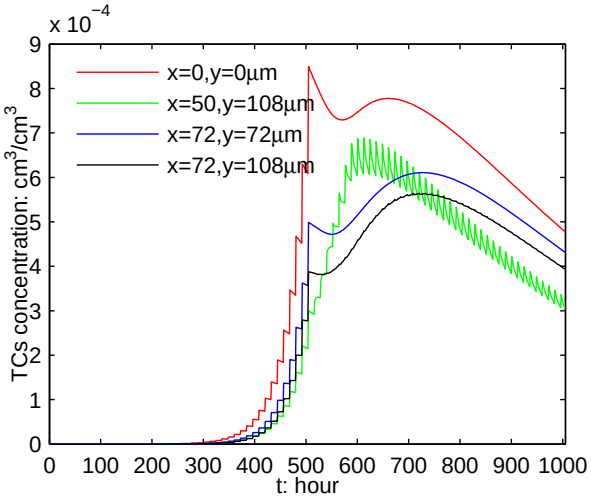

(d) z=660-770μm

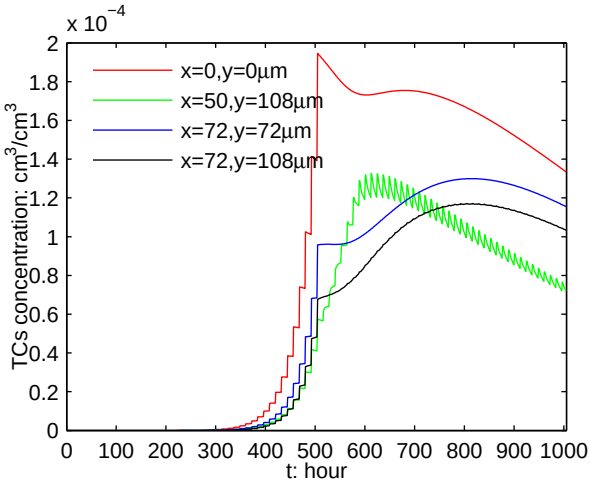

(e) z=880-990μm

Figure 3.7: A comparison of tumor growth in different locations: red, located at x=0,y=0μm, is the primary site, green, located at x=50, y=108μm, is closest to the adjacent capillary, blue, located at x=72,y=72μm, is furthest from four adjacent capillaries with a distance of more than 50μm, and black, located at x=72,y=108μm, is 30μm distant from two adjacent capillaries. (a)-(e) respectively represent different z-axes.

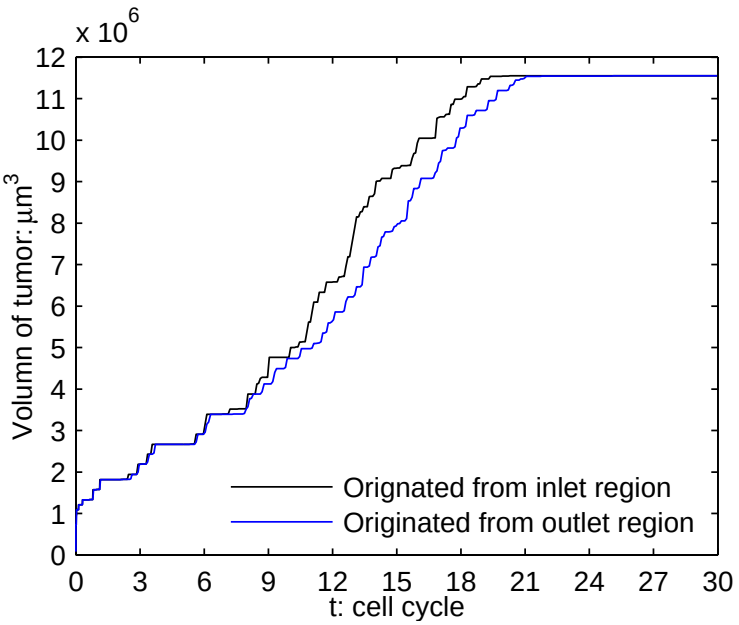

Figure 3.8: The evolution of tumor volume over time with units μm^3.

3.4.5 TC concentration into blood circulation over time

The TCs that are located in the middle of the four capillaries are easiest to grow, because this is where nutrients and oxygen are most difficult to supply, and the circulation is poor. Therefore, we simulate two cases of solid tumors originating from two different locations, which are both located in the middle of the four capillaries: case I, originating at the inlet region, i.e. at x=0µm, y=0µm, z=0µm, and case II, originating at the outlet region, i.e. at x=0µm, y=0µm, z=990µm. As soon as the TCs migrate into the initial pre-existing capillaries, they will rapidly invade the blood circulation and can easily lead the tumor to metastasize. Therefore, we need to investigate the stage (i.e. the exact time) at which the TCs can migrate into the blood circulation, as presented in Fig.3.9: for case I, a small quantity of TCs with a concentration of $10^{-8}cm^3/cm^3$ initially enter the blood circulation from the outlet end of the closest capillary at approximately 12 cell cycles (144 hours); for case II, the TCs initially enter the blood circulation at approximately 15 cell cycles (184 hours). After that, the TCs grow within the capillaries very rapidly, because the permeability coefficient and the diffusion coefficient of oxygen within the capillaries are much higher than those within the tissues. These results emphasize the important finding that the TCs had entered into the blood circulation through the pre-existing capillaries long before the cells began to necrotize (because of lack of oxygen), and the vascular network was remodeled, and this also indicates the critical importance of early cancer detection. However, it is generally believed that

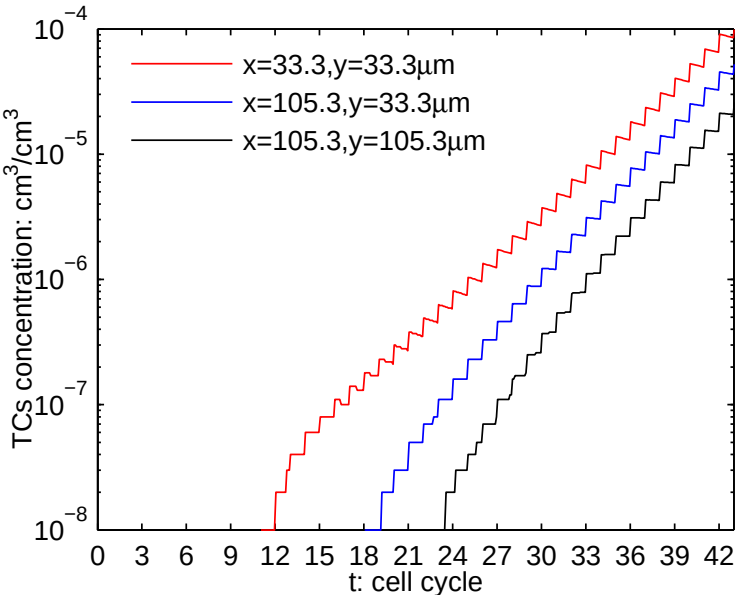

(a) case I (originating at the inlet region)

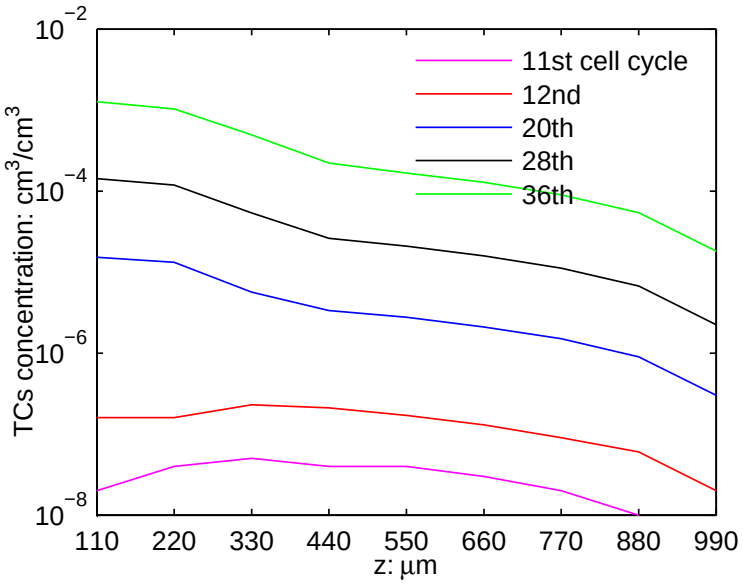

(b) case I, within the closest capillary

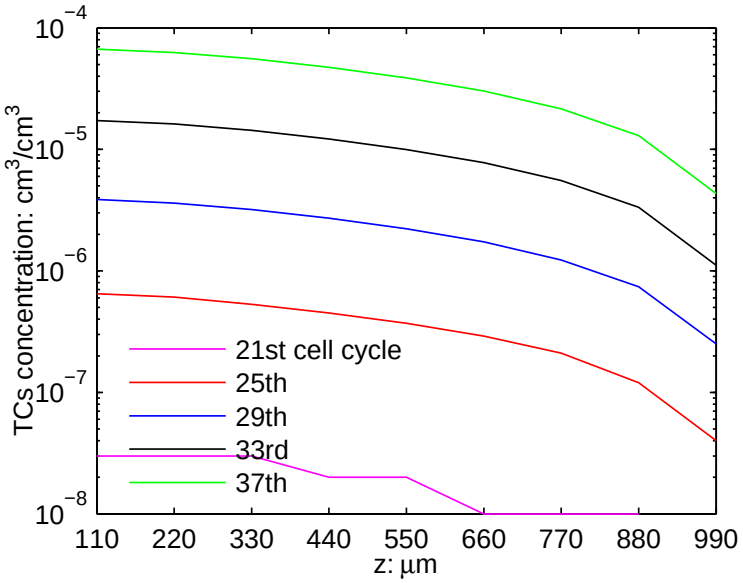

(c) case I, within the furthest capillary

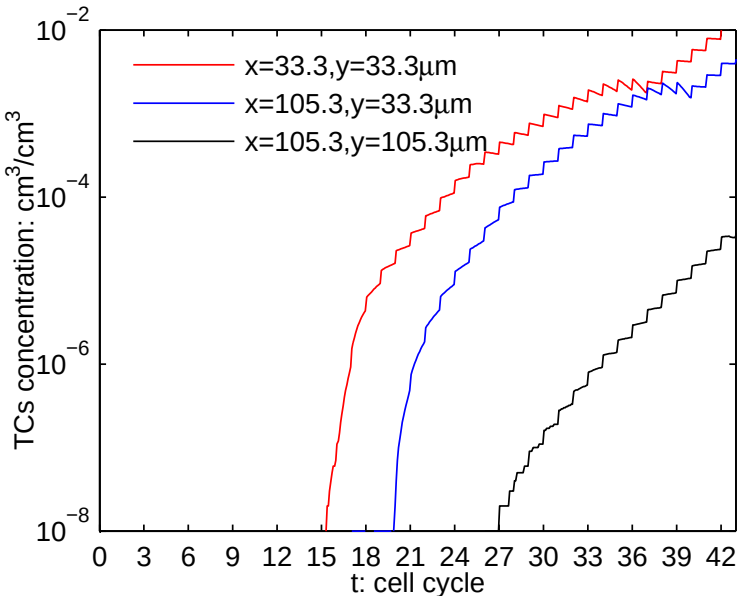

(d) case II (originating at the outlet region)

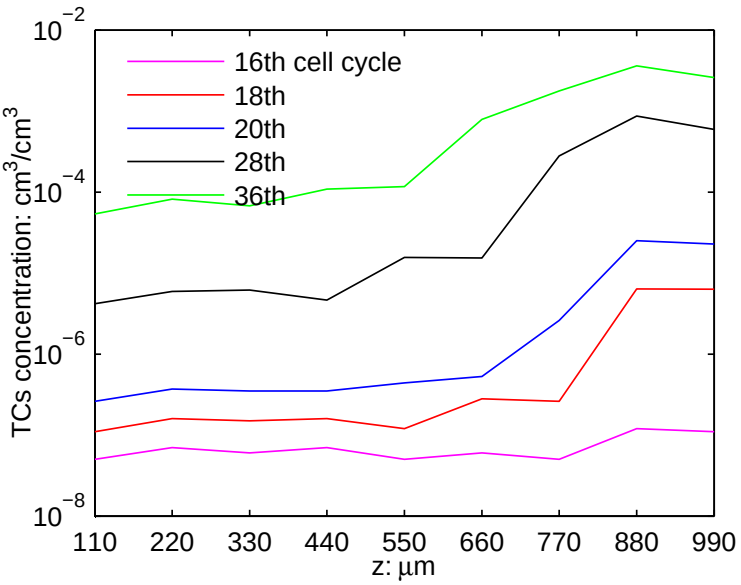

(e) case II, within the closest capillary

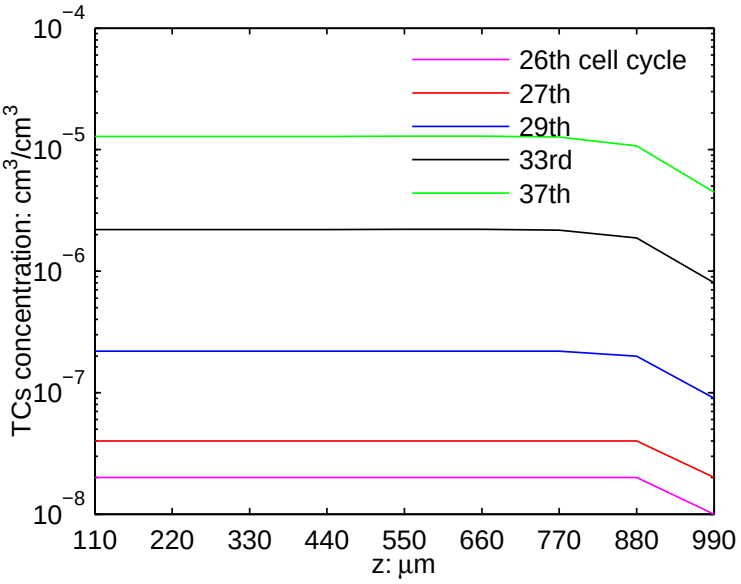

(f) case II, within the furthest capillary

Figure 3.9: An analysis of TC growth within the capillaries for (a)(c) case I, and (d)(f) case II. (a), (d): TC concentrations entering the blood over time, i.e. TC concentration at the outlet end of the three capillaries, where red (located at x=33.3-38.7,y=33.3-38.7µm) is closest to the primary site, blue (located at x=105.3-108, y=33.3-38.7µm) is further away from the primary site, and black (located at x=105.3-108,y=105.3-108µm) is furthest from the primary site. Furthermore, TC concentrations along the capillary direction are given at five different times, as shown in (b) and (e) for the closest capillary, and in (c) and (f) for the furthest capillary.

the growth of avascular tumors is limited because insufficient oxygen and nutrients are supplied with successive divisions of the TCs (Folkman 1971; Cai et al 2011), and, thereafter, the vascularization stage determines the pathophysiological characteristics of the tumor, including the invasiveness and the metastasis (Otrock et al 2007; Chung et al 2010; Weis and Cheresh 2011; Quail and Joyce 2013); considerable efforts in recent years have therefore been devoted to the development of various anti-angiogenic drugs and new anti-angiogenesis therapies, and many of these drugs and therapies have been clinically applied (Bergers and Hanahan 2008; Ribatti 2009; Ruoslahti et al 2010; Ziyad and Iruela-Arispe 2011; Carmeliet and Jain 2011). However, our numerical results indicate that these therapies are carried out at too late a stage for the treatments to have any major effects, even if the drugs could inhibit angiogenesis.

Additionally, we compare the TC concentrations along the capillary direction for case I (Fig.3.9(b),(c)) and case II (Fig.3.9(e),(f)), and those within the three capillaries at different distances from the primary tumor. The results indicate that: (a) for case I, the TCs enter into the blood circulation five cell cycles earlier than in case II, but for case II, the concentration of TCs entering the blood circulation is much higher than that of case I; (b) there is generally a difference of two orders of magnitude between the concentration in the inlet end and the concentration in the outlet end; (c) the TCs enter the capillary that is closest to the primary tumor about ten cell cycles earlier than they enter the most distant capillary, which is approximately 150μm from the primary tumor, and the TC concentration in the closest capillary is four orders of magnitude higher than that in the most distant capillary.

3.4.6 MDE concentrations over time and their diagnostic value

The results in Fig.3.10 show that from the initial time, the MDEs are transported much further along both the capillary direction and the direction from the primary tumor to the surrounding tissue than the TCs migrate. In the 9th cell cycle, the MDEs are diffused into the capillary with an average concentration of about 4×10^{-11}M, while the TCs have not yet entered the capillary, and at the 15th cell cycle, the average MDE concentration within the capillary increased to 4×10^{-10}M, while a small amount of TCs enter the capillary. Additionally, a comparison of the times at which the MDEs and the TCs enter the blood, as presented in Fig.3.11, indicates that there is a great difference between the time when the MDEs enter the blood circulation and the time when the TCs enter the blood circulation. In case I, the MDEs enter the blood circulation 12 cell cycles earlier than the TCs might have been examined, while for case II, the MDEs might

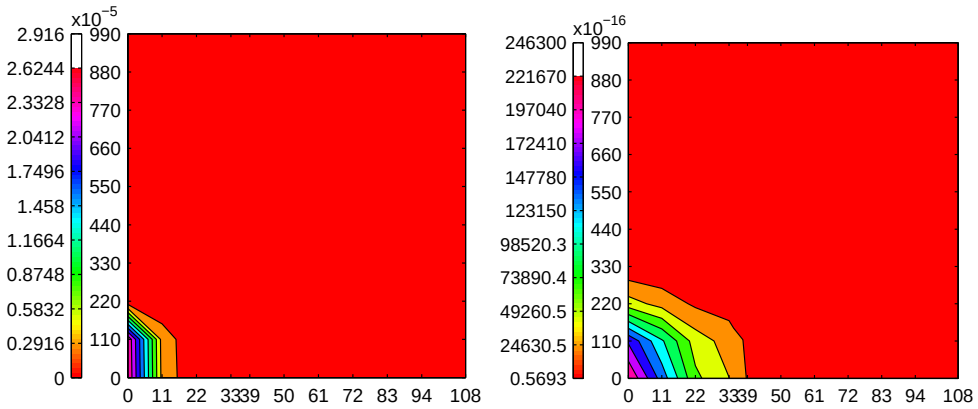

(a) x=0μm, 1st cell cycle

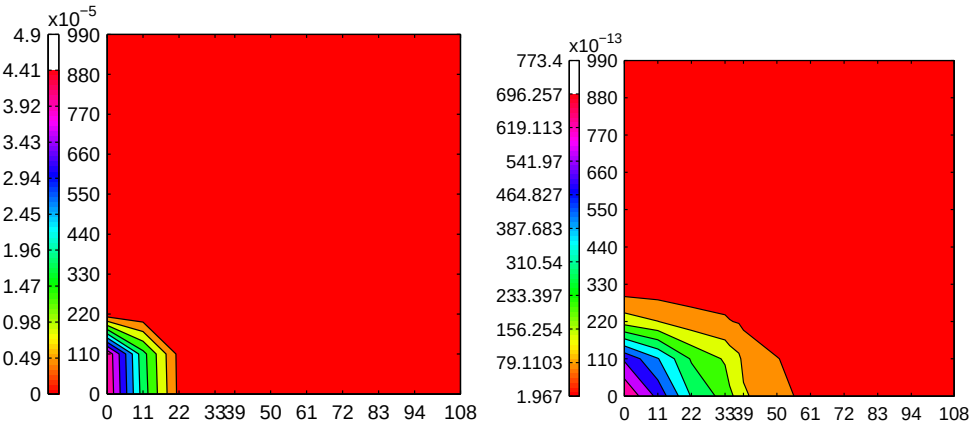

(b) x=0μm, 4th cell cycle

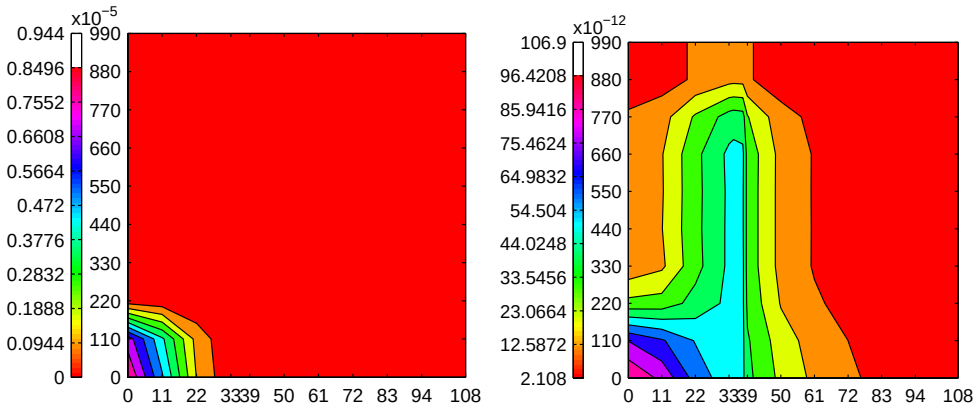

(c) x=33.3μm, 9th cell cycle

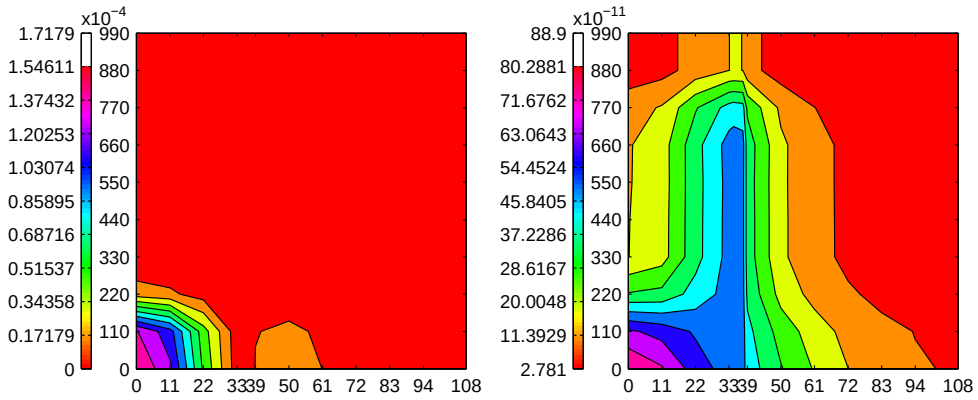

(d) x=33.3μm, 15th cell cycle

Figure 3.10: For case I, a comparison of TC growth and MDE transportation at four typical times, i.e. at the (a) 1st, (b) 4th, (c) 8th and (d) 15th cell cycles, where the TC concentration distributions are presented on the left sides of (a)(d) (in cm^3/cm^3), and those of the MDEs are presented on the right sides (in M). (a), (b): the distribution at fixed x=0μm; (c), (d): the distribution at fixed x=33.3μm. In (c) and (d), the grid of y=33-33.3, 38.7-39, 105-105.3 denotes the capillary wall, the grid of y=33.3-38.7, 105.3-108 denotes the capillary vessel, and the remaining region denotes the tissue.

have been examined in the blood 15 cell cycles earlier than the TCs; because MDEs grow very rapidly in the first few cell cycles, the MDEs have diffused into the pre-existing capillaries before the TCs begin to divide, and when the TCs begin to enter the blood circulation, the MDEs have increased to more than 10^{-12}M, which is 14 orders of magnitude higher than the MDE concentration at the initial time. The exponential fitting curves of the MDE concentrations, for which the values of the R-squares of these curves are all higher than 0.99, are also shown in Fig.3.11. The results above theoretically indicate that MDEs could be used as potential bio-markers because MDEs with their high concentrations could be examined in the blood much earlier than the TCs enter the blood circulation. This result agrees with many of the previous experimental studies, which have aimed to demonstrate and to estimate the role that MDEs can play in cancer diagnosis (Deakin and Chaplain 2013; Hadler-Olsen et al 2013; Zhang and Kim 2012; Kessenbrock et al 2010; Herszenyi et al 2012; Bourboulia and Stetler-Stevenson 2010; Eichelberg et al 2009), but also theoretically gives the development stage of the tumor (i.e. the cell cycle of the tumor) when the MDEs can be detected in blood, and provides a basis for estimation of the size of the solid tumor by examining the MDE concentration in the blood.

Additionally, the power functional relationship between the MDE concentrations entering the blood circulation and the volume of the solid tumor is shown, where the R-square values of the fitting curves are higher than 0.95. This could provide an important basis for early cancer diagnosis and tumor size estimation from the MDE concentration in the blood. Detection of an avascular tumor with a size of approximately 1-2mm^3 is very difficult, even when using many digital medical scanning techniques, such as computed tomography (CT) imaging and magnetic resonance (MR) imaging (Drukteinis et al 2013; Jun et al 2014); however, MDEs used as bio-markers would enable detection of the malignant tumor when it grows to within levels as small as 100μm.

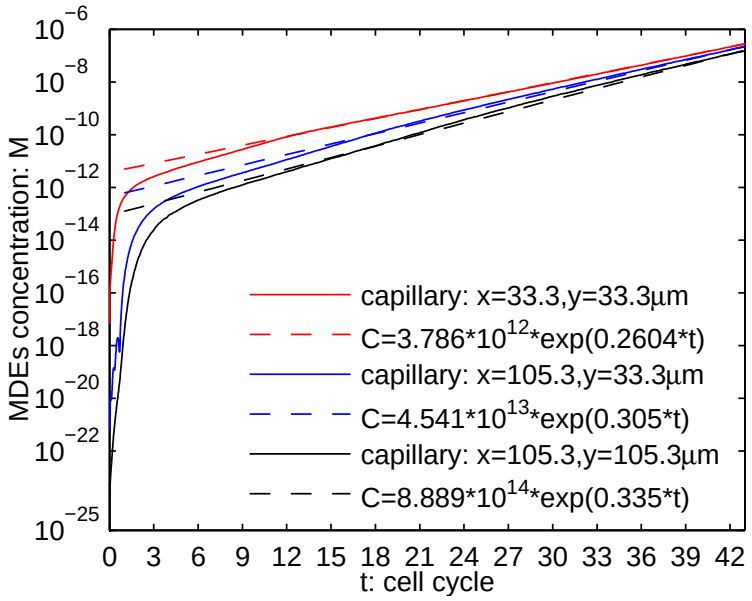

(a) case I (originating at the inlet region)

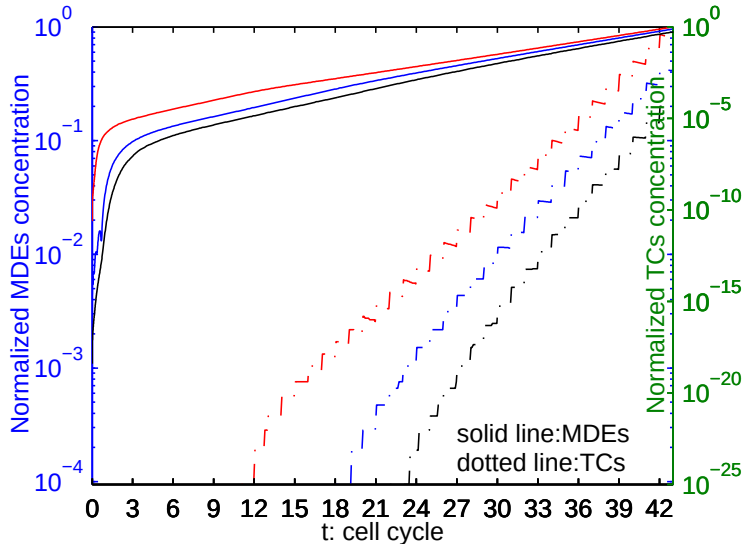

(b) case I (originating at the inlet region)

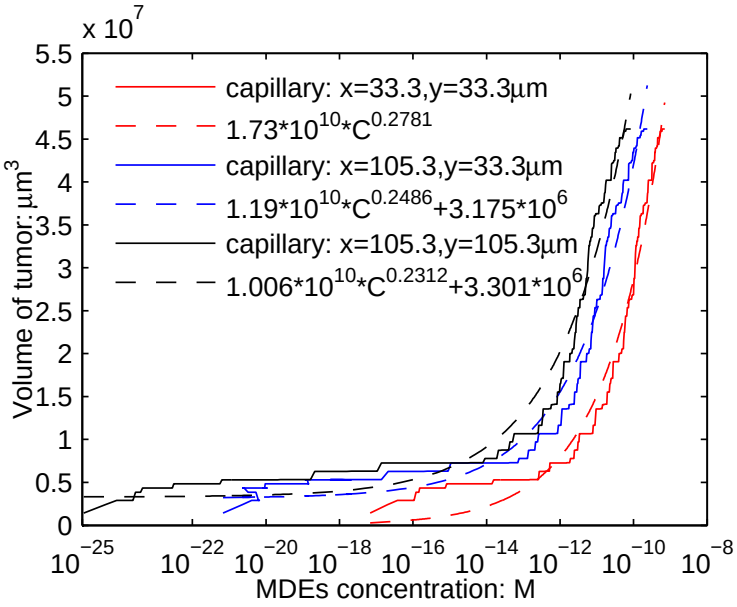

(c) case I, MDE concentration and volume of tumor

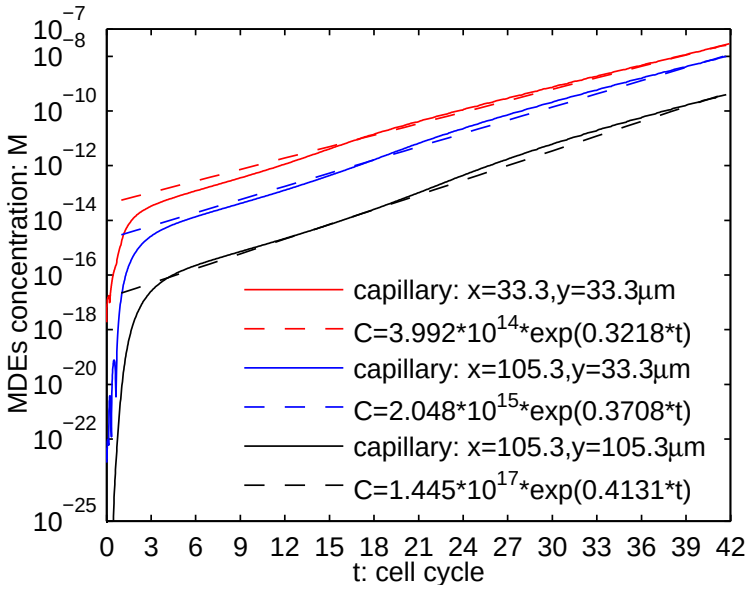

(d) case II (originating at the outlet region)

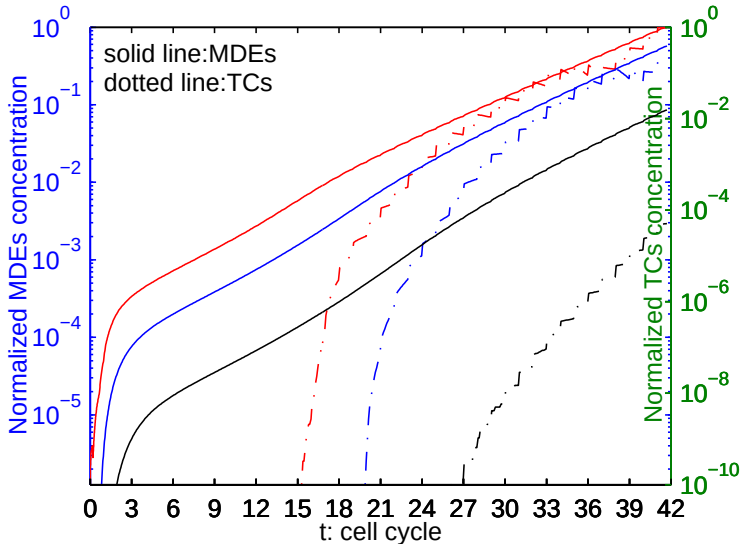

(e) case II (originating at the outlet region)

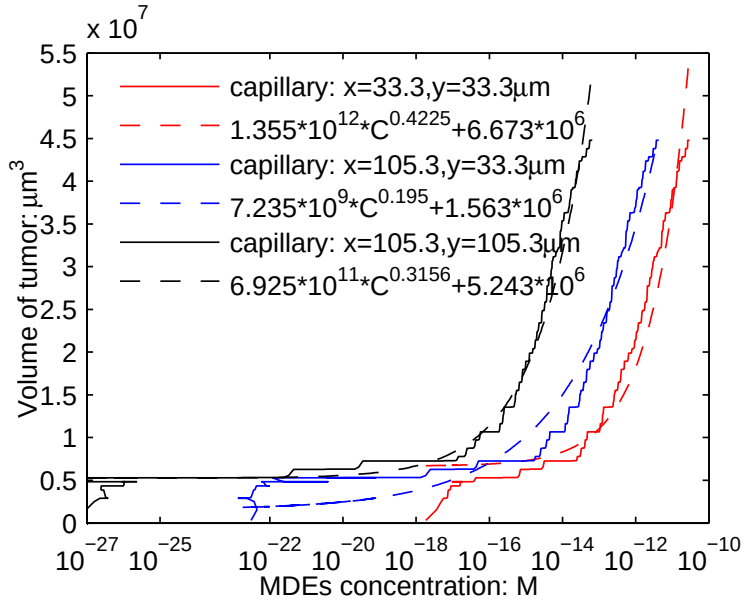

(f) case II, MDE concentration and volume of tumor

Figure 3.11: An analysis of MDE diffusion within the capillaries for (a)(c) case I and (d)(f) case II, where the red, blue and black curves correspond to the three capillaries in Fig.3.9. (a) MDE concentration entering the blood over time, i.e. concentration at the outlet end of the three capillaries over 42 cell cycles, where the corresponding fitting exponential curves are represented by the dotted lines; (b) a comparison of the times when the TCs and the MDEs enter the blood, where the horizontal axis represents the cell cycle of the TCs, and the vertical axis represents the normalized MDE concentration (using the left axis), and the normalized TC concentration (using the right axis); (c) the relationship between MDE concentration and the solid tumor volume, where the corresponding fitting power curves are represented by dotted lines. Corresponding figures for case II are presented in parts (d)(f).

3.5 Discussion

3.5.1 The effect of oxygen supplement on tumor growth

Most previous mathematical models have employed the reaction-diffusion equation to govern the process of oxygen transported to TCs. In these models the oxygen is simply assumed to be produced by a constant production or source coefficient, and is transported by pure molecular diffusion within healthy tissue (Anderson 2005;Gerischa and Chaplain 2008;Kiran et al 2009;Cai et al 2011;Mahmood et al 2011). Based on this simplification of a uniform oxygen supply from homogenous tissue, the oxygen distribution is entirely determined by the oxygen consumption coefficient of the cells. However, this assumption is not sufficient to describe the oxygen distribution at a micro level, which could lead to a necrotic core of tumor that would necessarily begin from the tumor center because of a high TC concentration. Some mathematical models consider the effect of the initial existing capillaries on oxygen supply, and have incorporated an organized initial vasculature, comprising arteries, veins and capillaries (Welter et al 2009;Welter and Rieger 2010). However, these neglect variations of the oxygen level within the vessels, assuming that these variations are small over the length of an oxygen-releasing capillary. Another similar simulation (Scium et al 2013) has been applied to the case where TCs grow in proximity to two otherwise healthy blood capillaries that are the only source of oxygen, and the results clearly showed that necrosis occurs in parts of the tumor distant from the capillary near where the tumor originated. This differs from Anderson (Anderson 2005), who also prove that the presence of capillary vessels has an important impact on tumor development and on their spatial configuration (Astanin and Preziosi 2009). However, this assumption of a constant level of oxygen within the capillaries remains inadequate when modeling oxygen transport in a micro-environment, because the difference in blood oxygen partial pressure over the length of the capillary, from the arteriole end to the venule end, is approximately 60 mmHg (Hall 2010) and the difference in simulation results for models with constant and varying hematocrit have been proven on a micro scale (Welter et al 2009).

Comparing our model with the above models, we see some improvements in the consideration of oxygen transportation:

- The variation of blood oxygen concentration within capillaries is incorporated: blood oxygen partial pressure ranges from 95 mmHg (at the inlet end) to 40 mmHg (at the outlet end) (Hall 2010).

- The oxygen diffusion coefficients within the capillary, at the capillary wall and within the tissue are different.
- The convection-diffusion of oxygen is not neglected; in previous work we compared the simulation results for an oxygen transport model with coupled convection-diffusion and without coupled convection-diffusion, and found differences on a micro scale (Zhao et al. unpublished). This effect has been neglected in most previous models (Jones and Chapman 2012).
- The variation of the oxygen diffusion coefficient related to TC concentration is incorporated, as we suggest a fast growth rate of TCs will occupy space in the tissue to vary the porosity of porous media, partly blocking the transport pathway for oxygen. Many previous models simply assume the diffusion coefficient of oxygen is constant (Cai et al 2011;Welter and Rieger 2010).

These improvements make the simulation of oxygen supply closer to reality. Based on the simulation results a novel finding is revealed, that a necrotic core would not necessarily occur first at the tumor center (detailed in sect.3.4.3). These quantitative results contribute to an understanding of the progression of an avascular tumor, and to the development of novel methods for the early detection of cancer and its treatment.

3.5.2 The effect of tumor micro-environment on TCs migration

Previously, Macklin presented a model for solid tumor growth that incorporated features of the tumor micro-environment to examine the effect of the micro-environment on tumor growth (Macklin and Lowengrub 2007). However, the microvessel structure was not incorporated, which is not helpful for gaining insight into the phenomenon of tumor growth at an avascular phase. A multicellular tumor spheroid within healthy tissue is often used to study tumor growth where the results only show that the further the tumor is from its center, the more slowly the tumor grows (Anderson 2005;Scium et al 2013). The simulation of a solid tumor in two capillaries investigated the effects of the vasculature on tumor evolution (Scium et al 2013). However, this model only considered the capillaries as an oxygen source, and paid little attention to the differences between the transport of chemical factors in the capillary, the capillary wall and the tissue (Welter et al 2009). Their results suggested that a tumor further from capillaries becomes necrotic earlier.

In the model we present here, we simulate a solid tumor growth in a porous media composed of the capillary, the capillary wall and the tissue, and in addition heterogene-

ity between these three media is considered. Based on this, we found that a tumor further from capillaries grows faster, as we saw in sect.3.4.4 and Fig.3.7. The main reasons for this are discussed below:

- Invasion for TCs surrounding capillaries is more difficult than for those within the tissue.
- Compared with conditions within the tissue, the seepage velocity of fluid surrounding capillaries is slower, convection-diffusion of MDEs becomes lower. Correspondingly the ECM concentration becomes higher and the migration of TCs becomes slower.
- The molecular diffusion of MDEs is lower surrounding the capillaries than within the tissue.

The results indicate that the presence of an initial micro-vessel structure plays an essential role: the evolution of an avascular tumor should not simply be described as an invasion of the area up to 1-2 mm from the tumor center, but should be a more complicated and systemic process that is closely related to the micro-environment that the tumor grows or migrates in.

3.6 Conclusion

The coupled mathematical model for an avascular solid tumor growth has been developed based on porous media mechanics, where the innovative aspects of the present model focus on:

- the convection-diffusion of oxygen,
- the convection-diffusion of MDEs,
- the effect of the ECM on tumor growth, which is directly coupled to the motility coefficient of TCs,
- the permeability coefficient of fluid and the diffusion coefficient of oxygen, which is related to the TC concentration.

Two cases are simulated, where the tumor originates at the inlet region and at the outlet region, and important findings include the facts that:

- For a solid tumor originating at the inlet region, necrosis occurs at the outlet region because of a low supply of oxygen; for a solid tumor originating at the outlet region, necrosis occurs at the primary site because of overconsumption of oxygen.
- For a tumor originating at the inlet end, when TC concentration in the primary site increases to more than $0.1\text{cm}^3/\text{cm}^3$, necrosis begins to occur at the outlet region; when TC concentration in the primary site increases to more than $0.28\text{cm}^3/\text{cm}^3$, necrosis begins at the primary tumor. In the case of a tumor originating at the outlet end, when TC concentration increases to more than $0.24\text{cm}^3/\text{cm}^3$, necrosis occurs first in the primary tumor.
- A tumor further from the adjacent capillary grows faster than a tumor close to the adjacent capillary.

The approach and results presented in this paper could provide the foundation for engendering novel therapeutic strategies and treatment optimization to improve the prognosis of patients with avascular tumors.

In the further study of MDEs as bio-markers for detection of early cancer, the numerical results based on the coupled mathematical model indicate four most important findings:

- The TCs had entered the blood circulation through the pre-existing capillaries long before the cells began to necrotize and the vascular networks were remodeled.
- In case I, the MDEs might be examined in the blood 12 cell cycles earlier than the TCs might be examined, and in case II, the MDEs might be examined in the blood 15 cell cycles earlier than the TCs.
- The development stage of the solid tumor and its size could both be estimated by measuring the MDE concentration in the blood, based on the exponential relationship of the MDE concentration over time and the power relationship between the MDE concentration and the volume of the tumor.
- MDEs acting as bio-markers would help in the diagnosis of a malignant tumor as small as 100μm.

This theoretical model led to new ideas for cancer treatments based on the development of drugs that could inhibit the secretion or diffusion of MDEs, which would then inhibit the degradation of the ECM. Incorporation of the governing equations of the MDE-inhibiting drugs into this model in the future will be helpful in determining the prognosis of these treatments.

Chapter 4.

General conclusion

This chapter will give a summary of the results acquired in the whole work, accompanied by some suggestions for future work.

This present dissertation mainly sought to disentangle the effect of convection-diffusion on oxygen transport at this level of the microcirculation, and then stimulus the entire process of a solid tumor growing in its very early stage, i.e. avascular phase for a solid tumor, by using a developed mathematical coupled model for oxygen transport in microcirculation and a mathematical coupled model for avascular tumor growth.

At first, this present dissertation aims to investigate a very significant and fundamental topic involved in the microcirculation, that is studying the distribution of oxygen concentration at this level. For this, we numerically calculate an entire process of oxygen transport, by developing a 3D coupled solid deformation–fluid seepage–convection and diffusion porous media model, which newly takes account of volumetric deformation of both capillary and tissue resulting from capillary fluctuation, and couples the deformations into seepage, then the seepage coupled the deformation affects on convection-diffusion of oxygen. Specially, we quantitatively examine how solid deformation, fluid seepage and convection-diffusion affect the transport of oxygen, and have some important findings:

- Solid deformation is more significant in the middle of capillary, where the maximum value of volumetric deformation reaches about 0.5%;
- Though solid deformation has a small impact on seepage, it can help the tissue fluid to flow more uniformly, also can help the oxygen to be transported more uniformly, eventually affects on the distribution oxygen concentration by 0.1% 0.5%.
- The change in pore pressure distribution within the tissue near arteriole end and near venule end of capillary is several times larger than within the tissue surrounding the middle of capillary.
- Convection-diffusion given by coupled deformation and seepage has a 16% maximum, 3% average increase in oxygen concentration, compared to pure diffusion.

Its more significant role is to allows oxygen to be transported more evenly, especially to where is away from capillary.

- Convection-diffusion has a greater effect in the middle of capillary than that near the ends of capillary. Also, larger values of permeability coefficient, or smaller values of the diffusion coefficient produce a more obvious effect on oxygen transport.

Thus, the numerical results from this more comprehensive theoretical model indicate that the convection-diffusion of oxygen transport should be necessary to be considered in the relevant studies, its important role of allowing oxygen to be transported more uniformly should be paid more attention and be studied further.

Second, based on the more comprehensive theoretical coupled model for oxygen transport, and that an important effect of convection-diffusion on oxygen transport has been demonstrated, a further study on the growth of avascular tumor was carried on. The coupled mathematical model for an avascular solid tumor growth has been developed based on porous media mechanics, where the innovative aspects of the present model focus on:

- the convection-diffusion of oxygen,
- the convection-diffusion of MDEs,
- the effect of the ECM on tumor growth, which is directly coupled to the motility coefficient of TCs,
- the permeability coefficient of fluid and the diffusion coefficient of oxygen, which is related to the TC concentration.

Two cases are simulated, where the tumor originates at the inlet region and at the outlet region, and important findings include the facts that:

- For a solid tumor originating at the inlet region, necrosis occurs at the outlet region because of a low supply of oxygen; for a solid tumor originating at the outlet region, necrosis occurs at the primary site because of overconsumption of oxygen.
- For a tumor originating at the inlet end, when TC concentration in the primary site increases to more than $0.1\text{cm}^3/\text{cm}^3$, necrosis begins to occur at the outlet region; when TC concentration in the primary site increases to more than $0.28\text{cm}^3/\text{cm}^3$,

necrosis begins at the primary tumor. In the case of a tumor originating at the outlet end, when TC concentration increases to more than $0.24 cm^3/cm^3$, necrosis occurs first in the primary tumor.

- A tumor further from the adjacent capillary grows faster than a tumor close to the adjacent capillary.

The approach and results presented in this paper could provide the foundation for engendering novel therapeutic strategies and treatment optimization to improve the prognosis of patients with avascular tumors.

In addition, we also use this mathematical model for the growth of avascular tumor to examine the clinic value of MDEs for early cancer detection. The numerical results based on the coupled mathematical model indicate four most important findings:

- The TCs had entered the blood circulation through the pre-existing capillaries long before the cells began to necrotize and the vascular networks were remodeled.

- In case I, the MDEs might be examined in the blood 12 cell cycles earlier than the TCs might be examined, and in case II, the MDEs might be examined in the blood 15 cell cycles earlier than the TCs.

- The development stage of the solid tumor and its size could both be estimated by measuring the MDE concentration in the blood, based on the exponential relationship of the MDE concentration over time and the power relationship between the MDE concentration and the volume of the tumor.

- MDEs acting as bio-markers would help in the diagnosis of a malignant tumor as small as 100μm.

This theoretical model led to new ideas for cancer treatments based on the development of drugs that could inhibit the secretion or diffusion of MDEs, which would then inhibit the degradation of the ECM. Incorporation of the governing equations of the MDE-inhibiting drugs into this model in the future will be helpful in determining the prognosis of these treatments.

References

Allen RD, Allen NS (1978) Cytoplasmic streaming in amoeboid movement. Annu Rev Biomed Eng 7:469–495

Anderson ARA (2005) A hybrid mathematical model of solid tumor invasion: the importance of cell adhesion. Math Med Biol 22(2):163–186

Astanin S, Preziosi L (2009) Mathematical modelling of the warburg effect in tumour cords. J Theor Biol 258:578–90

Aumailley M, Timpl R (1986) Attachment of cells to basement membrane collagen type iv. J Cell Biol 103:15691575

Baker EA, Leaper DJ (2003) The plasminogen activator and matrix metalloproteinase systems in colorectal cancer: relationship to tumour pathology. Eur J Cancer 39(7):981–8

Bear J (1988) Dynamics of Fluids in Porous Media. Elsevier, New York

Bergers G, Hanahan D (2008) Modes of resistance to anti-angiogenic therapy. Nat Rev Cancer 8(8):592–603

Bird RB, Stewart WE, Lightfoot EN (2002) Transport Phenomena. John Wiley & Sons, Inc., New York

Biro GP, Anderson PJ, Curtis SE, Cain SM (1991) Stroma-free hemoglobin: its presence in plasma does not improve oxygen supply to the resting hindlimb vascular bed of hemodiluted dogs. Can J Physiol Pharmacol 69(11):1656–1662

Bissell JM, Radisky D (2001) Putting tumours in context. Nature Reviews Cancer 1(1):46–54

Bogenrieder T, Herlyn M (2003) Axis of evil: Molecular mechanisms of cancer metastasis. Oncogene 22:65246653

Bourboulia D, Stetler-Stevenson WG (2010) Matrix metalloproteinases (mmps) and tissue inhibitors of metalloproteinases (timps): positive and negative regulators intumor cell adhesion. Semin Cancer Biol 20(3):161–168

Briozzo P, Morisset M, Capony F, Rougeot C, Rochefort H (1988) In vitro degradation of extracellular matrix with mr 52000 cathepsin d secreted by breast cancer cells. Cancer Res 48:3688–3692

Burridge K, Chrzanowska-Wodnicka M (1996) Ffocal adhesions, contractility, and signaling. Annu Rev Cell Dev 12:463–518

Byrne H, Preziosi L (2003) Modelling solid tumour growth using the theory of mixtures. Math Med Biol 20(4):341–66

Cai Y, Xu S, Wu J, Long Q (2011) Coupled modelling of tumour angiogenesis, tumour growth and blood perfusion. J Theor Biol 279(1):90–101

Campbell NE, Kellenberger L, Greenaway J, AMoorehead R, Linnerth-Petrik NM, Petrik J (2010) Extracellular matrix proteins and tumor angiogenesis. Journal of Oncology 2010:586–905

Carmeliet P, Jain RK (2011) Molecular mechanisms and clinical applications of angiogenesis. Nature 473(7347):298–307

Caro CG, Pedley TJ, Schroter RC, Seed WA (2012) The mechanics of the circulation, 2nd edn. Oxford Medical Publications, Oxford University Press, Cambridge

Casciari JJ, Sotirchos SV, Sutherland RM (1992) Variation in tumour cell growth rates and metabolism with oxygen-concentration, glucose-concentration and extracellar ph. J Cell Physiol 151(2):386–394

Chapman SJ, RJ RJS, Jawad R (2008) Multiscale modeling of fluid transport in tumors. Bull Math Biol 70(8):2334–2357

Charles M, Rubin MD (1998) The Genetic Basis of Human Cancer. McGraw-Hill, New York

Chertow GM, Paltiel AD, Owen WF, Lazarus JM (1996) Cost-effectiveness of cancer screening in end-stage renal disease. Archives of Internal Medicine 156(12):1345–1350

Choe G, Park JK, Jouben-Steele L, Kremen TJ, Liau LM, Vinters HV, Cloughesy TF, Mischel PS (2002) Active matrix metalloproteinase 9 expression is associated with primary glioblastoma subtype. Clin Cancer Res 8(9):2894–901

Chung AS, Lee J, Ferrara N (2010) Targeting the tumour vasculature: insights from physiological angiogenesis. Nat Rev Cancer 10(7):505–14

Condeelis J, Segall JE (2003) Intravital imaging of cell movement in tumours. Nat Rev Cancer 3:921–30

Condeelis J, Jones J, Segall JE (1992) Chemotaxis of metastatic tumor cells: clues to mechanisms from the dictyostelium paradigm. Cancer Metastasis Rev 11:55–68

Deakin NE, Chaplain MAJ (2013) Mathematical modeling of cancer invasion: The role of membrane-bound matrix metalloproteinases. Front Oncol 3(70)

Drukteinis JS, Mooney BP, Flowers CI, Gatenby RA (2013) Beyond mammography: New frontiers in breast cancer screening. The American Journal of Medicine 126(6):472–479

Edwards D, Brenner H (1993) Macrotransport Processes, 1st edn. Butterworth-Heinemann, Stoneham, MA

Eichelberg C, Junker K, Ljungberg B, Moch H (2009) Diagnostic and prognostic molecular markers for renal cell carcinoma: a critical appraisal of the current state of research and clinical applicability. Eur Urol 55(4):851–63

Eissa S, Swellam M, el Mosallamy H, Mourad MS, Hamdy N, Kamel K, Zaglol AS, Khafagy MM, el Ahmady O (2003) Diagnostic value of urinary molecular markers in bladder cancer. Anticancer Res 23:4347–4355

Federspiel WJ, Popel AS (1986) A theoretical analysis of the effect of the particulate nature of blood on oxygen release in capillaries. Microvasc Res 32(2):164–189

Fingleton B (2003) Matrix metalloproteinase inhibitors for cancer therapy:the current situation and future prospects. Expert Opin Ther Targets 7(3):385–97

Folkman J (1971) Tumor angiogenesis: therapeutic implications. N Engl J Med 285(21):1182–6

Frieboes HB, Jin F, Chuanga YL, Wisec SM, Lowengrubb JS, Cristini V (2010) Three dimensional multispecies nonlinear tumor growth-ii: Tumor invasion and angiogenesis. J Theor Biol 264:1254–1278

Friedl P, Wolf K (2003) Tumour-cell invasion and migration: Diversity and escape mechanisms. Nat Rev Cancer 3:362–374

Gerhards S, Jung K, Koenig F, Daniltchenko D, Hauptmann S, Schnorr D, Loening SA (2001) Excretion of matrix metalloproteinases 2 and 9 in urine is associated with a high stage and grade of bladder carcinoma. Urology 57:675–679

Gerischa A, Chaplain MAJ (2008) Mathematical modelling of cancer cell invasion of tissue: Local and non-local models and the effect of adhesion. Journal of Theoretical Biology 250:684704

Gohji K, Hirano H, Okamoto M, Kitazawa S, Toyoshima M, Dong J, Katsuoka Y, Nakajima M (2001) Expression of three extracellular matrix degradative enzymes in bladder cancer. Int J Cancer 95(5):295–301

Goldman D (2008) Theoretical models of microvascular oxygen transport to tissue. J microcirc 15(8):795–811

Goldman D, Popel AS (2000) A computational study of the effect of capillary network anastomoses and tortuosity on oxygen transport. J Theor Biol 206(2):181–194

Goldman D, Bateman RM, Ellis CG (2004) Effect of sepsis on skeletal muscle oxygen consumption and tissue oxygenation: interpreting capillary oxygen transport data using a mathematical model. Am J Physiol Heart Circ Physiol 287(6):2535–2544

Greene AS, Tonellato PJ, Zhang Z, Lombard JH, A W Cowley J (1992) Effect of microvascular rarefaction on tissue oxygen delivery in hypertension. Am J Physiol 262(5):1486–1493

Grinberg O, Novozhilov B, Grinberg S, Friedman B, Swartz HM (2005) Axial oxygen diffusion in the korgh model: modifications to account for myocardial oxygen tension in isolated perfused rat hearts measured by fpr oximetry. Adv Exp Med Biol 566:127–134

Groebe K (1990) A versatile model of steady state O_2 supply to tissue. application to skeletal muscle. J Biophys 57(3):485–498

Hadler-Olsen E, Winberg JO, Uhlin-Hansen L (2013) Matrix metalloproteinases in cancer: their value as diagnostic and prognostic markers and therapeutic targets. Tumour Biol 34(4):2041–51

Hall JE (2010) Guyton and Hall Textbook of Medical Physiology, 12th edn. Saunders, chapter 40

Hartridge H, Roughton FJW (1923) The measurement of the rates of oxidation and reduction of hmoglobin. Proc R Soc Lond B Biol Sci 94:336–367

He Y, Himeno R (2012) Finite element analysis on fluid filtration in system of permeable curved capillary and tissue. J Mech Med Biol 12(4):1250,077

Hellums JD, Nair PK, Huang NS, Oshima N (1996) Simulation of intraluminal gas transport in the microcirculation. Ann Biomed Eng 24(1):1–24

Herszenyi L, Hritz I, Lakatos G, Varga MZ, Tulassay Z (2012) The behavior and matrix metalloproteinases and their inhibitors in colorectal cancer. Int J Mol Sci 13(10):13,240–63

Hoofd L, Degens H (2009) The influence of flow redistribution on working rat muscle oxygenation. Adv Exp Med Biol 645:55–60

Hsu R, Secomb TW (1989) A greens function method for analysis of oxygen delivery to tissue by microvascular networks. Math Biosci 96(1):61–78

Hurst N, Stocken D, Wilson S, Keh C, Wakelam M, Ismail T (2007) Elevated serum matrix metalloproteinase 9 concentration predicts the presence of colorectal neoplasia in symptomatic patients. British Journal of Cancer 97(7):971–977

Hynes RO (2009) The extracellular matrix: Not just pretty fibrils. science 326:1216–1219

Jain RK, Stylianopoulos T (2010) Delivering nanomedicine to solid tumors. Nat Rev Clin Oncol 5(11):653–64

Jessen LR, Petersen OW, Koteliansky V, Bissell MJ (1995) The origin of the myofibroblasts in breast cancer. recapitulation of tumor environment in culture unravels diversity and implicates converted fibroblasts and recruited smooth muscle cells. J Clin Invest 95:859–873

Jlinoj J, Herva R, Korpela M, Hyhty M, Hujanen TT (2000) Matrix metalloproteinase 2 (mmp-2) immunoreactive protein is associated with poor grade and survival in brain neoplasms. J Neurooncol 46(1):81–90

Jones GW, Chapman SJ (2012) Modeling growth in biological materials. SIAM Rev 54:52118

Jumper C, Cobos E, Lox C (2004) Determination of the serum matrix metalloproteinase-9 (mmp-9) and tissue inhibitor of matrix metalloproteinase-1 (timp-1) in patients with either advanced small-cell lung cancer or non-small-cell lung cancer prior to treatment. Respir Med 98(2):173–7

Jun S, Jipei L, Maria G, HongBin F, Ling C, Sanford S, Feng J (2014) Analysis of micrornas in sputum to improve computed tomography for lung cancer diagnosis. Journal of Thoracic Oncology 9(1):33–40

Kessenbrock K, Plaks V, Werb Z (2010) Matrix metalloproteinases: Regulators of the tumor microenvironment. Cell 141(1):52–67

KF K, van Till JW, MA B, de Reuver PR, ID T, GJ O, FJ TK, OR B, van Gulik TM, DJ G, HC C (2007) Evaluation of matrix metalloproteinase 7 in plasma and pancreatic juice as a biomarker for pancreatic cancer. Cancer Epidemiol Biomarkers Prev 16(5):886–91

Kiran KL, Jayachandran D, Lakshminarayanan S (2009) Mathematical modelling of avascular tumour growth based on diffusion of nutrients and its validation. The Canadian Journal of Chemical Engineering 87:732–740

Klitzman B, Popel AS, Duling BR (1983) Oxygen transport in resting and contracting hamster cremaster muscles: experimental and theoretical microvascular studies. Microvasc Res 25(1):108–131

Ko M, Ediger D, Budak F, Karada M, Oral HB, Uzaslan E, Ege E, Gz RO (2006) Matrix metalloproteinase-9 (mmp-9) elevated in serum but not in bronchial lavage fluid in patients with lung cancer. Tumori 92(2):149–54

Krogh A (1919a) The number and distribution of capillaries in muscles with calculations of the oxygen pressure head necessary for supplying the tissue. J Physiol 52(6):409–415

Krogh A (1919b) The supply of oxygen to the tissues and the regulation of the capillary circulation. J Physiol 52(6):457–474

Lagerlund TD, Low PA (1991) Axial diffusion and mchaelis-menten kinetics in oxygen delivery in rat peripheral nerve. Am J Physiol 260(2):430–440

Lagerlund TD, Low PA (1993) Mathematical modeling of time-dependent oxygen transport in rat peripheral nerve. Comp Biol Med 23(1):29–47

Landis EM, Pappenheimer JR (1963) Exchange of substances through capillary walls. In: Hamilton WF, Dow P (eds) Handbook of Physiology: Circulation, vol 2, 1st edn, Am. Physiol. Soc., Washington, DC, pp 961–1034

Langenskild M, Holmdahl L, Falk P, Ivarsson ML (2005) Increased plasma mmp-2 protein expression in lymph node-positive patients with colorectal cancer. Int J Colorectal Dis 20(3):245–52

Lawrence JA, Steeg PS (1996) Mechanisms of tumour invasion and metastasis. World J Urol 15:124–130

Lei XX, Wu WY, Wen GB, Chen JG (1998) Mass transfer in solid tumors (1) fluid dynamics. Appl Math Mech 19(11):1025–1032

Lengauer C, Kinzler KW, Vogelstein B (1998) Genetic instabilities in human cancers. Nature 396:643–649

Liang G, Zhao Y (2005) A mathematical model for solid liquid and mass transfer coupling and numerical simulation for hydraulic fracture in rock salt. Progress in natural Science 15(8):742–748

Lin PC, Kreutzer U, Jue T (2007) Anisotropy and temperature dependence of myoglobin translational diffusion in myocardium: implication for oxygen transport and cellular architecture. J Biophys 92(7):2608–2620

Lina EY, Nguyena AV, Russellb RG, Pollarda JW (2001) Colony-stimulating factor 1 promotes progression of mammary tumors to malignancy. J Exp Med 193(6):727–740

Liotta J, Rao CN, Barsky SH (1983) Tomour invasion and the extracellular matrix. Lab Invest 49:636–649

Liotta LA, Tryggvason K, Garbisa S, Hart I, Foltz CM, Shafie S (1980) Metastatic potential correlates with enzymatic degradation of basement membrane collagen. Nature 284(6):67–68

Liu G, Gabhann FM, Popel AS (2012) Effect of fiber type and size on the heterogeneity of oxygen distribution in exercising skeletal muscle. PLoS ONE 7(9):e44,375

Macklin P, Lowengrub J (2007) Nonlinear simulation of the effect of microenvironment on tumor growth. J Theor Biol 245(4):677–704

Mahmood MS, Mahmood S, Dobrota D (2011) Formulation and numerical simulations of a continuum model of avascular tumor growth. Math Biosci 231:159–171

Matrisian LM (1992) The matrix-degrading metalloproteinases. BioEssays 14:455–463

Maurel J, Nadal C, Garcia-Albeniz X, Gallego R, Carcereny E, Almendro V, Mrmol M, Gallardo E, Aug JM, Longarn R, Martnez-Fernandez A, Molina R, Castells A, Gascn P (2007) Serum matrix metalloproteinase 7 levels identifies poor prognosis advanced colorectal cancer patients. Int J Cancer 121(5):1066–71

McGuire BJ, Secomb TW (2001) A theoretical model for oxygen transport in skeletal muscle under conditions of high oxygen demand. J Appl Physiol 91(5):2255–2265

Michel CC (1984) Fluid movements through capillary walls. In: Renkin EM, Michel CC, Geiger SR (eds) Handbook of Physiology: The cardiovascular system. Microcirculation, vol IV, 1st edn, American Physiological Society, Bethesda,MD, pp 375–410

Michor F, Nowak MA, Frank SA, Iwasa Y (2003) Stochastic elimination of cancer cells. Proc Roy Soc Lond B Biol Sci 207:2017–2024

Michor F, Iwasa Y, Nowak MA (2004) Dynamics of cancer progression. Nature Reviews Cancer 4:197–205

Middleman S (1972) Transport phenomena in the cardiovascular system, Wiley-Interscience, New York, pp 116–140

Mignatti P, Rifkin DB (1993) Biology and biochemistry of proteinases in tumor invasion. Physiol Rev 73:161–95

Mikelic A, Primicerio M (2006) A diffusion-consumption problem for oxygen in a living tissue perfused by capillaries. Nonlinear Differ Equ Appl 13(3):349–367

Miller CJ, S KB, R KA, C PP, Jian-Lun X, G BS, Richard F, L RT (2009) Cumulative incidence of false-positive results in repeated, multimodal cancer screening. Annals of Family Medicine 7(3):212–22

Mitsiades N, Yu W, Poulaki V, Tsokos M, Stamenkovic I (2001) Matrix metalloproteinase-7-mediated cleavage of fas ligand protects tumor cells from chemotherapeutic drug cytotoxicity. Cancer Res 61:577–581

Morgia G, Falsaperla M, Malaponte G, Madonia M, Indelicato M, Travali S, Mazzarino MC (2005) Matrix metalloproteinases as diagnostic (mmp-13) and prognostic (mmp-2, mmp-9) markers of prostate cancer. Urol Res 33(1):44–50

Morsi Y, Kogure M, Umezu M (1999) Relative blood damage index of the jellyfish valve and the bjork-shiley tilting-disk valve. Journal of Artificial Organs 2(2):163–169

Moschandreou TE, Ellis CG, Goldman D (2011) Influence of tissue metabolism and capillary oxygen supply on arteriolar oxygen transport: a computational model. Math Biosci 232(1):1–10

Moses MA, Wiederschain D, Loughlin KR, Zurakowski D, Lamb CC, Freeman MR (1998) Increased incidence of matrix metalloproteinases in urine of cancer patients. Cancer Res 58(7):1395–9

Mroczko B, Lukaszewicz-Zajac M, Wereszczynska-Siemiatkowska U, Groblewska M, Gryko M, Kedra B, Jurkowska G, Szmitkowski M (2009) Clinical significance of the measurements of serum matrix metalloproteinase-9 and its inhibitor (tissue inhibitor of metalloproteinase-1) in patients with pancreatic cancer: metalloproteinase-9 as an independent prognostic factor. Pancreas 38(6):613–8

Nassehi V, Hanspal NS, Waghode AN, Ruziwa WR, Wakeman RJ (2005) Finite-element modelling of combined free/porous flow regimes: simulation of flow through pleated cartridge filters. Chem Eng Sci 60(4):995–1006

Nicolson GL (1984) Cell surface molecules and tumor metastasis. regulation of metastatic diversity. Exp Cell Res 150:3–22

Otrock ZK, Mahfouz RAR, Makarem JA, Shamseddine AI (2007) Understanding the biology of angiogenesis: Review of the most important molecular mechanisms. Blood Cells, Molecules, and Diseases 39(2):212–220

Page TC, Light WR, Hellums JD (1998) Prediction of microcirculatory oxygen transport by erythrocyte/hemoglobin solution mixtures. Microvasc Res 56(2):113–126

Palaparthy R, Saini BK, Gulati A (2001) Modulation of diaspirin crosslinked hemoglobin induced systemic and regional hemodynamic response by ethanolin normal rats. Life Sci 68(12):1383–1394

Pankov K, Rsel D, Novotn M, Brbek J (2010) The molecular mechanisms of transition between mesenchymal and amoeboid invasiveness in tumor cells. Cell Mol Life Sci 67:63–71

Papadopoulos S, Endeward V, Revesz-Walker B, Jrgens KD, Gros G (2001) Radial and longitudinal diffusion of myoglobin in single living heart and skeletal muscle cells. Proc Natl Acad Sci 98(10):5904–5909

Patel S, Sumitra G, Koner BC, Saxena A (2011) Role of serum matrix metalloproteinase-2 and -9 to predict breast cancer progression. Clin Biochem 44(10-11):869–72

Perfahl H, Byrne HM, Chen T, Estrella V, Alarcn T, Lapin A, Gatenby RA, Gillies RJ, Lloyd MC, Maini PK, Reuss M, Owen MR (2011) Multiscale modelling of vascular tumour growth in 3d: The roles of domain size and boundary conditions. PloS One 6:e14,790.

Perumpanani AJ, Simmons DL, Gering A, Miller KM, Ward G, Norbury J, Schneemann M, Sherratt J (1998) Extracellular matrix mediated chemotaxis can impede cell migration. Proc R Soc Lond 265:2347–2352

Piiper J, Scheid P (1991) Diffusion limitation of O_2 supply to tissue in homogeneous and heterogeneous models. Respir Physiol 85(1):127–136

Pittman RN (2011a) Oxygen gradients in the microcirculation. Acta Physiol 202(3):311–322

Pittman RN (2011b) Oxygen gradients in the microcirculation. Acta Physiol 202:311–322

Pittman RN (2011c) Regulation of tissue oxygenation. In: Rafael S (ed) Integrated systems physiology: from molecule to function to disease, 1st edn, Morgan & Claypool Life Sciences, pp 1–100

Pittman RN (2013) Oxygen transport in the microcirculation and its regulation. Microcirculation 20(2):117–37

Popel AS (1989) Theory of oxygen transport to tissue. Crit Rev Biomed Eng 17(3):257–321

Popel AS, Gross JF (1979) Analysis of oxygen diffusion from arteriolar networks. Am J Physiol 237(6):681–689

Popel AS, Goldman D, Vadapalli A (2003) Modeling of oxygen diffusion from the blood vessels to intracellular organelles. Adv Exp Med Biol 530:485–495

Pozrikidis C (2010) Numerical simulation of blood and interstitial flow through a solid tumor. J Math Biol 60(1):75–94

Pozrikidis C, Farrow DA (2003) A model of fluid flow in solid tumors. Ann Biomed Eng 31(2):181–194

Preziosi L, Vitale G (2011) A multiphase model of tumour and tissue growth including cell adhesion and plastic re-organisation. Mathematical Models and Methods in Applied Sciences 9:1901–1932

Quail DF, Joyce JA (2013) Microenvironmental regulation of tumor progression and metastasis. Nat Med 19(11):1423–37

R R, G L, KR L, Wiederschain D, Kilroy SM, Lamb CC, Zurakowski D, Moses MA (2008) Tumor-specific urinary matrix metalloproteinase fingerprinting: Identification of high molecular weight urinary matrix metalloproteinase species. Clin Cancer Res 14:6610–6617

Rajagopalan H, Nowak MA, Vogelstein B, Lengauer C (2003) The significance of unstable chromosomes in colorectal cancer. Nature Reviews Cancer 3:695–701

Rao JS, Yamamoto M, Mohaman S, Gokaslan ZL, Fuller GN, Rao WGSSVH, Liotta LA, Nicolson GL, Sawaya RE (1996) Expression and localization of 92 kda type iv collagenase/gelatinase b (mmp-9) in human gliomas. Clin Exp Metastasis 14(1):12–8

Ribatti D (2009) Endogenous inhibitors of angiogenesis: a historical review. Leuk Res 33(5):638–44

Riddick AC, Shukla CJ, Bass CJPR, Nuttall RK, Hogan A, Sethia KK, Ellis V, Collins AT, Maitland NJ, Ball RY, Edwards DR (2005) Identification of degradome components associated with prostate cancer progression by expression analysis of human prostatic tissues. Br J Cancer 92(12):2171–80

Rocca GL, Pucci-Minafra I, Marrazzo A (2004) Zymographic detection and clinical correlations of mmp-2 and mmp-9 in breast cancer sera. Br J Cancer 90:14141421

Roose T, Netti PA, Munn LL, Boucher Y, Jain RK (2003) Solid stress generated by spheroid growth estimated using a linear poroelasticity model small star, filled. Microvasc Res 66:204–12

Roose T, Chapman SJ, Maini PK (2007) Mathematical models of avascular tumor growth. SIAM Rev 49:179208

Rosen AL, Gould SA, Sehgal LR, Sehgal HL, Levine HD, DeWoskin RD, Moss GS (1990) Effect of hemoglobin solution on compensation to anemia in the erythrocyte-free primate. J Appl Physiol 68(3):938–943

Roy R, Louis G, Loughlin KR, Wiederschain D, Kilroy SM, Lamb CC, Zurakowski D, Moses MA (2008) Tumor-specific urinary matrix metalloproteinase fingerprinting: identification of high molecular weight urinary matrix metalloproteinase species. Clin Cancer Res 14(20):6610–7

Roy R, Yang J, Moses MA (2009) Matrix metalloproteinases as novel biomarkers and potential therapeutic targets in human cancer. J Clin Oncol 27(31):5287–97

Ruoslahti E, Bhatia SN, Sailor8 MJ (2010) Targeting of drugs and nanoparticles to tumors. J Cell Biol 188(6):759–768

Salathe EP (2003) Mathematical analysis of oxygen concentration in a two dimensional array of capillaries. J Math Biol 46(4):287–308

Sauter W, Rosenberger A, Beckmann L, Kropp S, Mittelstrass K, Timofeeva M, Wlke G, Steinwachs A, Scheiner D, Meese E, Sybrecht G, Kronenberg F, Dienemann H, LUCY-Consortium, Chang-Claude J, Illig T, Wichmann HE, Bickebller H, Risch A (2008) Matrix metalloproteinase 1 (mmp1) is associated with early-onset lung cancer. Cancer Epidemiol Biomarkers Prev 17(5):1127–35

Schuff MM, Gore JP, Nauman EA (2013a) A mixture theory model of fluid and solute transport in the microvasculature of normal and malignant tissues. i., theory. J math Biol 66(6):1179–1207

Schuff MM, Gore JP, Nauman EA (2013b) A mixture theory model of fluid and solute transport in the microvasculature of normal and malignant tissues. ii: Factor sensitivity analysis, calibration, and validation. J math Biol 67

Schumacker PT, Samsel RW (1989) Analysis of oxygen delivery and uptake relationships in the rough tissue model. J Appl Physiol 67(3):1234–1244

Scium G, Shelton S, Gray WG, Miller CT, Hussain F, Ferrari M, Decuzzi P, Schrefler BA (2012) Tumor growth modeling from the perspective of multiphase porous media mechanics. Molecular and Cellular Biomechanics 9:193–212

Scium G, Shelton S, Gray WG, Miller CT, Hussain F, Ferrari M, Decuzzi P, Schrefler BA (2013) A multiphase model for three-dimensional tumor growth. New J Phys 15:015,005

Secomb TW, Hsu R, Park EY, Dewhirst MW (2004) Green's function methods for analysis of oxygen delivery to tissue by microvascular networks. Ann Biomed Eng 32(11):1519–1529

Sehgal LR, Gould SA, Rosen AL, Sehgal HL, Moss GS (1984) Polymerized pyridoxylated hemoglobin: a red cell substitute with normal oxygen capacity. Surgery 95(4):433–438

Sharan M, Popel AS, Hudak ML, Koehler RC, Traystman RJ, Jones MDJ (1998) An analysis of hypoxia in sheep brain using a mathematical model. Ann Biomed Eng 26(1):48–59

Sharma GC, Jain M (2004) A computational solution of mathematical model for oxygen transport in peripheral nerve. Comp Biol Med 34(7):633–645

Shpitzer T, Hamzany Y, Bahar G, Feinmesser R, Savulescu D, Borovoi I, Gavish M, Nagler RM (2009) Salivary analysis of oral cancer biomarkers. Br J Cancer 101(7):1194–8

Sieber OM, Heinimann K, Tomlinson IPM (2003) Genomic instability the engine of tumorigenesis? Nature Reviews Cancer 3:701–708

Skalak R (1971) Mechanics of the microcirculation. In: Fung YC, Perrone N, Anliker M (eds) Biomechanics: Its Foundations and Objectives, 1st edn, Prentice-Hall, New Jersey, pp 457–499

Smaje L, Zweifach BW, Intaglietta M (1970) Micropressures and capillary filtration coefficients in single vessels of the cremaster muscle of the rat. Microvascular Research 2(1):96–110

Spalding MC, Sebesta SC (2008) Geriatric screening and preventive care. Am Fam Physician 78(2):206–15

Stevenson WGS, Aznavoorian S, Liotta LA (1993) Tumor cell interactions with the extracellular matrix during invasion and metastasis. Annu Rev Cell Biol 9:541–573

Thorgeirsson UP, Lindsay CK, Cottam DW, Gomez DE (1994) Tumor invasion, proteolysis, and angiogenesis. J Neurooncol 18:89–103

Tian M, Cui YZ, Song GH (2008) Proteomic analysis identifies mmp-9, dj-1 and a1bg as overexpressed proteins in pancreatic juice from pancreatic ductal adenocarcinoma patients. BMC Cancer 214:1–11

Titcombe MS, Ward MJ (2000) An asymptotic study of oxygen transport from multiple capillaries to skeletal muscle tissue. J Appl Math 60(5):1767–1788

Toma A, Mang A, Schuetz TA, Becker S, Buzug TM (2012) A novel method for simulating the extracellular matrix in models of tumour growth. Computational and Mathematical Methods in Medicine 2012:109,019

Tsai AG, Friesenecker B, Mazzoni MC, HKerger, Buerk DG, Johnson PC, Intaglietta M (1998) Microvascular and tissue oxygen gradients in the rat mesentery. Proc Natl Acad Sci 95(12):6590–6595

Tsai AG, Johnson PC, Intaglietta M (2003) Oxygen gradients in the microcirculation. Physiological Reviews 83:933–963

Udagawa T, Fernandez A, Achilles EG, Folkman J, RJ DA (2002) Persistence of microscopic human cancers in mice: alterations in the angiogenic balance accompanies loss of tumor dormancy. FASEB J 16(11):1361–70

Vadapalli A, Goldman D, Popel AS (2002) Calculations of oxygen transport by red blood cells and hemoglobin solutions in capillaries. Artif Cells Blood Substit Immobil Biotechnol 30(3):157–88

Villar MV, Lloret A (2001) Variation of the intrinsic permeability of expansive clays upon saturation. In: Adachi K, Fukue M (eds) Clay science for engineering, Rotterdam: Balkema, pp 259–266

Villar MV, Snchez M, Gens A (2008) Behaviour of a bentonite barrier in the laboratory: Experimental results up to 8 years and numerical simulation. Physics and Chemistry of the Earth 33:S476–S485

Vu TH, Werb Z (2002) Matrix metalloproteinases: effectors of development and normal physiology. Genes Dev 14:2123–2133

Wang P, Olbricht WL (2010) Retro-convection enhanced drug delivery: A computational study. Ann Biomed Eng 38(8):2512–2519

Wang SD, Chen BC, Kao ST, Liu CJ, Yeh CC (2014) Genistein inhibits tumor invasion by suppressing multiple signal transduction pathways in human hepatocellular carcinoma cells. BMC Complement Altern Med 14(1):26

Wang W, Wyckoff JB, Frohlich VC, Oleynikov Y, Httelmaier S, Zavadil J, Cermak L, Bottinger EP, Singer RH, White JG, Segall JE, Condeelis JS (2002) Single cell behavior in metastatic primary mammary tumors correlated with gene expression patterns revealed by molecular profiling. Cancer Res 62:6278–6288

Weis SM, Cheresh DA (2011) Tumor angiogenesis: molecular pathways and therapeutic targets. Nat Med 17(11):1359–1370

Welter M, Rieger H (2010) Physical determinants of vascular network remodeling during tumor growth. Eur Phys J E 33:149–163

Welter M, Bartha K, Rieger H (2009) Vascular remodelling of an arterio-venous blood vessel network during solid tumour growth. J Theor Biol 259:405–422

Wood M, Fudge K, Mohler JL, Frost AR, Garcia F, Wang M, Stearns ME (1997) In situ hybridization studies of metalloproteinases 2 and 9 and timp-1 and timp-2 expression in human prostate cancer. Clin Exp Metastasis 15(3):246–58

Wu ZS, Wu Q, Yang JH, Wang HQ, Ding XD, Yang F, Xu XC (2008) Prognostic significance of mmp-9 and timp-1 serum and tissue expression in breast cancer. Int J Cancer 122(9):2050–6

Yang D, Zhao Y (2006) The constitute law of gas seepage in rock fractures undergoing three-dimensional stress. Transport In Porous Media 63(3):463–472

Yao H, Gu WY (2007) Convection and diffusion in charged hydrated soft tissue: a mixture theory approach. Biomech Model Mechanobiol 6(1-2):63–72

Yu P, Mustata M, Peng L, Turek JJ, Melloch MR, French PMW, Nolte DD (2004) Holographic optical coherence imaging of rat osteogenic sarcoma tumor spheroids. Applied Optics 43(25):4862–4873

Yu Q, Stamenkovic I (2000) Cell surface-localized matrix metalloproteinase-9 proteolytically activates tgf- and promotes tumor invasion and angiogenesis. Genes Dev 14:163–176

Yulianti K, Gunawan AY (2012) An asymptotic study for the steady model of oxygen diffusion in tissue region. ITB JSci 44(2):164–178

Zhang L, Kim D (2012) Computational analysis of the effects of matrix-degrading enzymes on cancer-cell invasion. Journal of Applied Physics 112:124,704

Zhao Y, Jin Z, Sun J (1994) Mathematical model for coupled solid deformation and methane flow in coal seam. Appl math Modelling 18(6):328–333

Zhao Y, Hu Y, Zhao B (2004) Nonlinear coupled mathematical model for solid deformation and gas seepage in fractured media. Transport In Porous Media 55(2):119–136

Zhao Y, Qu F, Zhijun W (2010) Experimental investigation on correlation between permeability variation and pore structure during coal pyrolysis. Transport in porous Media 82(2):401–412

Zhu Q, Zhang A, Liu P, XXu L (2012) Study of tumor growth under hyperthermia condition. Comp Math Method in Medicin 2012, DOI 10.1155/2012/198145

Zipfel WR, Williams RM, Christie R, Nikitin AY, Hyman BT, Webb WW (2003) Live tissue intrinsic emission microscopy using multiphoton-excited native fluorescence and second harmonic generation. Proc Natl Acad Sci 100(12):7075–7080

Ziyad S, Iruela-Arispe ML (2011) Molecular mechanisms of tumor angiogenesis. Genes and Cancer 2(12):1085–1096

Zweifach BW (1974) Quantitative studies of microcirculatory structure and function: Ii. direct measurement of capillary pressure in splanchnic mesenteric vessels. Circulation Res 34(6):858–866

Appendix

Verification of numerical simulation

All of the computations of the coupled mathematical models in this current study are programmed in-house code designed by Fortran 90 in single-precision floating-point format. The in-house codes are modified basing on a complete system of programming for solid deformation–fluid seepage–convection and diffusion in porous media(Liang and Zhao 2005;Zhao et al 1994), their programming had been used in the study of rock salt and many numerical results from their studies been widely accepted in the field of the transport in porous media. (Liang and Zhao 2005;Zhao et al 1994);Zhao et al 2004;Zhao et al 2010;Yang and Zhao 2006).

In Liang'study (Liang and Zhao 2005), the hydraulic fracture in rock salt is a complicated solid fluid and mass transfer coupling process. Through finite element methods , the law of fracture aperture changing and water pressure distribution in the crack is obtained under the coupling action of fracture and dissolution. The simulated results are shown in Fig.4.1. Furthermore, their study also compared the tested results from salt deposit in Yuncheng , China, as presented in Fig.4.2, the curve of simulated and tested hydraulic pressure found that the simulated results and tested results are basically in conformity with each other, demonstrating that the established solid fluid and mass transfer coupling mathematical model of hydraulic fracturing in rock salt is reasonable. Therefore, it should be reliable to use this system of simulation methods for solid-fluid

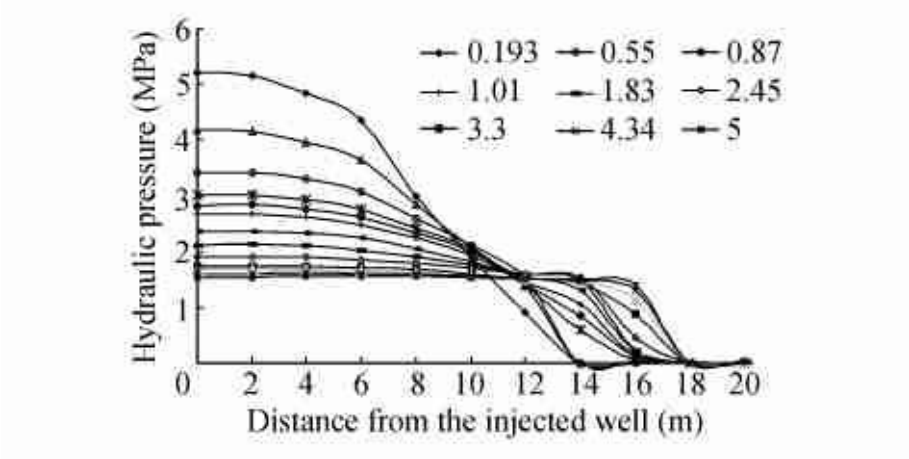

Figure 4.1: The change of hydraulic pressure with time(Liang and Zhao 2005).

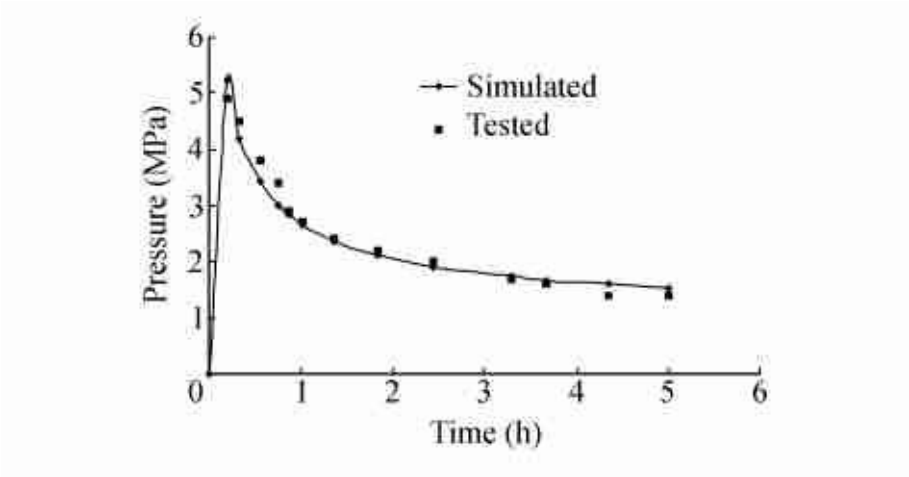

Figure 4.2: Curve of simulated and tested hydraulic pressure with time in rock salt during hydraulic fracture (Liang and Zhao 2005).

coupling convection-diffusion in porous media here, which has produced many results in the relevant studies.

Publication

- Ning Zhao, Keiji Iramina.
  A mathematical coupled model of oxygen transport in the microcirculation: the effect of convection-diffusion on oxygen transport.
  Journal of mechanics in medicine and biology
  Vo1.15.No.1(2015)1550003(26 pages)
  DOI:10.1142/S0219519415500037